NONEQUILIBRIUM PROPERTIES OF SUPERCONDUCTING-NORMAL METAL BOUNDARIES

Thesis by

David William Palmer

In Partial Fulfillment of the Requirements

for the Degree of

Doctor of Philosophy

California Institute of Technology

Pasadena, California

1975

(Submitted March 4, 1975)

ACKNOWLEDGMENTS

This investigation would never have been accomplished were it not for the theoretical and professional instruction of my thesis adviser, Professor J. E. Mercereau, and for the technical and experimental guidance of Dr. H. A. Notarys. The open, spirited method of research they practice and encourage in the Bosonic Laboratory has led to a many faceted investigation of nonequilibrium macroscopic quantum mechanics that excites the curiosity and encourages the necessary hard work.

In addition, this educational undertaking would not have been financially possible were it not for the three year National Science Foundation fellowship and the supplemental Robert S. McNamara fellowship and work program.

Permission from the American Physical Society for the use of Figs. A.1, A.2, and A.3, and the Institute of Electrical and Electronic Engineers for Figs. 3.2, 3.3, 3.6, and 3.7, is gratefully acknowledged.

ABSTRACT

Three different nonequilibrium states of superconductivity were experimentally investigated. These experiments included studies of: the electron transport properties across the interface of a single superconductor and a normal metal, electron transport between two weakly coupled superconductors, and electron transport through periodic arrays of hundreds of weakly coupled superconductors. In all of these investigations most emphasis was given to quantum interference effects. All three nonequilibrium states produced time dependent voltages which were investigated both by inducing step structure on the I-V characteristics with external microwave radiation, and by directly measuring the internal oscillating potentials. Josephson's relationship between frequency and voltage, $h\nu = 2eV$, was found to be significantly modified in certain well defined circumstances leading to a better understanding of quantum rules for nonequilibrium weak superconductivity.

To produce the structures necessary for these studies, thin films of soft, hard, and compound superconductors were used. These thin films were defined into strongly superconducting, weakly superconducting, and normal regions using highly refined photolithographic and etching techniques to provide boundary definition of less than 250Å, depth determination to within 5Å, and lateral detail resolution of 2000Å.

All results can be described using concepts of macroscopic quantum mechanics and simple equivalent circuit representations for the nonequilibrium electron state. Macroscopic wave function boundary

conditions and coupling effects were examined with particular emphasis on characteristic coupling energy, decay lengths, healing time, and thermal constants. The geometric dimensions and equilibrium electronic properties were used to predict the critical current-temperature dependence and the rf responsivity. In some circumstances a single superconductor-normal metal interface was found to show quantum interference effects much as though the superconductor were interfering with itself. Thermal effects, which can dominate at high voltages, were calculated, measured, and designed around so that the time response of the macroscopic quantum state could be investigated down to 10^{-12}sec.

TABLE OF CONTENTS

INTRODUCTION

The history of the macroscopic quantum wave function concept started in 1950 when Fritz London explained the Meisner effect and the persistent currents in superconducting rings by treating the super-electron state as a single macroscopic quantum wave function. At first the advantage of this perspective over a microscopic view was not completely appreciated, since the quest of most physicists in the 50's was to microscopically understand the electron interactions that produced superconductivity. However, the extraordinary advantage of the macroscopic phase state concept developed in the years following Brian Josephson's (1962) prediction of interference effects between two weakly coupled superconducting wave functions.[1] Phase and phase interference became more meaningful through the superconducting oxide-barrier junction experiments and discussions of P. W. Anderson[2] (1963-66) and the "double slit" DC interferometer experiments of J. E. Mercereau (1964).[3]

Weak superconductivity, superflow in the presence of a potential gradient, was first described by T. J. Rieger, D. J. Scalapino, and Mercereau (1971) as a "phase slip" process in a macroscopic wave function.[4] The macroscopic wave function perspective equates a superconducting current with a phase gradient in the wave function, $j \sim \nabla\theta$; therefore, a voltage which freely accelerates the super-electrons increases the current and hence the phase gradient in the wave function. This acceleration must be bounded, and in some geometries the limitation is not followed by a sudden switch to normal electron

conduction but rather a phase gradient relaxation process is initiated called "phase slip". This phase slip process is essentially a transition from one macroscopic quantum state to another with 2π less total phase change across the voltage supporting region. The phase slippage of 2π is accomplished by a periodic local diminution in superelectron density followed by recovery of the superelectron density supporting 2π less phase difference. Thus the finite voltage state of superconductivity is described as a periodic time dependent change in both the pair density and the phase gradient of the wave function with a period equal to $h/2eV$.

A more recent approach to reconcile weak superconductivity at finite voltage is to treat a local voltage sustaining region as represented by <u>two</u> coincident macroscopic quantum states whose amplitudes and phases are both functions of position (M. L. Yu 1973).[5] This description leads to many of the same consequences as those of phase slip, but has the analytic advantage of not relying on discontinuous acceleration processes to create the time dependence of pair density.

Weak superconductivity is a non-local nonequilibrium process and therefore has been extremely difficult, if not impossible so far, to describe from first principles. However, the experimental direct relationship between the period of time dependent variables and the applied voltage, and the discovery that in many different geometries the same nonequilibrium characteristic lengths occur, are two important keys to the fundamental understanding of a very complex process. As an extension of the macroscopic quantum wave function approach to nonequilibrium processes this thesis will consider time dependent phenomena

at the superconducting-normal metal interface, and at arrays of such interfaces. All phenomena found are described using macroscopic wave functions and transitions between macroscopic quantum states.

The results of this investigation are described according to the accepted views of superconductivity and superconducting weakly coupled wave functions. Clarification is made during each topic of discussion as to what is established knowledge and what is newly discovered; nonetheless it is helpful for seeing the connective thread of research to have listed in one place all new results of this investigation. Those results are (1) The weak coupling of two superconducting macroscopic wave functions through a normal metal was experimentally studied as a function of temperature, normal metal length, and mean free path. Agreement with proximity effect pair density distribution at a superconducting-normal interface was found. (2) Microwave perturbations on the I-V characteristics of such weakly coupled wave functions were compared to analytically known results of Josephson tunnel junctions. Good agreement was found in rf power and temperature dependences, but the frequency dependence was measured as $1/\nu^3$ instead of the predicted $1/\nu^2$, which is suggestive of possible relaxation processes in the voltage frequency relation. (3) The thermal limitations on interference effects were discovered and designed around so that 300 GHz interference response was achieved with a bridge. The response time implied was used to eliminate many relaxation processes from phase slip recovery. (4) A new method of measuring the fraction of power absorbed from incident microwaves was developed to allow the first quantitative measurements

of variable frequency for low resistance coupling. (5) Large scale series arrays of quantum interference bridges were fabricated and tested for the first time. A strong internal coupling was found between bridges when closely spaced ($< 1\mu$). This coupling produced coherent behavior between the individually time dependent voltages of the bridges. A strongly coupled array of n bridges acted as a single Josephson oscillator quantized in units of $(n)(h/2e)$. This strong coupling was described as the result of both direct bridge to bridge interaction through the superconducting separation, and also next nearest neighbor wave function interference. (6) The time dependence found in single bridges and arrays suggested that the simple superconducting-normal interface was also time dependent. Indeed such a time varying voltage was found across a current biased interface. In addition, unexpected features were discovered, including the existence of a critical current for the proximity boundary and a voltage-frequency relation $h\nu = n2eV$. Most often $n = 2$ and the boundary was described by a bisected version of the phase slip process. (7) In order to do this research unique submicron fabrication techniques were developed both in photoresist exposure and thin film etching.

Chapter one contains a review of important features of the superconducting state and the macroscopic wave function. Chapter two considers the proximity effect bridge, concentrating on the nature of the two wave function coupling and the response of the bridge to microwave perturbations. Chapter three discusses series arrays of hundreds of bridges. Coupling requirements between bridges and next nearest wave functions are described. Chapter four examines the single

superconducting-normal interface, presenting critical currents, a time dependent voltage, and a variation on the Josephson voltage-frequency relation. Appendix A considers all aspects of thin film deposition, photoresist, and thin film etching techniques that were developed and used for this investigation. Appendix B describes the experimental measurement methods used. Appendix C discusses the thermal effects seen in proximity bridges.

CHAPTER 1

ESTABLISHED PROPERTIES OF SUPERCONDUCTING MACROSCOPIC QUANTUM WAVE FUNCTIONS

Review of the well known properties of superconducting macroscopic wave functions is necessary before discussing the time dependent effects which were discovered during this investigation of superconducting-normal metal boundaries. The emphasis of this introductory framework will be to review the applicability of the macroscopic wave function to superconductivity and to estimate how far from equilibrium the superconducting state can be pushed before the imposed scales of distance, time, or pair density disqualify the macroscopic wave function assumption.

1.1 The Macroscopic Assumption

Many condensed matter phase transitions have been looked at as Bose condensations: superfluid, superconducting, lattice distortive, exitonic, magnetic, and liquid-solid transitions.[1] The Bose particles involved include the He^4 atoms themselves in liquid He, pairs of opposite spin and momenta electrons in a superconductor, and lattice phonons in a lattice distortive transition. These transitions can be classified into two categories. The first type of transition gives long range spatial order, and the other type leads to long range momentum order. Within this dichotomy helium superfluidity and metallic electron superconductivity can be considered as a Bose condensation with long range momentum order. This order results in fluid flow

without dissipation.

Superfluid condensed states can be considered a macroscopic quantum mechanical wave function of the form[2]

$$\psi(r) = \sqrt{\rho(r)}\, e^{i\theta(r)} \tag{1-1}$$

Operationally $\psi\psi^* = \rho$ is the density of superconducting pairs, and θ is the phase of the wave function. This representation of the superconducting electron condensate as a single wave function is an assumption originated by F. London in 1935, but is an assumption that is warranted both by experimentally confirmed predictions and some theoretical justification based on the microscopic theory of superconductivity.[3] The assumption of the wave function representation ψ also allows all quantum mechanics operator manipulations upon ψ. For example, applying the standard velocity operator $v = -(1/m^*)(ih\nabla + e^*A)$ to the wave function gives the velocity density which, when multiplied by the charge of the superconducting carriers, e^*, gives the electric current

$$j = \rho \frac{e^*}{m^*} (\hbar\nabla\theta - e^*A) \tag{1-2}$$

Thus the supercurrent is proportional to the gradient of the macroscopic phase. Frequently in this research the one dimensional, zero magnetic field nature of the current flow will allow the vector potential term to be ignored.

If a voltage is applied to the superconductor, the superelectrons will accelerate, resulting in a current increasing in time. A time change in current implies a time change in the gradient $\nabla\theta$. Thus, a

voltage drop between two points of a superconductor produces a time rate of change in the phase difference between the two points. The exact relation is

$$\frac{d}{dt}(\theta_1-\theta_2) = (2e/\hbar)V \qquad \text{(I-3)}$$

Experimentally it was found that a superconductor is a perfect diamagnetic material at low magnetic field levels (the Meisner effect).[4] Surface currents arise on the superconductor with the presence of an external field in order to prevent field penetration into the superconductor. A useful length, the London penetration depth, indicating the distribution of shielding currents can be extracted from equation (1-2). Taking the curl of both sides leaves[5]

$$\lambda^2(\nabla \times j) = H \qquad \text{where} \quad \lambda^2 = m^*/\rho e^{*2}\mu_o$$

Since $\nabla \times H = j$, the above equation leads to a second order differential equation in j. Thus the shielding currents drop exponentially in magnitude beneath the surface of a superconductor, or equivalently the external magnetic field penetrates the surface on the scale of λ. Putting in values for m, e, ρ for conduction electrons in a typical metal gives $\lambda = 100\text{Å}$. Experimentally the measured value for most superconductors is $\lambda \sim 500\text{Å}$. This discrepancy is due to nonlocal nature of superconductivity. The superconducting thin films used in this investigation span the thickness range from below to well above λ in thickness. Since λ is a function of pair density, ρ, it is a function of temperature. Experimentally it is found that[6]

$$\lambda(T/T_c) = \lambda(0)[1 - (T/T_c)^4]^{-1/2} \qquad (1\text{-}4)$$

where T_c is the superconducting transition temperature and $\lambda(0)$ is the penetration depth at $T = 0$.

Superconductivity is a nonlocal property. That is, the strength of superconductivity, the density of superelectron pairs, does not depend solely on the nature of the lattice and electrons at a point, but rather represents an average over a sphere of radius ξ, the coherence length. Typically $\xi = 1\mu$ in a superconductor well below T_c. This nonlocality can be justified by the following uncertainty argument. The superconducting electrons have lowered their energy by forming pair states.[7] The lowered energy at $T = 0$ represents about kT_c per pair. The uncertainty time necessary to determine this energy difference in an interaction is therefore $\sim h/kT_c$, so the distance of an interaction for electrons at the Fermi velocity is $\xi_o \sim hv_F/kT_c$.

The coherence length is about 1μ when $T_c = 4^oK$ and $v_F = 10^6$m/sec. Thus many pairs exist within a coherence volume all having the same phase to maximize the condensation energy; and a sequence of overlapping coherence volumes can be considered as a mechanism for providing long range momentum order (phase order). Again, if the mean free path, ℓ, is shorter than the coherence length, the random walk considerations are important. Thus when $\ell < \xi$ a better approximation is[8]

$$\xi(T) \simeq \sqrt{\ell\xi_o}\,\left(\frac{T_c}{T_c - T}\right)^{1/2} \qquad (1\text{-}5)$$

Notice, since the pair binding energy goes to zero at $T = T_c$ there is also temperature dependence for the coherence length.

The consequences of a well defined macroscopic phase are sometimes more unexpected than an arbitrary observable current (1-2) or voltage (1-3). For example, magnetic flux can be quantized as a direct result of macroscopic phase. The wave function in a superconducting ring must be single valued at equilibrium. Thus traversing around the ring and returning to the same point can only lead to phase changes of $2\pi n$, for integer n. Since the phase gradient represents current, this is a statement of quantized current flow or magnetic flux in a superconducting ring. Formally, integrate equation (1-2) over a path more than λ beneath the surface of the superconducting ring where the current density is zero. Here $0 = j = \frac{\hbar}{m}(\nabla\theta - \frac{q}{\hbar}A)\rho\, e^*$ thus integration gives $2\pi nh = \hbar \oint \nabla\theta \cdot ds = q \oint A \cdot ds = q\Phi$, the flux through the loop. This quantum of trapped flux is called $\Phi_o = h/2e$. This quantization has been experimentally observed.[9]

1.2 Relative Macroscopic Phase and Josephson Coupling

That relative quantum phase can be as real and observable as length or position was a difficult, slowly accepted concept. Arguments made by P. W. Anderson in 1966 demonstrated the dynamically conjugate relationship between the number of superconducting pairs, N, in a volume and their phase, θ.[10] Thus an uncertainty relation exists between N and θ as between p and x, in particular $\Delta N \Delta\theta \sim 1$. Thus an isolated superconductor would have no experimentally definable phase; since $\Delta N = 0$, the number of pairs is known in isolation.

Experimentally this seldom is a problem since any interaction with a superconducting volume, such as a traversing current, introduces uncertainty in N allowing phase to become a well defined variable.

Similarly two wave functions with phase $\theta_1(t)$ and $\theta_2(t)$ can have a well defined relative phase if some pair interchange is permitted. B. Josephson first derived the consequences of weakly interacting macroscopic wave functions leading to a pair current between two weakly connected superconductors,[11]

$$I_J = I_c \sin(\theta_1 - \theta_2) \tag{1-6}$$

where I_J is the pair current. This pair current provides the necessary uncertainty in the numbers of pairs in either superconducting volume that allows θ_1 and θ_2 to be sharply defined relative to each other. Another aspect of this result follows from the derived time dependence of the relative phase when a voltage, V , exists between the two wave functions[12]

$$\frac{d}{dt}(\theta_1 - \theta_2) = 2eV/\hbar \tag{1-3}$$

Thus an oscillating pair current results from a voltage between two weakly coupled wave functions. Josephson also showed that a magnetic field could modulate the phase difference $(\theta_1 - \theta_2)$ which leads to the periodic modulation of I_J with external magnetic field applied perpendicular to the coupling current flow.

The first geometry to demonstrate relative phase effects between two wave functions consisted of Pb and Sn films separated by 10Å of oxide, the original Josephson junction.[13] Since the original

observations of the Josephson effect many geometries have been developed that produce a weak coupling between two superconducting wave functions: Two overlapping superconducting thin films separated by 10Å of oxide, 100Å of semiconductor, 1000Å of normal metal, or 10,000Å of superconductor at T_c ; a sharpened point (radius $\sim$ 1μ) of superconductor pressed against a block of superconductor; two superconducting wires crossed and pressed together; a short high current density region in a thin film formed by locally constricting the width to 1μ ; and a locally depressed equilibrium superconducting pair density in a short region of a superconducting film.

Experimentally whenever weak coupling is established between two superconductors Josephson-like phenomena are observed. One purpose of this investigation has been to study in detail the interference resulting from one form of well defined and well controlled weak coupling to determine what defines the coupling as "weak" and not instead as "strong" (and therefore like a single bulk superconductor) or as "too weak" (and therefore like two isolated superconductors). In addition, quantum interference was found tc exist not only between <u>two</u> adjacent weakly coupled wave functions but, as a result of studies on series arrays of <u>hundreds</u> of weakly coupled wave functions, also between two wave functions separated by a third. Further, quantum interference effects were discovered and examined at the diffuse edge of a <u>single</u> wave function.

1.3 Internal Nonequilibrium Properties of Superconducting Wave Function

If a superconducting wave function is suddenly forced out of equilibrium, there is a certain response time necessary for recovery.

For example, if a localized depairing of electrons occurs there is a characteristic recombination time, τ_R . If the electrons are out of thermal equilibrium there is a thermal recovery time, τ_{TH} . There are many recovery times spanning the micro to picosecond range, thus the temperature dependence of these recovery times is very important in sorting out the various recovery processes involved. The nonequilibrium superconducting state has four time constants of immediate importance. First, the Ginsburg-Landau time constant, $\tau_{GL} = \frac{\hbar\pi}{8k|T_c-T|} \sim 10^{-12}$, is the time with which the superconducting pair condensate recovers when perturbed from its equilibrium density. If instead the quasiparticles (normal electrons) are perturbed, there are three associated relaxation times:[15] (1) an imbalance in the Fermi momentum distribution of quasiparticles relaxes with the branch mixing time constant, $\tau_Q \sim 10^{-10}$sec; (2) if the quasiparticles are out of thermal equilibrium this again relaxes in $\tau_{TH} \sim 10^{-10}$sec; and (3) excess quasiparticles combining to form pairs occurs in the recombination time $\tau_R \sim 10^{-9}$sec. These times imply characteristic lengths over which such imbalances can occur. For example, the length associated with τ_R in the short mean free path case is

$$\lambda \sim \sqrt{V_F \tau_R \ell} \tag{1-7}$$

Letting $V_F = 10^6$m/sec, $\tau_R \sim 10^{-10}$sec, $\ell = 100\text{Å}$ gives $\lambda_R \sim 1\mu$. This length is called the branch mixing length.

1.4 The Proximity Effect at the S/N Interface

Since the superconducting pair density is a nonlocal property, a sharp lattice interface between a superconductor and a normal metal does not lead to an equivalent pair density change on an angstrom scale. In comparison, a superconductor-vacuum interface has a constant pair density up to the metal surface, since the electrons can sample only the superconducting region due to the strong electrostatic forces near the surface. The redistribution of the equilibrium pair and normal electron density at a S/N interface is shown in figure 1.2b.

Historically S/N interfaces were studied using layered thin films. It is possible in such a geometry for the superconducting metal film to induce superconductivity in the juxtaposed normal film; this is called the "proximity effect". When both film thicknesses are comparable to the coherence length, then the proximity effect is basically a result of the nonlocal superconducting electrons sampling the superconducting environment of both films and thereby reaching some compromise energy gap for the composite film. One alternate way of looking at the proximity effect which is more useful in thicker films is to consider the superconducting film as inducing superconductivity in the normal film by a diffusion of superconducting electrons into the normal metal.

A graphic example of the thin film proximity effect appears in the temperature versus thickness plot for the layered refractory films used in this research (Fig. 1.1). In this example the net transition temperature is some average of the transition temperatures of the individual materials depending on the relative thicknesses of the layers.

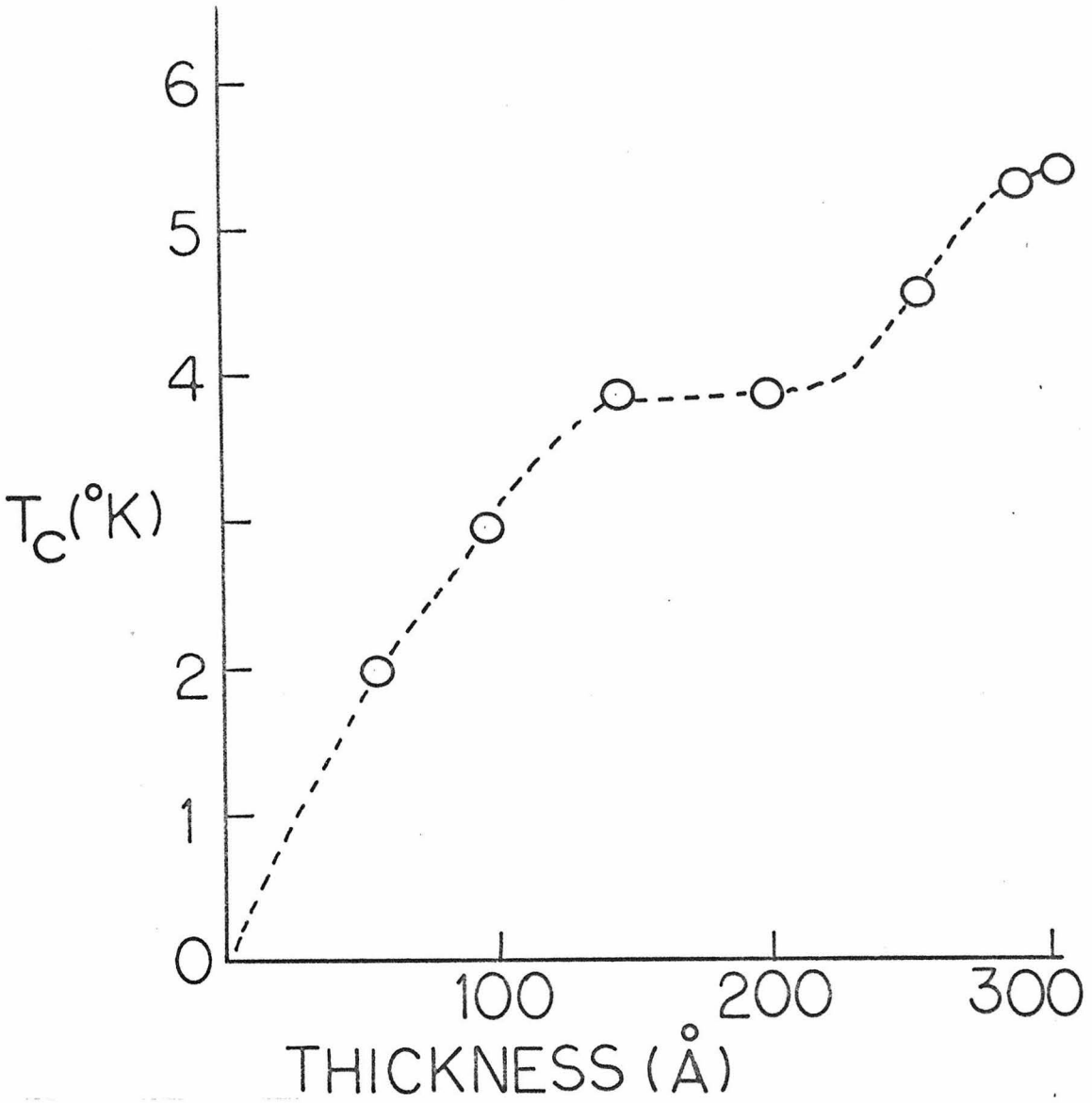

Fig. 1. A plot of the transition temperature, T_c, of a superconducting thin film used in this research as a function of thickness. This particular sample was evaporated to its full 300Å thickness from which large sections were controllably thinned down by anodization. The film consisted of 200Å of Ta with 100Å of Nb on top. The 200Å film has a $T_{c,Ta} \sim 3.9^{o}K$; the Nb, when alone on the substrate, has a $T_{c,Nb} \sim 8^{o}K$. The proximity effect, the superconducting electrons sampling both metal films, is responsible for the T_c averaging from 150-300Å. The decrease in T_c below 150Å is due to quality change in the Ta film as a function of the distance from the substrate.

The average transition temperature also depends on the mean free path of the films as reflected in the coherence length. It is also of interest to note that the T_c of a single film layer is often a function of thickness (Fig. 1.1, for thickness under 200Å). The substrate can influence the lattice structure of a very thin film in such a way as to decrease the transition temperature T_c ; however, T_c approaches the bulk value after the first few hundred angstroms are deposited.

DeGennes first derived the formulas for the density of superconducting electrons near an interface of a superconducting and normal metal.[16] If the the mean free paths are long compared to the coherence length (the clean limit) the pair density is

$$\sqrt{\rho} = \phi(x) \exp(-K|x|)$$

where ϕ is slowly varying in x , and $K^{-1} = \hbar v_N/2\pi kT$. This result can be thought of as a thermal uncertainty half life of superconducting electrons entering the normal metal, $t = \hbar/kT$, times the Fermi velocity in the normal metal, v_N .

However, the films used in this investigation typically have mean free paths shorter than the coherence length, $\ell << \xi$, so the diffusion takes place in a random walk fashion which is expressed in the above formula by forming the geometric mean with the mean free path

$$K^{-1} = \left(\frac{\hbar D}{2\pi kT}\right)^{1/2} = \left(\frac{\hbar v_N \ell}{6\pi kT}\right)^{1/2} \qquad (1\text{-}8)$$

where $D = v_N\ell/3$ is the diffusion constant.[17] Putting $v_N = 10^6$m/sec, $\ell = 100$Å and $T = 4^oK$ the value of $K^{-1} = 1000$Å .

Fig. 12

Plots of superconducting pair density, ρ_s , versus linear direction, x , for several lattice boundary conditions. (a) A superconducting metal-vacuum interface with the pair density remaining constant up to the interface. (b) A superconducting-normal metal interface. The pair density decays exponentially into the normal metal. Standard theory shows a small discontinuity of pair density at the interface, a detail which is not noticed in this investigation. (c) If a short normal region separates two superconductors, an overlap of pair density distribution will exist in the normal region. This overlap of macroscopic wave function amplitudes can lead to interference effects that are seen in the "proximity effect bridge."

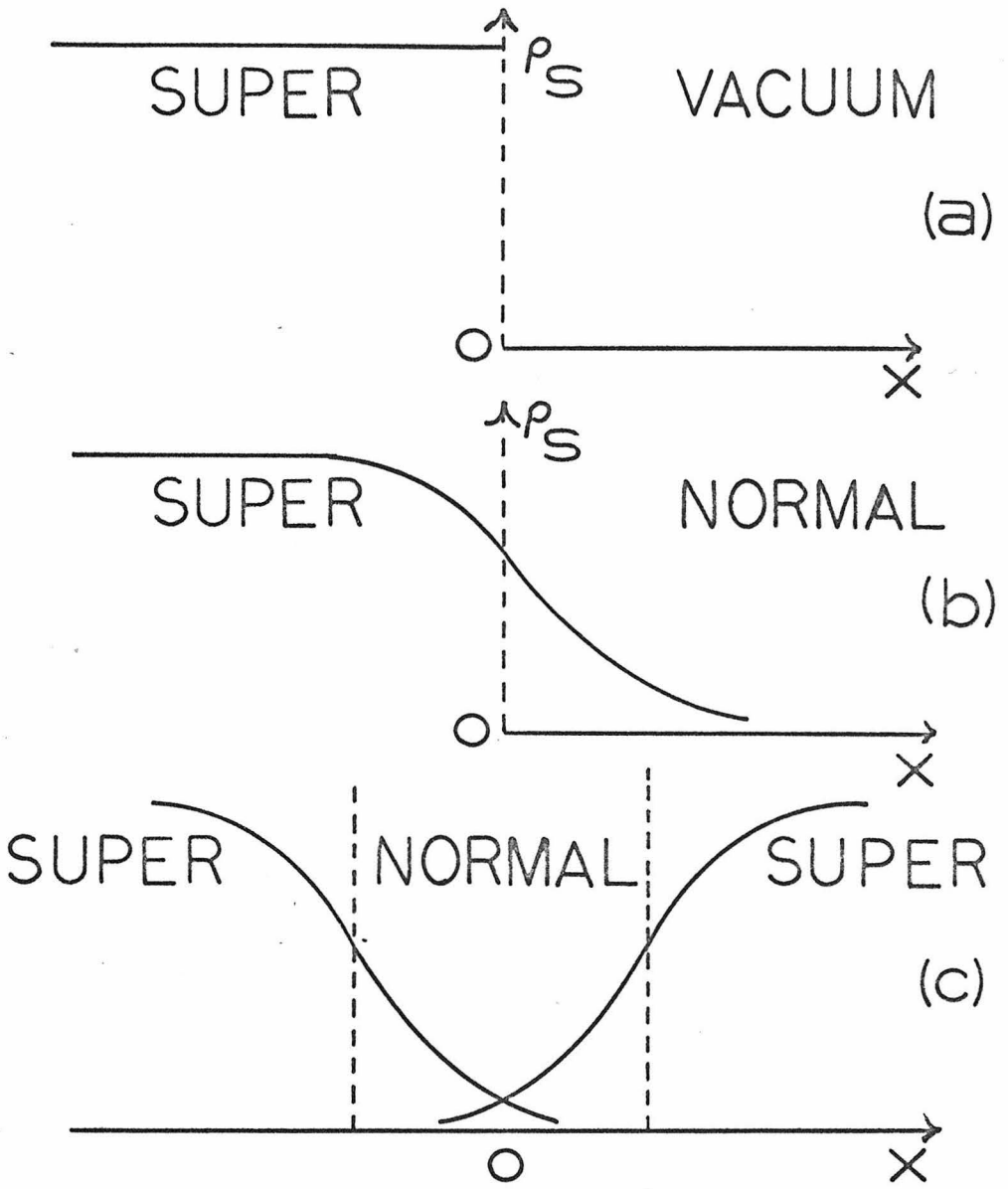
SUPER
ρ_s
VACUUM
(a)
O
X
ρ_s
SUPER
NORMAL
(b)
O
X
SUPER
NORMAL
SUPER
(c)
O
X

1.5 The Proximity Interference of Two Wave Functions

The existence of the diffuse electron S/N interface allows a very interesting coupling to exist between two wave functions. Consider a pair density distribution as shown in figure (1.2c) with the exponential tail of two wave functions diffusing across a narrow normal metal section forming a small overlap. This overlap between wave functions produces quantum interference effects. A particularly useful formalism of this interference for the investigation in this thesis has been developed recently by M. L. Yu.[18] Instead of an arbitrary small coupling, the details of the pair amplitudes are included. The wave functions can be represented as

$$\psi_0 f(x)\, e^{i\theta_1(x)} \quad , \quad \psi_0 g(x)\, e^{i\theta_2(x)} \quad , \quad f(+\infty) = g(-\infty) = 1$$

Looking at the center of the normal section where $f = g$ and the total wave function amplitude is smallest, the expression for supercurrent is

$$j_s = \frac{4\hbar|e|}{m} \psi_0^2 \left[f\nabla f \sin(\theta_1-\theta_2) + f^2\nabla\theta(1 + \cos(\theta_1-\theta_2))\right] \qquad (1\text{-}11)$$

It is of interest in passing to note that the current depends on $(\theta_1-\theta_2)$ and on the exact nature of the edge of the wave functions as defined by $f(x)$ and $g(x)$. The first term is Josephson-like (eq. 1-6) in its form with the sine of the phase difference. The second term is proportional to the gradient of phase as is the London current (eq. 1-2) as well as containing a phase interference term.

CHAPTER II

PROXIMITY EFFECT COUPLING OF TWO MACROSCOPIC WAVE FUNCTIONS

In the past several years this laboratory has concentrated its attention on quantum interference in a study of the coupling parameters between two superconducting wave functions. This has led to the development of an experimentally well defined structure now known as a "proximity effect bridge" in which a short section of normal metal separates two superconductors.[1] The symbol (S/N/S) will be used in the text to represent these structures. In the normal metal the superconducting wave functions can overlap and quantum interference can occur. Several aspects of this coupling have been investigated as a result of this thesis: (1) This chapter will consider the generality of this overlap coupling, that is, the materials, distances, and temperatures over which such quantum coupling can exist. (2) Using the maximum proximity supercurrent flow through the S/N/S bridge as a measure of the coupling strength, this strength is studied as a function of temperature, bridge geometry, and film material properties. (3) High frequency (high voltage) coherent response of the S/N/S sets a lower bound on the recovery time of the interference regions of the two macroscopic wave functions giving some insight into recovery processes. (4) The existence of high voltage across the resistive bridge produces a temperature rise in the bridge region. This temperature rise is responsible for some high frequency cutoff and critical current hysteresis which had previously been considered quantum mechanical. (5) Low power microwave perturbations are used to compare proximity coupling with the analytical solution of Josephson tunneling coupling.

2.1 Generality of the Planar Proximity Effect Bridge

For these investigations it has been necessary both to develop a controlled technique for "weakly" coupling two superconductors and to show to what extent if any the important physical results of the investigation depend on the particular materials used (as distinct from the superconducting state itself). In order to do this it has been necessary to develop special thin film proximity effect bridges and associated circuitry with characteristic dimensions less than one micron. It has been shown as a result of this work that planar proximity effect bridges can be made out of any superconducting film using any method which locally reduces the superconducting pair density, ρ_s . This experimentally proven generality bespeaks of the correctness of the generality of the model used to describe this bridge, the macroscopic wave function phase slip model. Figure 2.1a is a schematic plot of the necessary pair density distribution for weak coupling; as will be indicated later the important parameters are L and ρ_w . Figure 2.1b is a schematic illustration of a thin film proximity effect bridge in which an inhomogeneous section connects two strong superconducting regions. Basic to the technique is finding situations in which geometric changes in the films can be used to create the necessary profile for ρ_s . To eliminate suspicions as to material or lattice parameter importance in the workings of these bridges, tests were made in this investigation with soft and hard superconducting elemental thin films as well as high transition temperature compound films.

The original proximity effect bridges were made by first depositing a narrow line of Au on the substrate and then a film of Sn (Fig.

Fig. 2.1

Schematic representation of thin film proximity effect bridges.

In (a) the most general requirement to make a bridge, the reduction in pair density in a localized region, is represented.

The parameters used in the text are displayed in (b). "L" is the current length of the bridge, "W" is the current width, and "t" is the bridge thickness. The bias current direction from one strong superconductor to the other is indicated by the large arrow.

Part (c) is a side view of one way of effecting the necessary localized pair reduction. By placing a Au line on a substrate and overlaying a Sn film, a region of lower pair density separating two stronger regions is obtained. These Sn/Au bridges have worked with $100\text{Å} < t < 2500\text{Å}$, $.5\mu < L < 5\mu$, $2\mu < W < 10^3\mu$.

Layered refractory films can also be manipulated to locally modify the pair density as in (d) and (e). If the local T_c decreases with decreasing thickness as in Nb/Ta films, then a line partially etched into the film forms a bridge. However, if the film T_c increases with decreasing thickness as for W/Ta, then leaving a line of the film unetched forms a bridge. These proximity effect bridges have shown interference for $30\text{Å} < t < 500\text{Å}$, $.3\mu < L < 2\mu$.

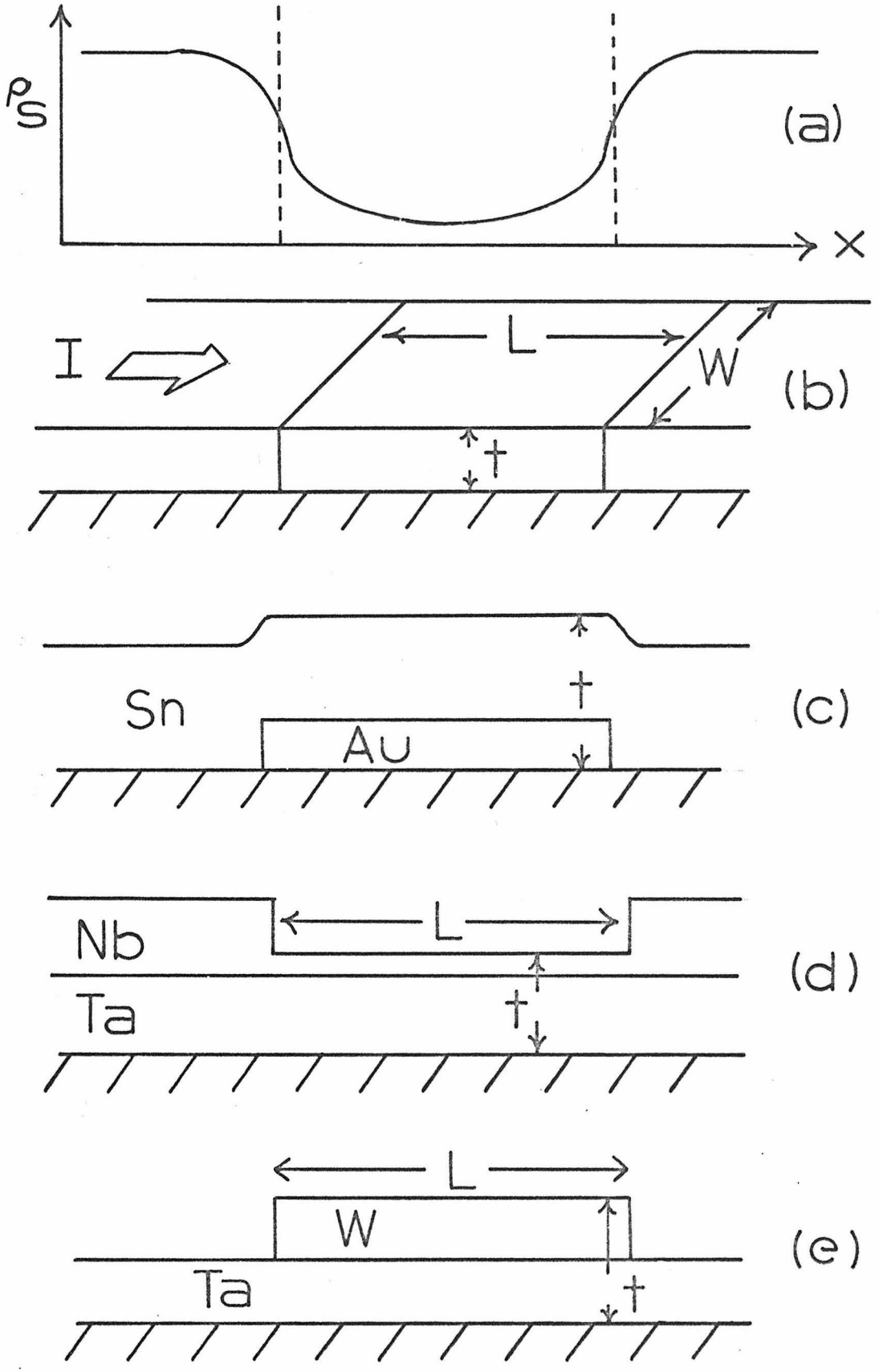
ρ_s
(a)
X
I
L
W
(b)
t
Sn
Au
t
(c)
Nb
L
Ta
t
(d)
L
W
Ta
t
(e)

2.1c). The Sn/Au line region had a reduced transition temperature and thus lower pair density at any temperature compared to the Sn film alone. Such bridges were also made with In, Pb, and Cu.

Refractory films were also used as bridge materials (Nb, Ta, W, Ti, Hf, Zr). Two basic methods were used. First, the films used tend to have a transition temperature, T_c, which depended on thickness (Appendix A). The typical film showed a strong T_c dependence on thickness below 100Å. Thus by taking a 300Å film of Ta and etching a line with a depth of 200Å a locally depressed T_c region was formed separating two strongly superconducting half planes (Fig. 2.1d). A second approach, which was more reproducible and versatile, started with a built-in gradual thickness dependence of T_c by layering refractory films of differing independent T_c. For example, a layered film of 200Å of Ta under 100Å of Nb has a transition temperature of $5.5^{\circ}K$. The Nb film alone on the substrate would be superconducting at $8^{\circ}K$ and the Ta at $4.1^{\circ}K$, but the proximity effect[2] allows the conduction electrons to average the gap energy of the two materials and produce a composite film of homogeneous superconductivity whose T_c is $5.5^{\circ}K$. Now, by removing the top Nb in a local region the T_c was reduced forming a weak link between the two bordering regions. An inverted structure of refractory films also produced this result with more T_c depressing film left on a small linear region (Fig. 2.1).

Additional insurance of material independence was given by successful bridge fabrication on high T_c compound films of NbN and Nb_3Sn.[3] The NbN samples were of thickness $\sim$3000Å and transition temperature $\sim 14.7^{\circ}K$, with an appreciable T_c versus thickness dependence

under 1000Å. It was this natural T_c versus thickness that was used to introduce the necessary inhomogeneities in pair density. Photoresist masking was used to define the regions to be thinned or cut away and argon ion beam etching was used for material removal. Bridges were made with lengths 1-2μ, widths ∿35μ, thicknesses 375-750Å, and operating temperatures up to 14°K. Bridge resistance was ∿.2Ω. Bridges were also made in Nb_3Sn by photolithographic and argon ion etch techniques. Typical dimensions for bridges were: length ∿1μ, width 5-15μ, thickness ∿400Å in a 500Å basic film, with bridge resistance of 1Ω. Transition temperature for the basic films ranged up to about 17.5°K depending on thickness, with bridge transition temperatures about 0.5°K less than that of the basic film.

The dimensional and material parameters for these bridges have been varied over a wide range: resistivity 10^{15}Ω-m for Nb/Ta to 10^{18}Ω-m for Nb_3Sn; operating temperature of the bridge 1.3-17°K; length of bridge, .2-3μ; resistance of bridge, 1mΩ - 1Ω. In addition the film thickness in the bridge region has been varied over 50-500Å in Nb/Ta and 50-2000Å for Sn/Au. Yet quantum interference effects are observed in all cases. Recently other scientists have begun to fabricate proximity effect bridges in the spirit of the above mentioned bridges. However, their techniques for weakening a small dividing section of the film often differed from the above methods, emphasizing again how general the results of the weakening are. Their techniques are: (1) Mo thin films have been elevated in T_c by implanting N^+ or S^+ everywhere but along a fine dividing line[4], (2) crystalline Nb films have been locally weakened by structural change caused by ion bombardment[5],

(3) Nb films have also been weakened by Fe ion implantation.[6]

2.2 Phase Slip Description of Weak Proximity Coupling

Many features of proximity effect bridges have been adequately explained in previous investigations.[7] In particular, an analytic expression for the bridge supercurrent in the absence of internal noise, rf radiation, and Joule heating effect has been deduced and experimentally confirmed

$$I_s(t) = \frac{I_c}{2}\left[1 + \cos\left(\frac{2e}{\hbar}\int_0^t V(t')\,dt'\right)\right] \qquad (2\text{-}1)$$

where I_c is the critical current, V the voltage across a current biased bridge (Fig. 2.2a). This interference supercurrent is seen to have a slightly different form from that derived by Josephson (eq. 1-6) for an insulating tunnel junction; this difference arises from the phase slip process to be described later. Thus the supercurrent is time dependent when a voltage exists between the two wave functions, and the frequency-voltage dependence is again the constant 2e/h . The exact wave form of the supercurrent is not experimentally known but for analysis is approximated by the (1 + cosine) term. Figure 2.2b shows a typical I-V characteristic that results from this equation and accurately represents the experimental result. The constant resistance or slope is well defined above $\sim 2I_c$ and corresponds closely to the normal state resistance of the bridge above its transition temperature, T_{cb} . The excess current, shown as ΔI in figure 2.2b, is unique to proximity effect bridges and is due to the unidirectional flow of the supercurrent in the voltage state as opposed to the symmetric flow of the ac pair current in Josephson tunnel junctions.

Fig. 2.2

Schematic plots of currents and voltages of the phase slip description which agree with the measured characteristics of the proximity effect bridge.

Part (a) is a graph of the supercurrent through a voltage sustaining bridge, I_s , as a function of time. The voltage across the bridge accelerates the superconducting electrons, increasing I_s until the critical velocity of the weakest bridge region is reached. The current, I_s , then is quenched to zero, the bridge recovers, and the acceleration process starts again. Notice the periodic current flow is unidirectional unlike the Josephson tunnel junction.

Part (b) is a typical I-V curve of a proximity effect bridge. The critical current, I_c , is the maximum bias current that will pass through the bridge without creating a voltage drop. The excess current, ΔI , is experimentally $\sim I_c/2$ and results from the unidirectional periodic supercurrent flow through a voltage sustaining bridge.

(c) Application of rf radiation to a proximity effect bridge induces "steps" in the I-V characteristic which occur at multiples of the Josephson voltage, $V_J = h\nu_{rf}/2e$. For example, one microvolt $\sim$ 500 MHz, and one millivolt $\sim$ 500 GHz.

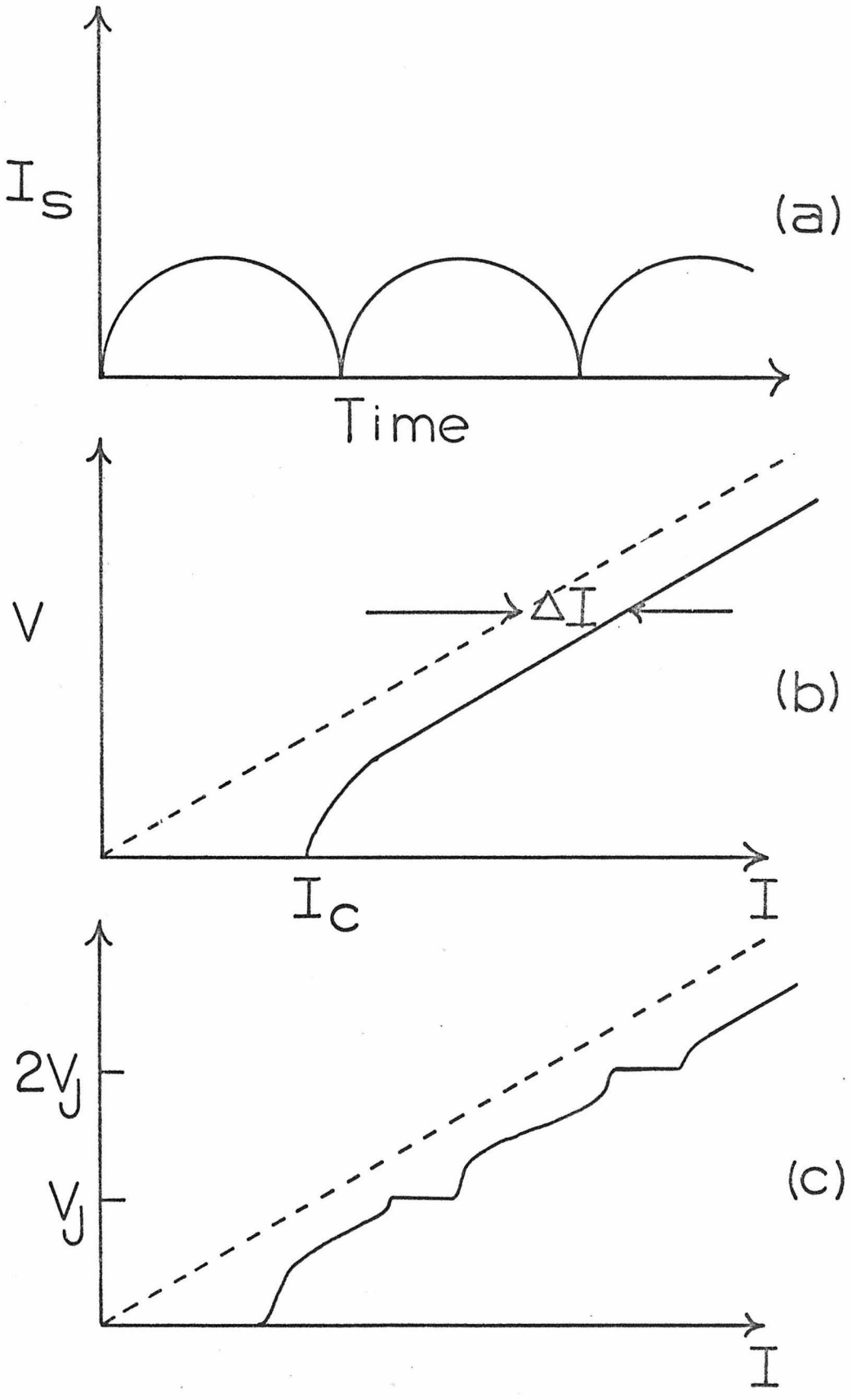
I_s
(a)
Time
V
ΔI
(b)
I_c
I
$2V_j$
V_j
(c)
I

The time variation of supercurrent, the phase slip process, is understood to be a time dependent phase change across the bridge which is periodically interrupted by the density of pairs in the center coherence length of the bridge diminishing to zero thereby allowing a 2π phase winding to be removed (Fig. 2.3).[8] The existence of a time average voltage across a bridge causes superelectrons to accelerate to their critical current, j_c, where their kinetic energy equals the energy gap. The pair density ρ_s is now unstable and decays spontaneously to a lower superconducting current state as shown in figure 2.3; the process then repeats. Therefore the phase slip process is a relaxation oscillation in the phase difference across the bridge. Previous detailed analysis[9] of a voltage sustaining superconductor using the time dependent Ginsburg -Landau theory has shown the phase slip process occurs with frequency $\nu = 2eV/h$. The interference indicated in the phase slip equation 2-1 resembles closely in form the second term of equation 1-11 which was derived by two-wave function considerations. Thus equation 1-11 can be considered part Josephson-like and part phase-slip-like depending on the details of the wave function edges. Throughout the discussion of the next few sections attention will be called to the relative importance of the two terms of equation 1-11 and hence the applicability of equation 2-1 in all limits of planar bridge quantum interference.

Application of microwave radiation in addition to a constant voltage causes a frequency modulation effect which produces "steps" in the I-V characteristic[10] at the Josephson voltages $V = nh\nu/2e$, where the bridge slip frequency coincides with the incident frequency or

Fig. 2.3

Schematic representation of the phase slip process in a proximity effect bridge. The length of the arrow (or distance from the axis) represents the amplitude of the superconducting wave function. The angle as measured from vertical represents the phase. The horizontal axis is the x-direction, the current direction in a bridge. (a) represents constant amplitude and phase throughout the bridge region. A voltage has caused a relative phase change, hence current flow, along the axis in (b). This gradient of phase represents a critical current flow which forces a decrease in the local amplitude of the wave function (c), and allows the wave function to recover to its original constant phase and amplitude condition and start all over (d). One 2π winding over this region was used for artistic convenience; the cycle could have been between 8π and 10π of total phase change.

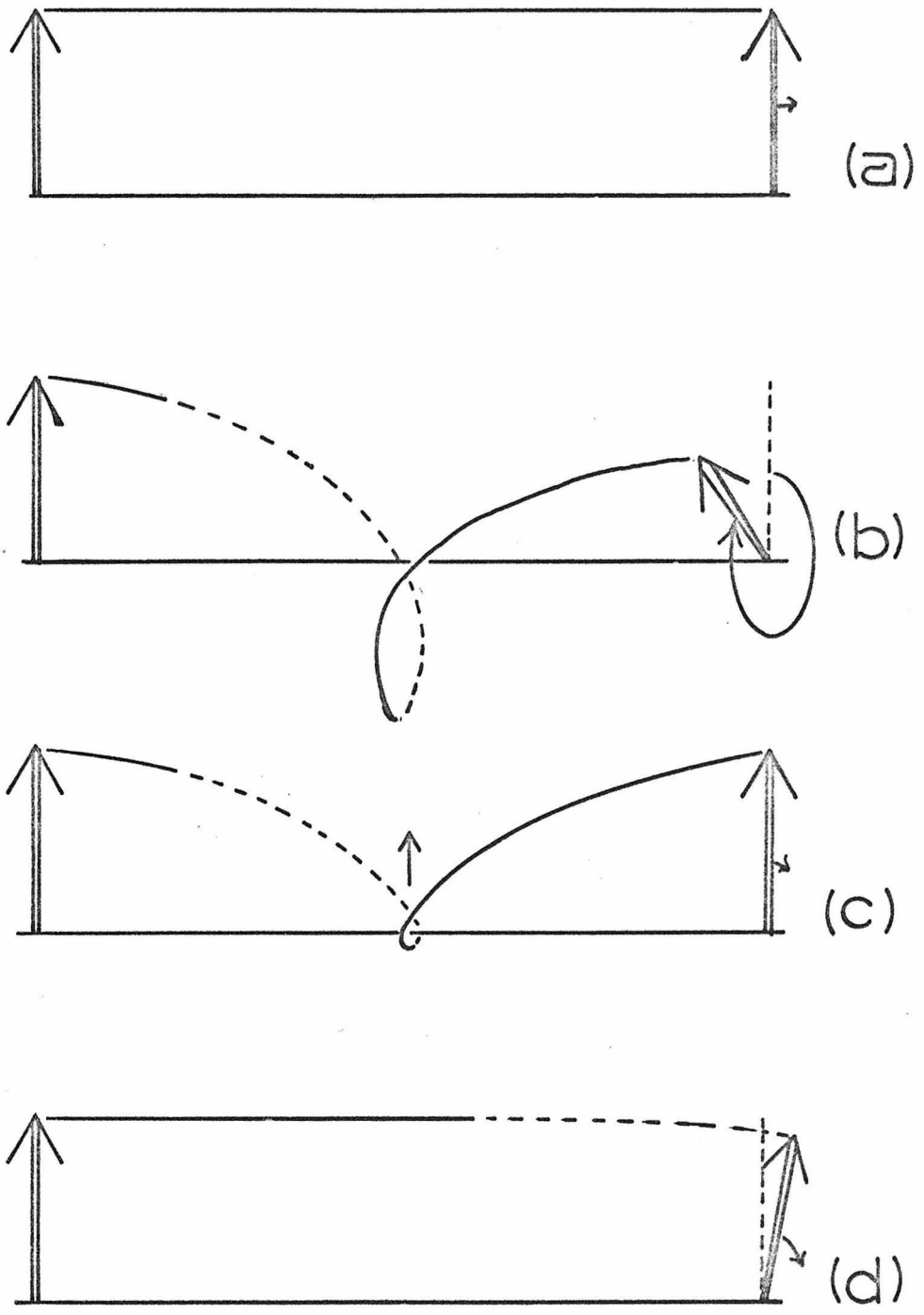
(a)
(b)
(c)
(d)

integral multiples of the incident frequency (Fig. 2.2c). Thus the dc current-voltage characteristic can be used to monitor the high frequency response of these quantum interference devices.

2.3 Critical Current of Proximity Effect Bridges

The critical current of the proximity effect bridge has three distinct temperature ranges (Fig. 2.4a), two of which are determined by the physics of superconductivity while the third is set by thermal heating. The two of physical interest are delineated in temperature by the intrinsic transition temperature, T_{cw}, of the weakened section if it were isolated and not adjoined by the stronger superconducting sections. This temperature is not a measurable quantity in other bridge geometries (Dayem-Anderson, point contact, etc.). The three critical current temperature zones are as follows:

(1) In the highest temperature range, between the actual and intrinsic transition temperatures of the bridge region, the critical current grows exponentially in temperature over several current decades,

$$I_c = I_o \exp(-\beta (T - T_{cw})^{\alpha}) \qquad (2\text{-}2)$$

where T_{cw} is the intrinsic transition temperature the bridge region would have if it were isolated. Typically $\frac{1}{2} \leq \alpha \leq 1$ and $5 \leq \beta \leq 30$.

(2) Below T_{cw} the critical current is proportional to $(T_{cw} - T)^{3/2}$ for several more decades of increase.

(3) At the lowest temperatures the critical current becomes metastable due to Joule heating or magnetic effects and there is a very slow increase in critical current with decreasing temperature.

Fig. 2.4

Typical critical current, I_c , dependence on temperature, T , of a proximity bridge is plotted in (a). There are three temperature regions of interest. In the highest temperature range, from T_{cw} to T_{cb} , the critical current dependence is exponential, in this case $I_c \propto \exp -\beta(T - T_{cw})^{1/2}$. This temperature range, being above the "intrinsic" superconducting temperature of the bridge region, T_{cw} , exhibits superconductivity in the bridge that has been induced by the adjoining strong superconductors. Part (b) is a plot of this "exponential tail" of the critical current. The second temperature range of critical current is below T_{cw} and is of the form $I_c \propto (T_{cw} - T)^{3/2}$. This dependence is correct for thin homogeneous films with uniform current density. Thus in this region the proximity of the strong film does not seriously affect the superconducting behavior of the bridge. The temperature T_{cw} is obtained by extrapolating the straight line section of graph (a) to zero critical current. This value agrees experimentally with large regions of superconducting film weakened to the same thickness as the bridge region; such a large region does not have its transition temperature changed by strong superconducting neighbors. The third critical current temperature range starts about $.5^{o}K$ below T_{cw} and is evidenced by hysteresis in the critical current. I_c continues to increase with lowered temperature but not as fast as $(T - T_{cw})^{3/2}$.

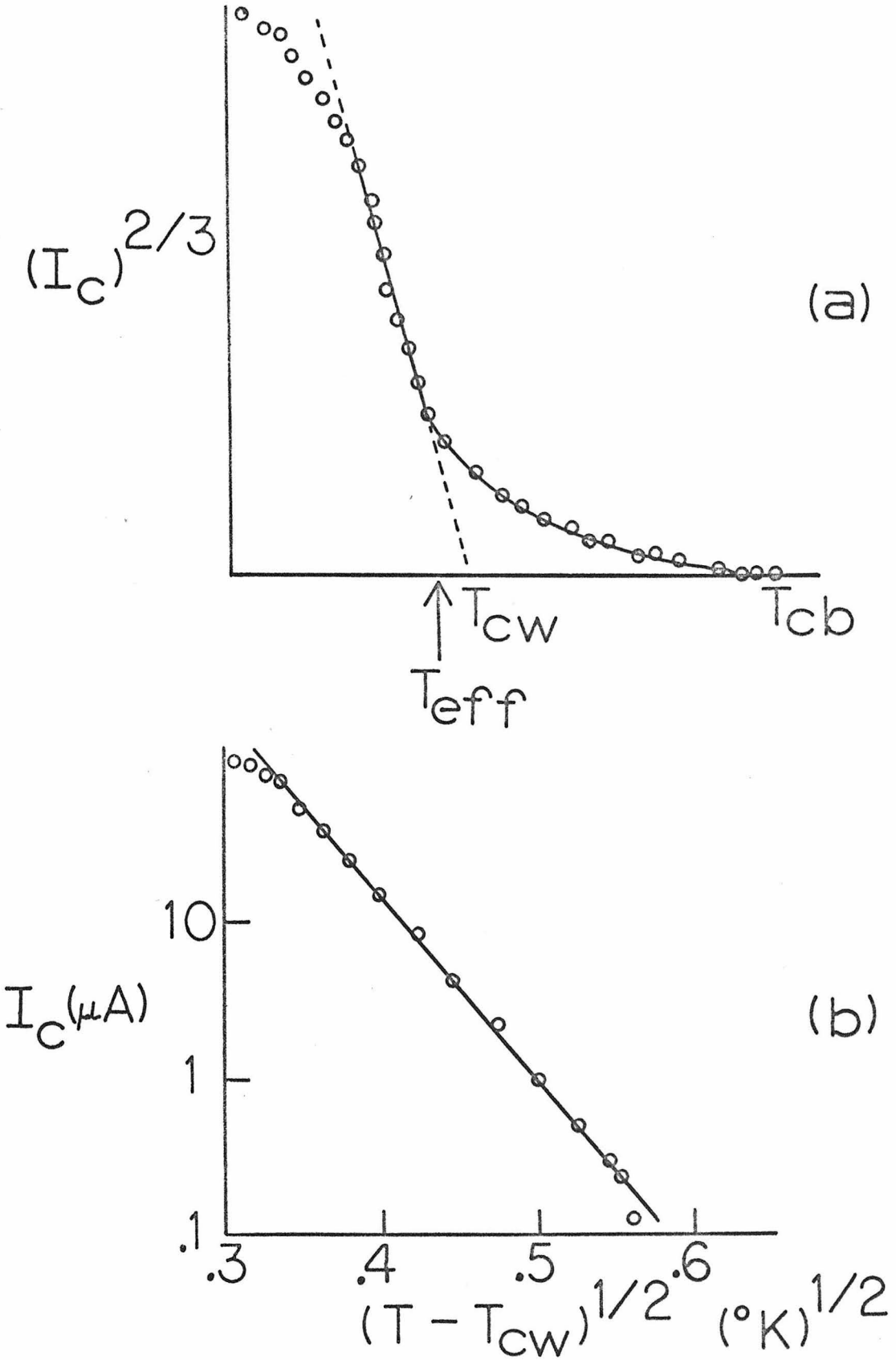
$(I_c)^{2/3}$
(a)
T_{cw}
T_{cb}
T_{eff}
10
1
.1
$I_c(\mu A)$
(b)
.3
.4
.5
.6
$(T - T_{cw})^{1/2}$ $(°K)^{1/2}$

J. Bardeen showed from the BCS theory of superconductivity that a homogeneous superconducting thin film which supports a uniform current density has a critical current dependence of $I_c = A(T_c - T)^{3/2}$ where T_c is the transition temperature of the film.[11] Therefore, the growth of critical current as $(T_{cw} - T)^{3/2}$ in these thin film uniform current distribution bridges below T_{cw} is not unexpected and indicates that in this temperature range the adjoining superconductors do not materially alter the critical current of the weak section. T_{cw}, the intrinsic transition temperature of the bridge, was measured by finding T_c for a large region of the thin film (100μ square) which had been etched to the same thickness as the bridge region and also by extrapolating the $(T_{cw} - T)^{3/2}$ curve to the $I_c = 0$ point (Fig. 2.4a). These two techniques give corresponding results to within experimental accuracy.

Above T_{cw} the intrinsic pair density of the bridge region is zero but the proximity of the adjoining strong superconducting films now has a profound effect on the supercurrent. Pair diffusion from S to N across the S/N interface causes a state of virtual superconductivity to occur in N with the pair density distribution ρ_s decreasing exponentially with the distance into the normal region. This dependence is shown in equation 2-3a or 2-3b depending on the relative size of the mean free path, ℓ, and coherence length, ξ.[12]

$$\rho(x) = \rho(0)\exp(-2Kx)$$

$$\text{if } \ell < \xi \qquad K^{-1} = \left(\frac{hV_F\ell}{6\pi k_B T}\right)^{1/2} \tag{2-3a}$$

$$\text{if } \ell > \xi \qquad K^{-1} = \frac{hV_F}{2\pi k_B T} \tag{2-3b}$$

The microscopic theory for this effect was first derived by DeGennes[12] (see section 1.4), however, the physics is essentially that a pair formed in S has a finite lifetime in N. That lifetime is roughly the time necessary for the thermal energy kT to break the pair $\sim h/kT$. Thus the spatial extent of this effect is roughly how far the electron can travel at the Fermi velocity, V_F, in this time, $\sim(hV_F/kT) = K^{-1}$ as in eq. 2-3b. If the lifetime is also foreshortened by mean free path effects, the result is eq. 2-3a.

For this work these results must be modified because N is really a superconductor above its transition temperature, T_{cw}. This situation has also been investigated theoretically[13] and results in a dependence such as shown in eqs. 2-3a and 2-3b but with T replaced by $(T - T_{cw}) = \Delta T$ for $\Delta T/T < 1$.

The bridge critical current scales as the lowest density of pairs in the bridge, that is, the density at the center farthest from the interfaces, ρ_w. By definition the critical current $j_c = \rho_c v_c$. In the microscopic theory of a homogeneous superconductor the pair density ρ is proportional to $N\Delta(\Delta/E_F)$, where Δ is the superconducting energy gap, E_F is the Fermi energy, and N is the normal electron density at the Fermi surface. The critical velocity, v_c, changes the kinetic energy of the electrons by the energy gap, that is, $(1/2)m(v_F+v_c)^2 - (1/2)mv_F^2 = \Delta$. Thus $v_c \propto \Delta$ and $j_c \propto \Delta^3 \propto \rho^{3/2}$. To demonstrate that the proximity effect is responsible for this excess current above T_{cw} the experimental exponent, $(T - T_{cw})^{\alpha}$, must be compared with the predicted proximity effect exponent, K(L). This

comparison was done in three ways. First, the magnitudes of the calculated and experimental exponents were compared in several different bridges. Next, for a given T_{cw} the length of the bridge was varied and checked against the measured β. Third, using the resistivity as an indication of the mean free path, the change in β on ℓ was noted. All three methods substantiated the assumption of proximity effect causing the excess current.

For typical Nb/Ta proximity effect bridges of short mean free path, α was empirically 1/2, thus it was necessary to compare β with the K appropriate for $\ell < \xi_o$. Though I_c scaled with ρ_w the exact theoretically expected functional dependence for this geometry is unknown. Fortunately, this unknown only enters this order of magnitude calculation as a factor between 1 and 2. A reasonable estimate of the factor can be made by considering the superflow as similar to the homogeneous case outlined above, $j_c \propto \rho^{3/2}$. For a one-dimensional superconductor near T_c, I_c is proportional to $(\Delta T)^{3/2}$ and ρ is proportional to ΔT, thus it is not unreasonable to assume I_c as proportional to $(\rho)^{3/2}$. Thus

$$I_c \propto \exp[-\beta(\Delta T)^{1/2}] \propto (\exp(-2Kx))^{3/2} \qquad (2\text{-}4a)$$

resulting in

$$\beta = 2(3/2)KL/2 = (3)\left(\frac{6\pi\, k_B}{h\, V_F \ell}\right)^{1/2} \frac{L}{2} \qquad (2\text{-}4b)$$

Using $V_F = 10^6$m/sec, $L = .5\mu$, and $\ell = 100\text{Å}$ gives $\beta = 12$. Five Nb/Ta bridges and films that were described by these parameter values had a range of measured β from 7 to 15. This agreement was slightly

fortuitous considering the lack of certainty with which the variables V_F and ℓ could be known.

For proximity effect bridges the exponential temperature dependence of the critical current ranged between ΔT and $(\Delta T)^{1/2}$. Bridges with longer mean free paths as calculated from resistivities tended to have the ΔT dependence as expected from eq. 2-3b of the proximity effect, but the exact dependence could not be confirmed in detail in these small geometries.

To check the variation in length of β, a tungsten on tantalum film was used to form four bridges of different lengths, .4 - 2μ. Since the bridges were formed by etching off the W overlay film everywhere except along a fine dividing line, the transition temperature of the original film can be used as T_{cw}. The critical current of all bridges for $T_{cw} < T$ was exponential with the exponent proportional to $(T - T_{cw})$. β is linearly proportional to bridge length L. On this film β had to be measured taking into consideration the temperature dependence of the pair density in the strong film. Figure 2.5b shows a plot of β versus bridge length L, experimentally confirming the length dependence indicated in the proximity effect exponent.

Accurate critical current data were obtained for bridges of different materials with resistivities differing by a factor of 8. Using the resistivity to estimate the mean free path ℓ the exponent β was calculated for bridges in Nb/Zr, Nb/Ta/Zr, Nb/Ta, and Sn/Au. As predicted by eq. 2-3a, β-experimental scaled as $(V_F\ell)^{-1/2}$ to within a factor of two. β ranged from 6 for Sn/Au to 30 for Nb/Zr. Again the

Fig. 2.5

T_{cw} is well defined for bridges made on W/Ta films; in particular $T_{cw} = 3.7^{o}K$, the transition temperature of the untouched film (a). The variation of the critical current on bridge length can to a first approximation be considered a change in the exponential coefficient β in the dependence $I_c \propto \exp(-\beta\Delta T)$. For very short bridges, where the operating temperature is close to the transition temperature of the strong film, the strong film pair density dependence on temperature must be taken into account in calculating β from the experimental data. This compensated, empirical β is plotted as a function of length in part (c). This approximately linear dependence of β on L is consistent with the proximity effect explanation of critical current.

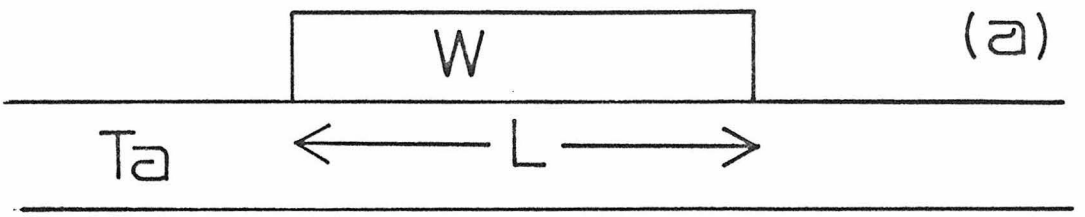
W
(a)
Ta
L

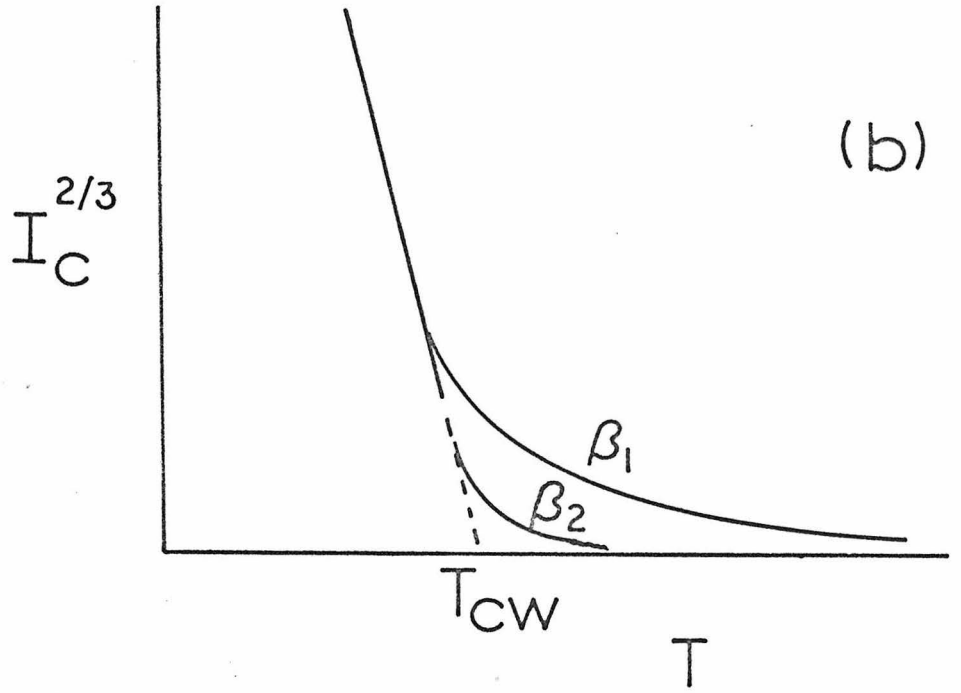
(b)
$I_c^{2/3}$
β_1
β_2
T_{cw}
T

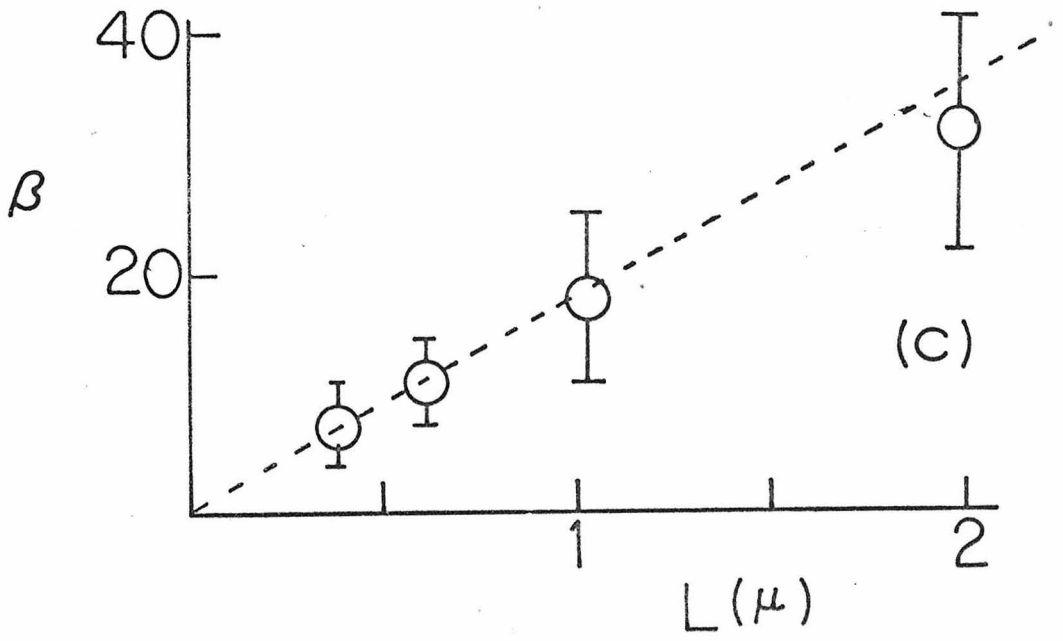
40
20
β
(c)
1
2
L(μ)

Fermi velocity could not be directly measured but was estimated by using the bulk value of the material.

For an experimentally useful bridge, at best 2 decades of critical current could be monitored in the exponential tail region of the temperature dependence. Also, the internal bridge noise and outside interference tended to make ambiguous any measurements below 1μA. These considerations limit the accuracy of the constants enumerated above.

2.4 Thermal Considerations of Proximity Effect Bridges

In describing this investigation an attempt is being made to adhere to the macroscopic quantum treatment of superconductivity. However, it must be recognized that this "quantum state" exists in intimate contact with the massive "classical" system of normal electrons, with individual electrons continuously transferring from one system to the other. Nevertheless , most of the features of this combined system can be described simply as the sum of the action of the two components: one, a macroquantum state; and the other, a normal electron gas. Thus currents are assumed to be the sum of a supercurrent, I_s , plus a normal current, I_n . These normal currents, at finite voltages, dissipate energy and under these conditions the macroquantum state must be regarded as in intimate contact with a heat source and sink. One rather remarkable result of this work has been to experimentally verify that even in extreme non-equilibrium conditions the major effects of this combination of super and normal states can be described in terms of the resistance of the normal state and the consequent dissipation (I_n^2R).

Despite good thermal coupling between the refractory films and their sapphire substrates, one millivolt across a proximity effect bridge caused considerable temperature rise in the bridge region (see Appendix C for experimental details and calculations). The rise in bridge temperature δT was linear in Joule heat for $\delta T/T_{bath} < .1$, therefore δT increased as the square of the current bias. For example, a standard Ta bridge region (10μ x $.5\mu$ x 100Å, with $R = .1\Omega$) experienced $\delta T = .01^{o}K$ at $100\mu A$ and $\delta T \sim 1^{o}K$ at 1 mA.

When this standard bridge was tested at 1 mV (10 mA) to find the 500 GHz Josephson step in the I-V curve, the bridge region rose well above $T_{cw} \sim 4^{o}K$ no matter what the bath temperature. Thus no coherent response existed at 500 GHz regardless of quantum considerations. Higher resistivity films lessened the Joule heating problem, but higher resistivity necessitated much shorter bridge length eventually reaching the limit of optical microscope technology.

Many Josephson-like couplings show hysteresis in critical current.[14] Such hysteresis also exists at high critical currents (> 200 μA) in the typical proximity effect bridge, and in this investigation was explained as a thermal effect. The bridge temperature increased while changing from the zero resistance to the normal resistance state. The temperature increase corresponded to a decrease in I_c. Hence the critical current with increasing bias, $I_{c\text{-up}}$, was greater than with decreasing bias, $I_{c\text{-down}}$, since the bridge temperature was different.

Both high frequency cutoff and initial rise hysteresis have possible alternate quantum explanations, but in the case of proximity

effect bridges a sufficient explanation is simply Joule heating.

2.5 The Temperature, Length, and Frequency Boundaries of Proximity Effect Weak Coupling

Describing the interference wave function overlap using the proximity effect makes it possible to relate the experimental limits on the temperature, bridge length, and frequency ranges over which quantum interference can exist to the geometry of the wave function. In addition to the simple existence of quantum interference, a qualitative change in the nature of interference occurs as these parameters change and can be described as a modification of the boundary region of the macroscopic wave functions. This qualitative change can be analyzed in terms of the relative value of the two coefficients in eq. 1-11, $f^2(\nabla f/f)$ and $f^2\nabla\theta$, by calculating f from the proximity effect.

Most parameter ranges for quantum interference can be gleaned from the plot of critical current versus temperature (Fig. 2.4a). For example, if β is large ($\beta > 50$) then the exponential tail of the critical current is not observable and there are no Josephson-like interference effects. Instead the bridge region acts bulk-like with $I_c \propto (T_{cw} - T)^{3/2}$. If β is made smaller, by changing the material parameters ℓ or V_F or the bridge length L, the exponential critical current temperature range $T_b - T_{cw}$ and the maximum proximity effect critical current, $I_c(T_{cw})$, are both increased. In general, when the superconductivity of the bridge region is due primarily to proximity electrons ($T > T_{cw}$) the quantum coupling is weak and the interference is Josephson-like, whereas below T_{cw} as the pair density becomes large

and due mostly to the intrinsic superconductivity of the bridge region, the coupling is strong and the interference is better explained as a phase slip process. The rest of this section will show that the value of β essentially determines the following: the quantum interference temperature range, the maximum bridge length, and the highest coherent frequency interference. The only other major influences that limit the operational range of the bridge interference are Joule heating, which sets the lower temperature and lower bridge length limits, and Johnson noise, which determines the low frequency limit to interference.

First, the quantum operational temperature range can be extracted from the critical current plot. Experimentally a critical current I_c below .5 μA becomes difficult to identify because internal noise broadens the voltage rise at I_c to around 1 μA. Correcting for this broadening, a qualitative change in the "critical current" has been monitored at about 5×10^{-8} μA.[15] This corresponds closely to the minimum critical current necessary to ensure the coupling energy of the two-wave functions is greater than the thermal fluctuation energy

$$kT < I_c\Phi_o$$

The wave function energy $I_c\Phi_o \sim (1/2)I_c^2 L_{bridge}$ is the maximum energy that can be added to the coupling region before a voltage develops between the two-wave functions.[16] Thus T_{cb}, the upper temperature limit on quantum interference, can be defined as the temperature where $I_c > 5 \times 10^{-8}A = kT/\Phi_o$, although in a standard test $I_c > 5 \times 10^{-7}A$ is a more practical criterion. All quantum interference effects are seen at these small critical current levels: the existence of a critical

current, induced rf steps, and periodic critical current modulation of I_c with magnetic field.

The lowest temperature (and therefore strongest coupling) at which quantum interference can occur is a bit harder to describe. At T_{cw} the critical current that exists is solely due to the proximity effect and is comparable to the maximum current width of the rf induced steps for that bridge; thus $I_c(T_{cw})$ is an experimental measure of the maximum interference. However, quantum interference exists at bath temperatures well below T_{cw}. Thus although the bridge region has become intrinsically superconducting, the interference coupling between the two strong superconductors continues at these lower temperatures. Practically, thermal hysteresis sets in about $.5^{o}K$ below T_{cw} and the bridge temperature for these large currents has become significantly different from the bath temperature.

Secondly, the range in possible bridge lengths can also be determined from critical current considerations. The proximity pair density diffusion length, $K^{-1}/2$, is longest at T_{cw}. Using the measured critical current $I_c(T_{cw})$ and calculating the corresponding value for the pair density, $K_{max}^{-1}(T_{cw})/2$ leads to $1500\mathring{A}$ for Sn/Au and $1100\mathring{A}$ for Nb/Ta. The longest bridge is then one whose center density, ρ_c, supports $I_{c\text{-}min} = 3 \times 10^{-8}A$ and $\rho_c \exp(L/K^{-1}) = \rho_{strong}$. This approximation assumes an exponential dependence of pair density up to the interface and a pair density match at the interface. Neither of these assumptions is rigorously true but to the accuracy that the bridge lengths can be measured no error is introduced. Putting in typical K_{max}^{-1} values for Nb/Ta films implies 2.9μ as the longest bridge that

would still have quantum interference effects. Experimentally the cutoff in length is at 2μ. Longer bridges with the consequent larger β have small temperature ranges where the proximity coupling exists alone. Through most of the operational range the strong coupling limit applies, that is, the second term in eq. 1-11 dominates with coefficient $f^2\nabla\theta$. Experimentally, as the bridge gets longer, the rf harmonic structure is washed out and the maximum fundamental step width is a small fraction of the critical current. The magnetic modulation of the critical current is not complete and consists of only a few periods.

The practical limit on minimum bridge length is thermally determined. Experimentally to make a short $L = .3\mu$ bridge it is necessary to depress T_{cw} and shorten the mean free path of the bridge film so that only small critical current values are obtained below T_{cs}. If instead the critical current of the bridge is large, that is, if the coupling is strong at all temperatures except near T_{cs} (where even ρ_s is small) then the bridge Joule heating when biased above I_c will raise the bridge temperature above T_{cs}. Thus there is no effective operating temperature range for such strong coupling, however, high resistivity material with very short bridge length could perhaps operate in this strong coupling range. In short very depressed ($T_{cs}/T_{cw} > 2$) bridges operated above T_{cw} the interference coefficient $f^2(\nabla f/f)$ dominates and the magnetic field and rf interference behavior become more Josephson-like compared to the longer bridges. That is, the rf power dependence of the steps and the magnetic modulation of the critical current resemble those of a tunnel

junction. The magnetic modulation of the critical current is complete and periodic for 10 or more periods. The maximum rf step current width is comparable to $I_c(T_{cw})$.

Thirdly, the upper frequency limit to interference seems to be determined by the density of proximity electrons in the central region of the bridge. This can be shown as follows. The energy gap of a homogeneous superconductor can be shown to be the following function of temperature,

$$\Delta(T) = \Delta(0)\,[(T_{cw} - T)/T_{cw}]^{1/2} \qquad (2\text{-}5)$$

However, when the proximity effect has induced more superconducting electrons in the region than would exist intrinsically, an effective $\Delta(T)$ can be estimated from the magnitude of the critical current. Consider $I_c(T_{cw})$ as a measure of the maximum superelectron density due to the proximity effect. The same critical current would exist in an isolated bridge region were it at T_{eff} as indicated in figure 2-4a,

$$I_{c\text{-bridge}}(T_{cw}) = I_{c\text{-isolated weak}}(T_{eff}) \,.$$

$\Delta(T_{eff})$ can be considered the equivalent gap in the weak link at T_{cw} . Experimentally, the maximum frequency interference seen by a proximity effect bridge corresponds to $2\Delta(T_{eff})/h$ to within a factor of 2 . This argument assumes that the heating does not limit the measured maximum frequency interference before this gap limit (see Appendix C). When the temperature is lowered well below T_{cw} so that the density is not only the proximity density but the intrinsic density as well, the high frequency limit is still governed by the proximity density only.

The low frequency limit has been discussed in the literature[17] and is caused by the internal Johnson noise of the bridge. Standard Nb/Ta bridges with .1Ω resistance have ∿50 MHz as a lower interference limit if $I_c \geq 1$ μA .

An equivalent way of looking at the problem considers the gap as a function of position within the bridge

$$\Delta_{eff} = \Delta_o \exp(-Kx)$$ where x is the distance from the interface.

The high frequency interference is limited by the Ginsburg-Landau frequency, $\nu_{G-L} = 2\Delta_{eff}/h$, in the center coherence length of the bridge.

2.6 RF Responsivity of Proximity Effect Bridges

Changes in the I-V characteristics of proximity effect bridges induced by low levels of microwave radiation can be analyzed to compare the internal time dependent pair currents of bridges with Josephson tunnel junctions. Minimum detectable perturbation of the current biased quantum mechanical interference was achieved with low power level rf incident radiation tests. By chopping the incident rf and monitoring the bridge voltage with a lock-in amplifier tuned to the chopping frequency, it was possible to detect changes in the I-V characteristics induced by 10^{-17}W; this method measures the rf responsivity of the bridge (see Appendix B).[18]

The results of these measurements agreed well with the expressions used for rf step widths for the resistance shunted tunnel junction.[19] These expressions are, for the zero step (critical current)

$$I_o = I_c J_o(2eV_{rf}/h\nu)$$

and for the first step

$$\Delta I_1 = I_c J_1(2eV_{rf}/h\nu)$$

For small V_{rf} these terms reduce to

$$I_c - I_o = I_c(2eV_{rf}/h\nu)^2 \qquad (2\text{-}6a)$$

$$\Delta I_1 = I_c(2eV_{rf}/h\nu) \qquad (2\text{-}6b)$$

The rf responsivity at a current bias, I_B, is the change in the time average voltage measured across the bridge with and without incident rf radiation (Fig. 2-6). This change in voltage for I_B slightly above I_c is

$$V_{res} = (\Delta I_c)(dV/dI)_{I=I_B} = I_c(2eV_{rf}/h\nu)^2 \, (dV/dI)_{I=I_B} \qquad (2\text{-}7)$$

At the first step the maximum responsivity measured is equal to the width of the step, ΔI_1, times the change in differential resistance induced over this region. Experimentally the change in differential resistance at the first step is proportional to V_{rf}/ν for small rf levels. Thus

$$V_{res} = (\Delta I_1)\, \delta(dV/dI) \propto I_c(2eV_{rf}/h\nu)^2 \qquad (2\text{-}8)$$

The experimental responsivity measurements agree with the predictions based on a resistance shunted current biased tunnel junction in all respects except the frequency fall off. For example, both the

Fig. 2.6

(a) Plot of I-V characteristics of a proximity effect bridge with and without incident microwave radiation. The application of microwaves depresses the amount of initial supercurrent and induces constant voltage steps into the characteristics.

The voltage difference of the two curves in (a) is plotted as a function of bias current in graph (b). This difference is called the rf responsivity.

(c) For small rf powers near the critical current, the responsivity signal, V_r , can be analytically expressed as the product of the decrease in critical current, (ΔI_c) times the slope of the I-V characteristic, dV/dI.

(d) The maximum responsivity signal, V_r , near a voltage step for small rf powers is the current width of the step, ΔI_1 , times the local difference of slope of the two characteristics, $\Delta(dV/dI)$.

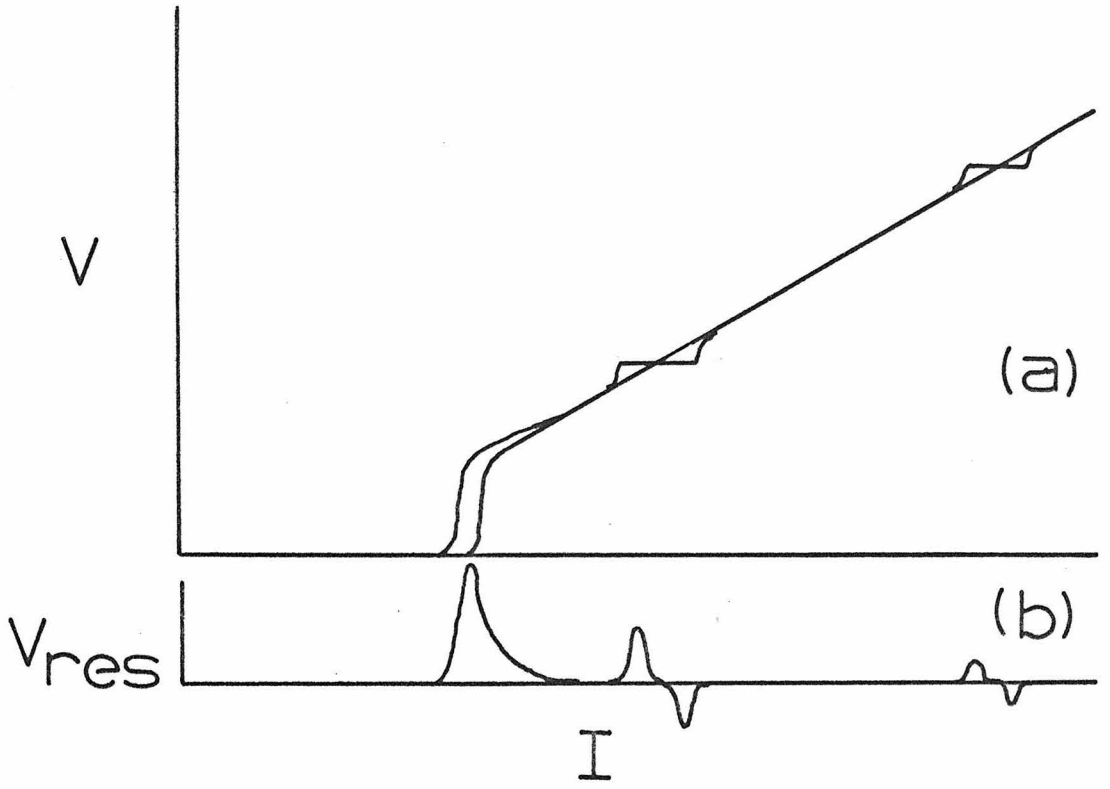

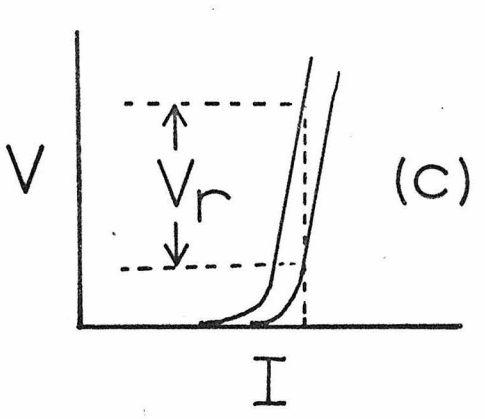

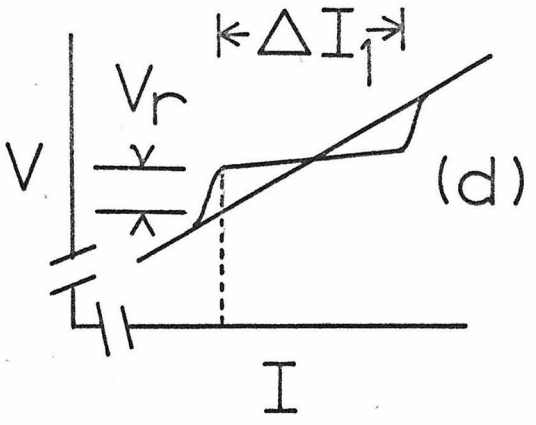

$$V_r(I_B) = (\Delta I_c)\left(\frac{dV}{dI}\right)\Big|_{I_B}$$

$$V_r(I_B) = (\Delta I_1)\left(\Delta\frac{dV}{dI}\right)\Big|_{I_B}$$

responsivity at I_c and I_1 were proportional to I_c and the incident rf power over many decades (Fig. 2.7). However, the frequency dependence of the responsivity as measured at 10, 35, and 96 GHz did not obey the $1/\nu^2$ rule, but rather decreased approximately as $1/\nu^3$ (Fig. 2.8).

This functional dependence of responsivity on absorbed power, critical current, and frequency can be understood in terms of an effective impedance for the bridge. The quantum mechanical voltage-frequency relation ($2eV_e = h\nu$) for these bridges implies that the voltage V_e is the equilibrium potential maintained between the two strong superconductors, while the power absorbed, $P = \overline{V}_n^2/R$, is that due to dissipation within the normal electronic state. Thus V_e and V_n are not necessarily the same in these non-equilibrium conditions[20] and the exact interrelation of V_e and V_n will depend on the details of the electronic process in the weak region. However, some aspects of this dependence can be anticipated from a "lumped circuit model" which contains some of the physics of these complex effects.

The high characteristic impedance of radiation from free space or a waveguide makes these low resistance, small-sized bridges essentially microwave current biased. Microcalorimetry tests (see section C.5) at high dc and rf voltages proved that over these operational ranges the bridge impedance could be treated as strictly resistive with regard to the absorption of radiation. However, for small voltages, where the superconducting and Josephson nature of the bridge are still dominant, the bridge impedance is unknown. There are at least two possibilities for simple estimates of internal impedance: one is that the interference

Fig. 2.7

(a) As the temperature is decreased below the bridge transition temperature, T_{cb} , the maximum rf responsivity near I_c , V_{res} increases exponentially in $(T - T_{cw})$.

(b) This increase is experimentally proportional to the critical current within the exponential range of critical current growth, $T > T_{cw}$.

(c) Over a large dynamic rf power range the maximum rf responsivity near I_c scales as the incident power.

All three graphs are also representative of the rf responsivity signal present at the first quantum interference step. Thus the dependence on I_c and rf power of the proximity effect bridge for small power levels of microwaves is in agreement with the resistance shunted tunnel junction description.

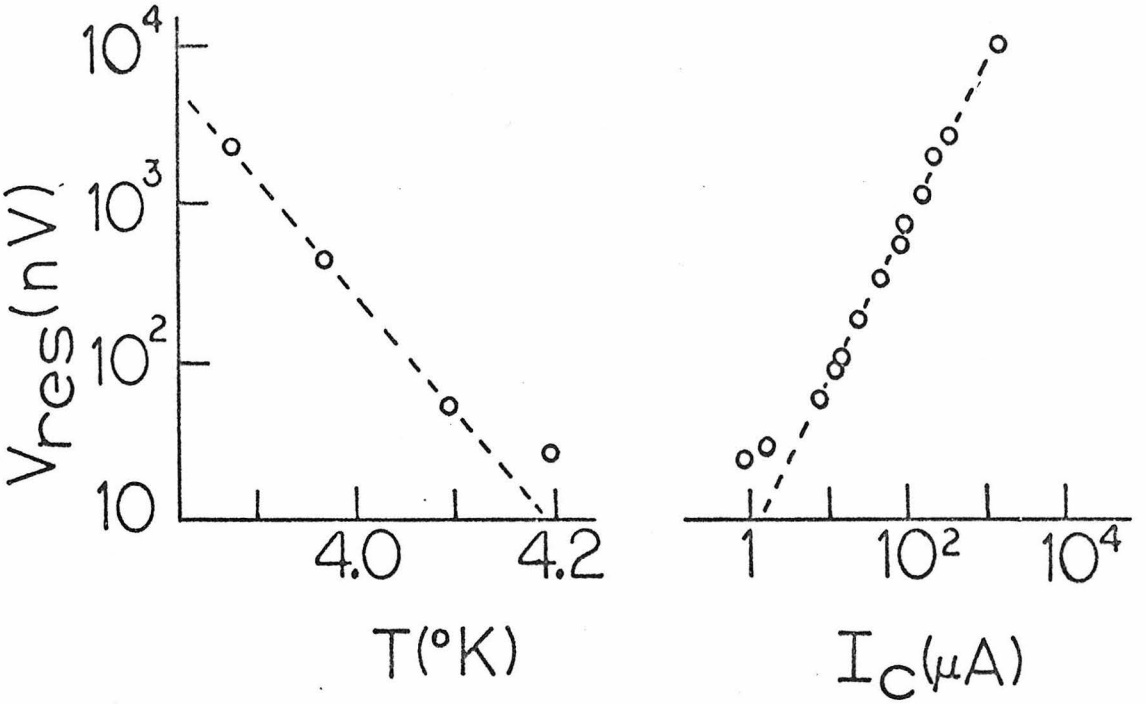
10^4
10^3
10^2
10
V_{res}(nV)
4.0
4.2
T(°K)
1
10^2
10^4
I_c(μA)

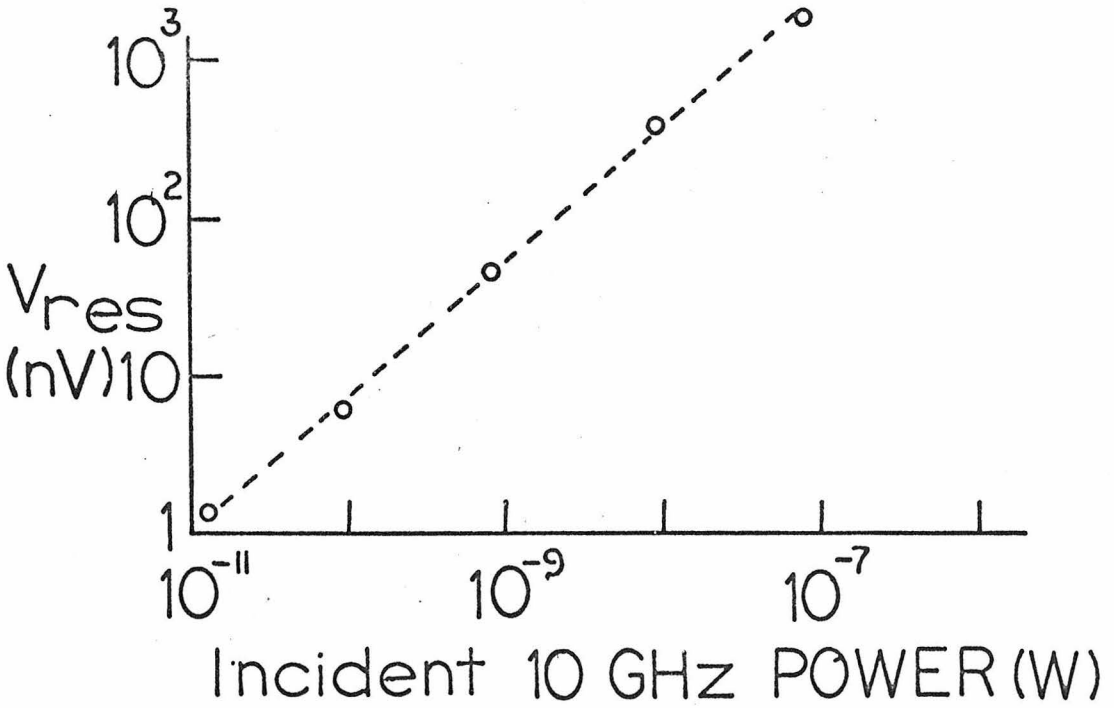
10^3
10^2
V_{res}
(nV)10
1
10^{-11}
10^{-9}
10^{-7}
Incident 10 GHz POWER (W)

bridge is shorted by some effective capacitance, a second is that the interference element should be considered as in series with a "kinetic inductance"[21] associated with the supercurrent (Fig. 2.9). Geometric estimates of this shorting capacity yield 10^{-12}F, while estimates of kinetic inductance are $10^{-11} - 10^{-12}$H. Both equivalent circuits are consistent with the frequency independent absorption measurements taken at high voltage levels where quantum interference has ceased, and produce the same I-V characteristics at low voltages that are produced by the simple resistance shunted tunnel junction.

To explain the $1/\nu^3$ responsivity dependence on the shunt capacitance in the frequency range 10-100 GHz would require $C \geq 10^{-9}$F (Fig. 2.9a). This needed capacitance is much larger than calculations and LC circuit tests indicate.

The bridge inductance, however, can divide the rf voltage and cause the responsivity to have a frequency dependence more rapid than ν^{-2}. Figure 2.9b gives a possible equivalent circuit for a proximity effect bridge. R_b is the normal electron path and R_c, L_B, and current source X represent the superelectron path. The current source obeys $I_J = I_o(1 + \cos \frac{2e}{h} \int V(t')dt')$, where V is the voltage across R_c. With this circuit a microwave current, I_{rf}, gives rise to an rf voltage across the bridge

$$(V_{rf})_B = I_{rf}R_bR_c/(R_b + R_c + i\omega L)$$

If $R_c = R_b = 2R_{bridge}$ the peak voltage across the bridge becomes

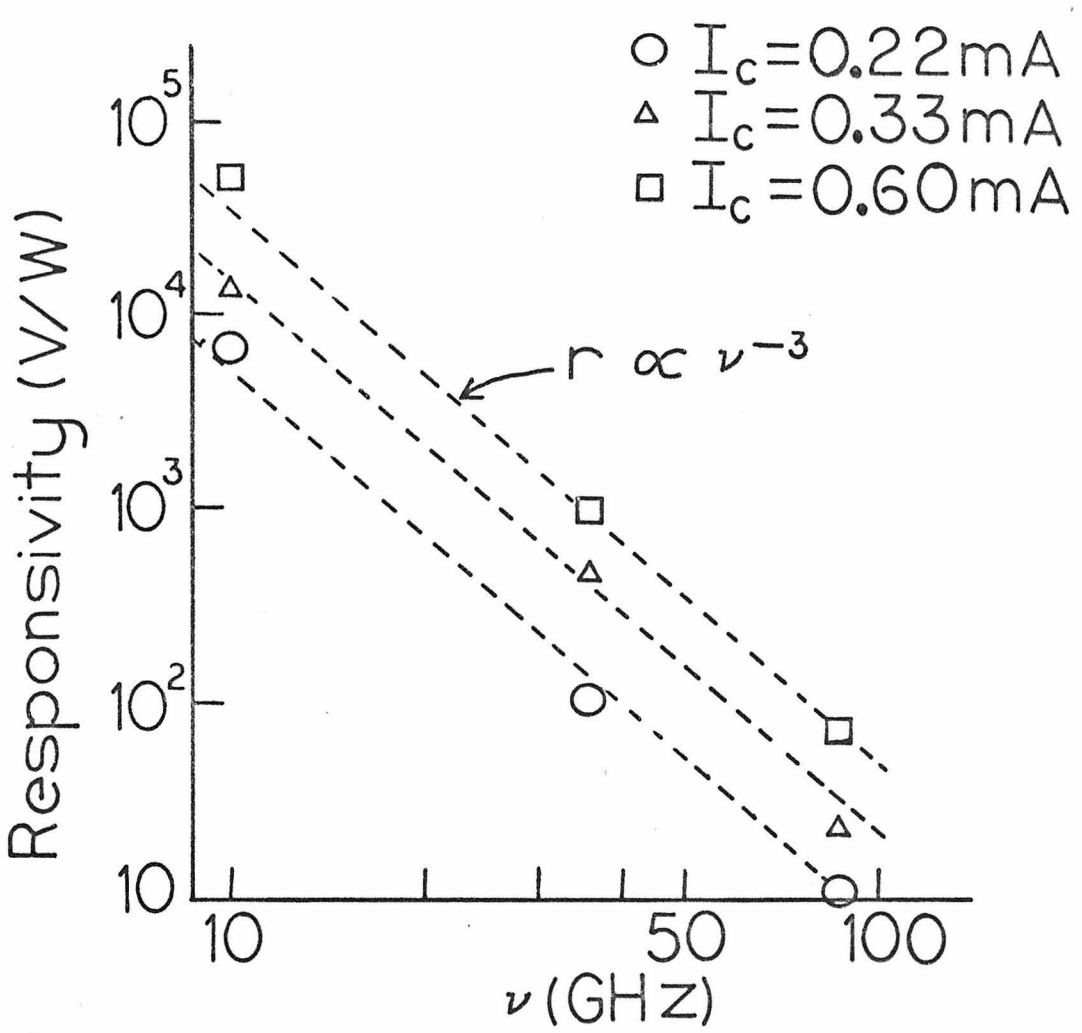

Fig. 2.8 In contrast with the tunnel junction predictions and experiments, the dependence of responsivity on frequency for the proximity effect bridge is as $\sim 1/\nu^3$. Typical results for three different temperatures at 10, 35, and 95 GHz of a Nb/Ta proximity effect bridge are plotted.

Fig. 2.9

Possible equivalent circuit representations of the proximity effect bridge which produces $1/\nu^3$ dependence of responsivity when rf current biased. In both circuits the current source marked with an X obeys the Josephson-like frequency-voltage law, $I_s = I_c(1 + \cos 2e/h \int_0^t V(t')dt')$. Both circuits produce the standard I-V bridge characteristic with just a DC bias current present.

(a) The capacitance necessary to match the experimental responsivity results is $C = 10^{-9}F$, a value completely inconsistent with the geometric calculation of $10^{-12}F$ and simple measurements made with a bridge in a resonant LC circuit.

(b) Letting $R_b = R_c = 2R_{bridge}$ allows this equivalent circuit to reproduce the standard I-V curves of proximity effect bridges. The left current path can be considered for superconducting electrons and the right path for the normal electrons. The fact that the voltage across R_c does not necessarily equal that across R_b can be interpreted as a nonequilibrium situation in which the normal and pair potentials are different. To match the experimental responsivity data, the time constant of this circuit must be such that $L \sim 10^{-11}H$, a value consistent with estimates of the kinetic inductance of the bridge.

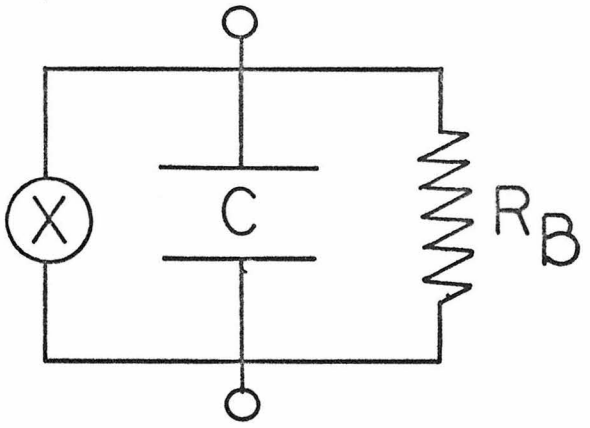

(a)

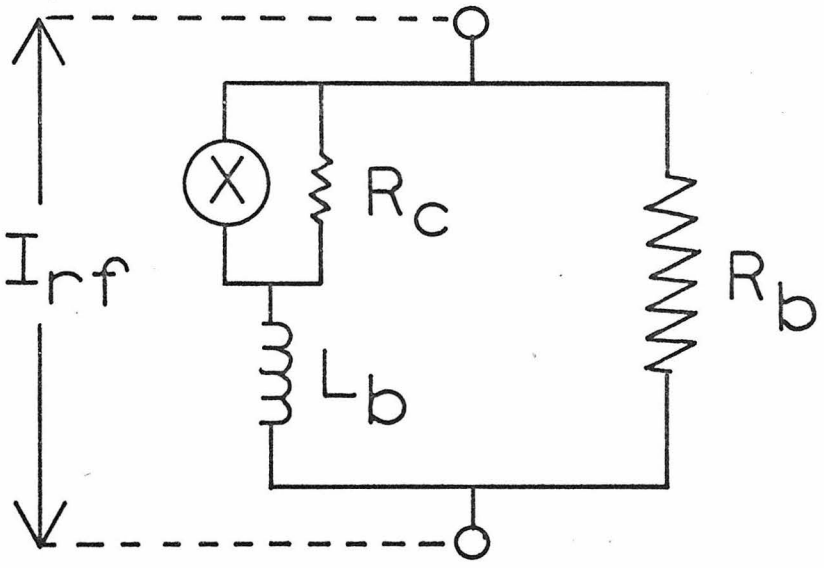

(b)

$$(V_{rf})_B \sim I_{rf} R_b^2 f/(R_b^2 + \omega^2 L^2)^{1/2}$$

This relationship explains the experimental $1/\nu^3$ dependence if $\omega^2 L^2 >> R_b^2$, a requirement satisfied is $\omega L = .3\Omega$ implying $L = 5 \times 10^{-12} H$.

Thus by considering the rf bridge impedance in detail it has been possible to explain the fast decrease in high frequency responsivity. An alternate or coexisting phenomenon which explains the $1/\nu^3$ responsivity dependence and the high frequency limit (section 1.5) relies on a phase slip recovery time, τ_s. Assume that the proximity superelectrons must diffuse back into the central coherence volume after a phase slip. For example, the amplitude in eq. 1-11 may recover as

$$\psi_o f(1 - \exp(-t/\tau_s)) \qquad (2\text{-}9)$$

where τ_s is the characteristic time of recovery. If the period of incident radiation is comparable to τ_s then the average amplitude of the proximity wave function is considerably less than the equilibrium amplitude, hence a decrease in responsivity is distinctly possible with increasing incident frequency. Assuming that the responsivity is proportional to the effective critical current that would result from this effective electron density, a value for τ_s can be calculated from the experimental fact that the (responsivity at 100 GHz/responsivity at 10 GHz) = .1 of the predicted value. This calculation gives $\tau_s = 10^{-11}$ sec. Two important points add credence to this calculation: (1) the 10 GHz responsivity numerically agrees with eq. 2-6a, whereas the 100 GHz responsivity is lower than the prediction by a factor of .1,

and (2) if superelectrons were really diffusing back into the central coherence volume the time constant would be about 10^{-12} seconds.

CHAPTER III

SERIES ARRAYS OF WEAKLY COUPLED MACROSCOPIC WAVE FUNCTIONS

A natural extension of the study of the single proximity effect bridge was the investigation of two or more bridges in series. Two intriguing reasons for studying bridge arrays were to find under what conditions the time dependent voltages in series bridges would synchronize both in frequency and phase, and to search for possible evidence of interactions involving more than two macroscopic wave functions. This investigation was the first (and only) successful fabrication of series arrays of identical superconducting quantum interference devices despite many attempts and widespread theoretical interest.[1] This research revealed that when series bridges were placed 2μ or less center to center a strong interbridge coupling existed which helped synchronize the frequency and phase of the internal oscillations. A synchronized array acted like a single Josephson device quantized as $2eV = Nh\nu$, where N is the number of bridges in the array.

The existence of intrafilm bridge coupling had no theoretical explanation or even prediction. Thus to explain the strong dependence of the array properties on bridge spacing two new intrafilm coupling processes have been introduced. The first explanation considers the direct interaction between neighboring bridges due to the nonequilibrium which exists between the normal and superconducting electron flow within the bridges (see Chapter II, section 6). This nonequilibrium condition extends one micron into the strongly superconducting material that separates the bridges, thus supplying a vehicle whereby the nonequilibrium

processes of one bridge can propagate to a closely placed neighboring bridge. The second explanation uses the possible quantum interference between next nearest wave functions (not the omnipresent interference between adjoining wave functions) to induce synchronism among neighboring bridges.

The discovery of this strong interbridge coupling, in addition to exposing more facets of the macroscopic wave function, also facilitates the use of the Josephson-like effects in three long-standing instrumentation problems. First, a frequency-voltage converter was made between GHz and millivolts (rather than microvolts for a single Josephson device) perhaps allowing the standard volt to be conveniently pegged to standard frequencies by use of the first rf step of a 1000 bridge array. A single Josephson device obeys $h\nu = 2eV$ so that the first 10 GHz step occurs at $\sim$ 20 μV; however, a 1000 bridge series would display the first step at (1000)(20 μV) = 20 mV. Secondly, current biasing a large array results in a voltage oscillation whose frequency can be tuned by simple current adjustment. Such a cryogenic, tunable oscillator has been tested from 10-500 MHz. Thirdly, the good impedance matches possible with high resistance arrays promise to finally allow the maximum sensitivity of bridge I-V characteristics to microwave radiation to be fully exploited. As shorter bridges become technically feasible the upper frequency range will be raised and submillimeter waves will be coherently detectable.

Section 3.1 will discuss the original observations on two bridge arrays which were the experimental tip of the iceberg . Experiments on large hundred bridge arrays will be enumerated in section 3.2. The last

section of this chapter will discuss the possible physical explanations of the experimentally discovered strong interbridge coupling, both as a natural extension of the nonequilibrium relaxation time discovered in single bridges and as evidence of interactions involving three-wave functions.

3.1 Two Proximity Effect Bridges in Series

The first extension of a single bridge was two in series. The two new phenomena of interest already developed with the double bridge. First, it was noticed that when the center-to-center distance of standard .5μ long bridges was less than 2μ the critical currents and rf step structure became suddenly coincident over a larger range of temperatures than would occur with longer spacing. The strong superconducting region between bridges could be adjusted from .2 - 1μ before either one long bridge resulted or a complete decoupling of behavior was noticed. Secondly, the internal oscillating voltages were in phase if the bridges were at the same time-average voltage either because they were identical and single biased or different and independently biased. To investigate this coherent oscillation two identical bridges were made in Nb/Ta film 20μ apart (Fig. 3.1b). The bridges were 100μ wide to ensure a low resistance ($\sim$ 5 mΩ) so that 26 MHz oscillations would not be masked by internal Johnson noise. A separate thin film bias lead was fabricated between the bridges to allow independent biasing. A tank circuit was used to match bridge impedances with room temperature amplifiers (see Appendix B). As expected, the bridge oscillating voltage doubled when the bridges were biased so that they

Fig. 3.1

Placing two proximity effect bridges 20μ apart (b), it is possible by individual trim biasing to force the bridges to oscillate at either coincident or separate frequencies (a). The graphs in (a) have vertical axes proportional to the amplitude of 26 MHz voltage oscillation measured across the two bridges, and the horizontal axes show I_{bias}. In the first frame I_{trim} has been adjusted so that the average voltage across each bridge is equal, thus the bridges oscillate at the same frequencies. The half-width of the signal is constant whether the 26 MHz oscillations occur at the same I_{bias}. The size of the voltage oscillation indicates the phase agreement of the two bridges; this agreement is most probably induced by the weakly coupled LC tank circuit in which the bridge emissions are measured. The other frames of part (a) show the 26 MHz oscillating voltage with I_{trim} adjusted so that the average voltage across the bridges is not equal.

When two identical bridges are placed 2μ apart center-to-center as in (c), the measured oscillation output when current biased indicates phase and frequency coincidence with a common bias. If the identical bridges are farther apart than 2μ or obviously different, as in (d), then neither the frequencies nor the phases will be coincident.

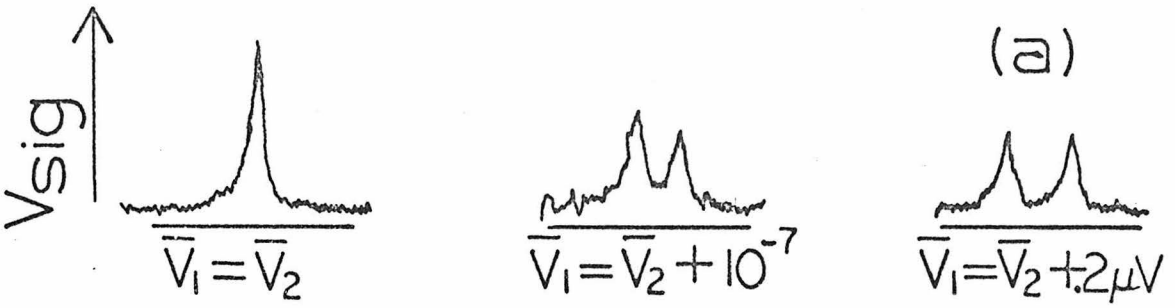
(a)
Vsig
$\bar{V}_1 = \bar{V}_2$
$\bar{V}_1 = \bar{V}_2 + 10^{-7}$
$\bar{V}_1 = \bar{V}_2 \pm 2\mu V$

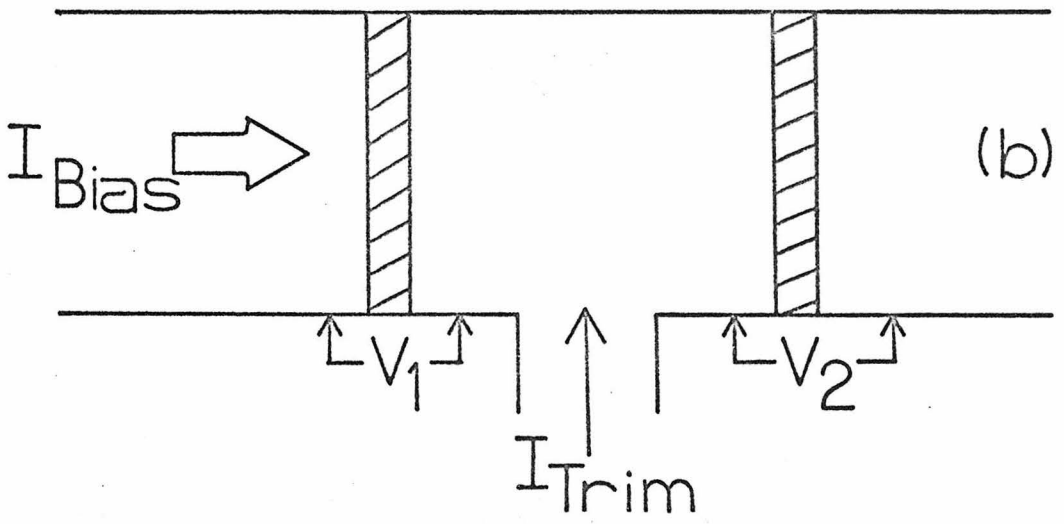
I_{Bias}
(b)
V_1
V_2
I_{Trim}

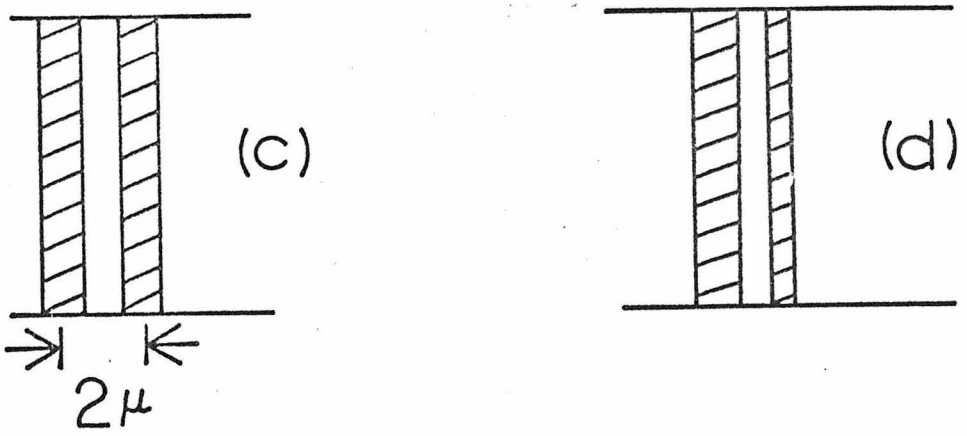
(c)
(d)
2μ

oscillated at identical frequencies (Fig. 3.1a). The signal width of the double bridge remained the same as the single bridge. Thus, there was no antipathy to coherent oscillation of series bridges when coupled weakly to a tank circuit. A test of two identical bridges 2μ apart with common current bias again resulted in a voltage signal twice the value that would be expected from one oscillating bridge. These tests were difficult to make quantitatively since it was hard to insert a small test signal without changing the impedance matching of the measuring system. Nonetheless accurate ratios of power output of a fixed bridge system at different temperature and bias could be achieved, as well as approximate ratios between different bridge systems. This difficulty stems from the nonlinearity of the system to voltage size, the small rf voltages being measured (10 nV), and the severe impedance mismatch between bridge and amplifiers.

The simple extension of this approach by making 10 bridges in series again confirmed the necessity of having close spacing to achieve cooperative behavior. In addition these studies made it obvious that fabrication procedures of increased scale and uniformity were needed. For example, slight differences between bridge resistances implies rf step widths will not be maximized at the same incident rf power since the n^{th} harmonic step size scales as $J_n(\frac{2eI_{rf}R_{bridge}}{h\nu})$. Also, slight differences in bridge length lead to different exponents β in the critical current temperature dependence $I_c \sim \exp(\beta\Delta T)$. Such critical current divergence makes coincident array operation impossible unless $\Delta T/T_c << 1$. As result, laser, SEM, and translational microscopic exposure techniques were developed to make hundreds of closely spaced

uniform bridges (see Appendix A).

3.2 Large Scale Arrays of Proximity Effect Bridges

The most successful method used in large scale array fabrication was SEM exposure of a grid pattern on the photoresist cover film, and ion beam milling of the exposed underlying refractory films (Fig. 3.2). The uniformity in lateral dimensions under optical and SEM inspection was complete with the respective resolutions of .2 and .03 microns. Depth uniformity had to be inferred from transition temperature widths. The transition widths were 10-100 $m^{o}K$ for 200 bridge arrays. Such a transition width is not unusual for a single bridge, so great uniformity of etching depth was achieved ($\sim \pm 5\mathring{A}$).

By reducing the separation between series connected proximity effect bridges to less than a few microns the Josephson oscillations of the individual bridges tended to synchronize. This synchronism or coherence is characterized first by bias current coincidence at the rf steps of the different bridges and secondly by phase agreement between the individual bridge voltage oscillations. This effect has been evidenced by both increased coincidence of steps at small incident rf radiation powers and by the linear scaling with bridge number of the internal oscillating voltage of a current biased series array.

3.2.1 DC properties

Extensive survey tests have been conducted on series arrays with 10 to 500 bridges. Many properties of these arrays are simply additive results of single bridge properties. For example, our standard Nb/Ta

Fig. 3.2

Schematic illustration of a small scale array made in a Nb/Ta film on sapphire (not to scale). Each bridge is formed by removing the Nb and some Ta film along a line by ion etching through a photoresist mask. Along the etched line the local transition temperature of the remaining Ta film is lower than that of the untouched adjoining film. Typically, the Nb is 100Å thick, the Ta 200Å thick, the current length of the bridge is .5μ, and the separation distance measured from the center of one bridge to the center of the next is 1-10μ . Arrays of this type have been tested with from 10-1000 series bridges, from .1 to 50Ω .

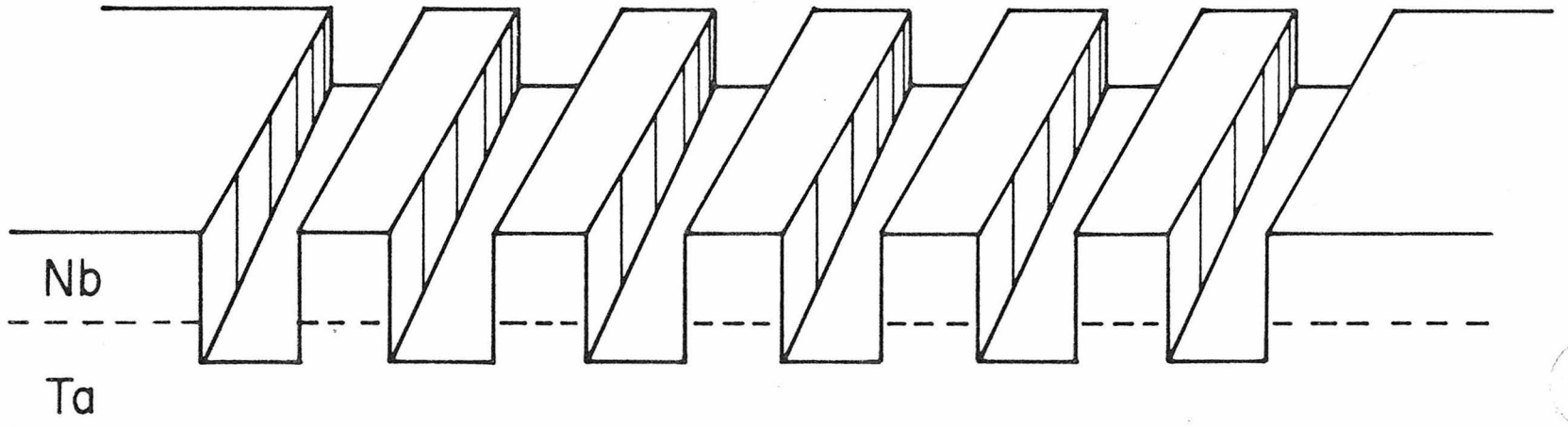
Nb
Ta

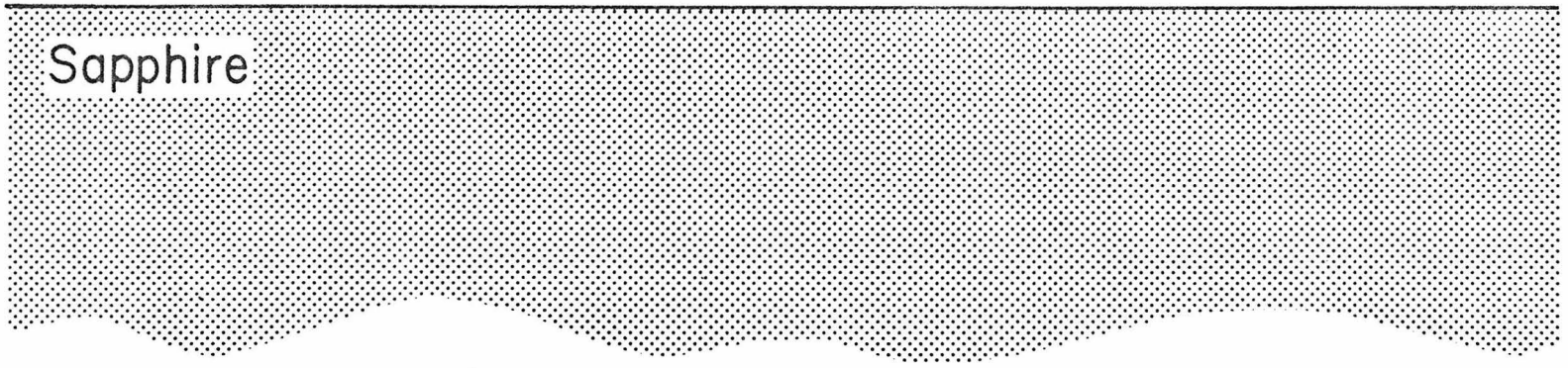
Sapphire

layered film has a resistance of 2Ω per square for the bridge areas. Thus, an array of 100 bridges each 100μ wide and .5μ long (length measured along the direction of current flow) is 1Ω. Arrays have been fabricated with resistances ranging from .1 to 50Ω. This great variability in array resistance with independent variability of the individual bridge resistance allowed the measurement criteria of good impedance matching to be decoupled from experimental goals such as seeing low frequency response or Joule heating behavior.

Critical current varies exponentially in temperature for arrays similar to single proximity effect bridges, $I_c = I_0 \exp(\beta T)$ to $I_0 \exp(\beta T^{1/2})$, (Fig. 3.3). The general behavior of the exponent ranges between linear and square root in temperature depending on the particular thin film used. This variation probably arises from the short mean free path in some thin films modifying the proximity effect and altering the expected $I_c \propto \exp(\beta T)$, dependence for these bridges.[2] Typically, β is between 10 and 20.

A perpendicular DC magnetic field modulates the critical current of a single bridge in a manner similar to the Josephson tunnel junction; that is, a single slit diffraction curve with a period in applied magnetic field of $\delta B = \phi_0/A$; where A is an empirical effective area. For proximity effect bridges the effective area is not simply the geometric area of the bridge, but is modified by some demagnetization factor which is proportional to the square of the width of the bridge. Hundreds of bridges in a closely packed series have a similar critical current modulation (where A is still the effective area of a single bridge) except that higher lobes of the curve are somewhat suppressed

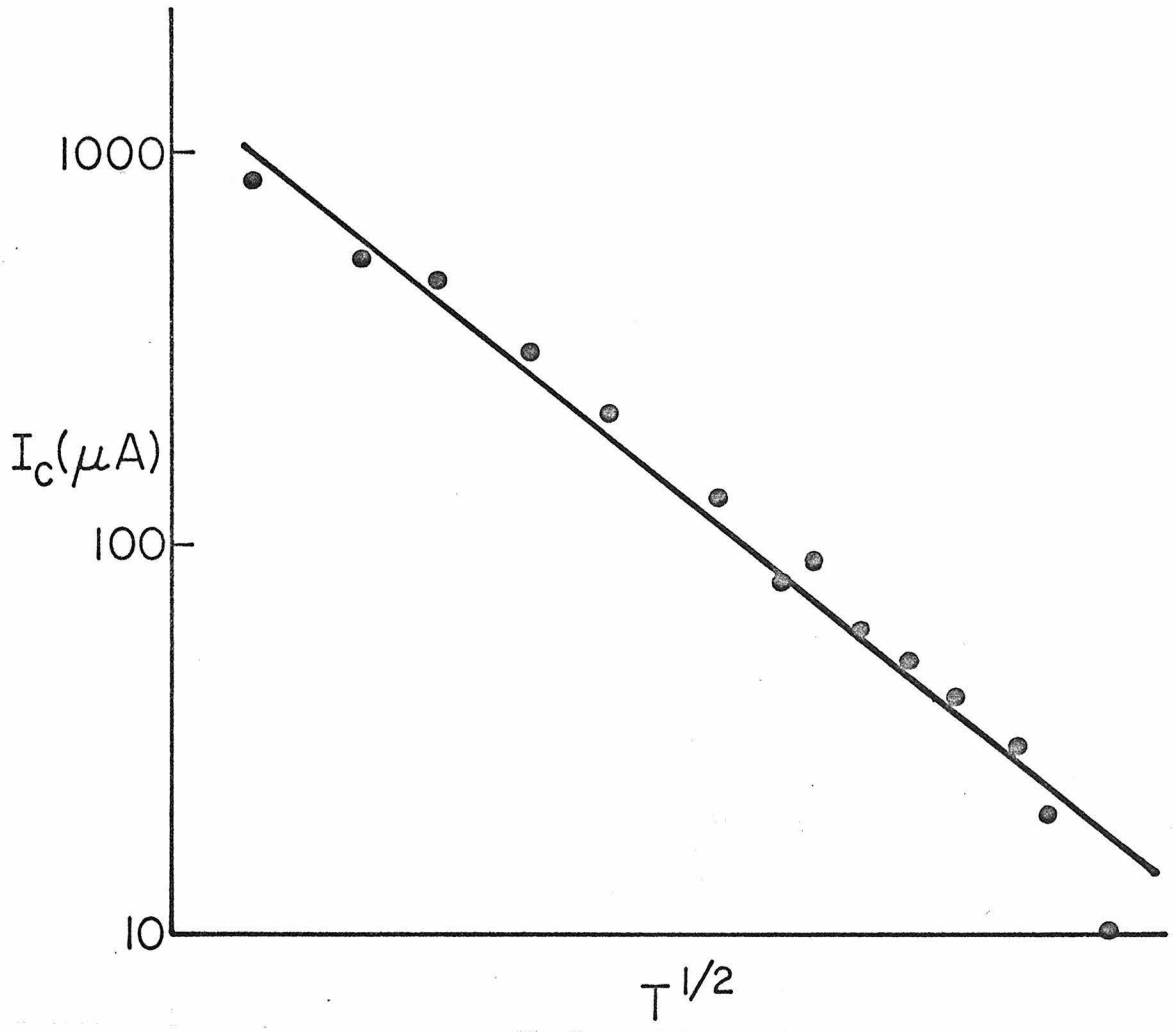

Fig. 3.3 The critical current of a bridge array has a high temperature exponential dependence very much like a single proximity effect bridge. Here a few decades of critical current are plotted as a function of $T^{1/2}$.

perhaps because of slightly different demagnetization from bridge to bridge (Fig. 3.4).

In addition to additive properties, arrays have cooperative interactions which lead to synchronous oscillation. Tests were made with 150 bridge arrays both in a 30 MHz resonant circuit and broad band from 10-500 MHz (Appendix B). In both cases the rf power scales as the number of series bridges. It must be emphasized that the maximum extractable signal from the coherent array grows linearly as the number of bridges, n , since both the oscillating internal voltage and the internal resistance are linear in bridge number. Another perspective considers instead a non-optimized but constant output load, which can lead to an output power growing as n^2 . This perspective is often called "superradiant" and implies that the fraction of energy that leaks into the radiation field is independent of the source resistance.

The frequency width of the rf power emitted has a lower bound determined by the Johnson noise and the effective bandwidth of a single bridge[3]. However, if operated far below the transition temperature ($I_c \geq 200$ μA), the frequency width of emission exceeds the intrinsic Johnson noise broadening since the individual differences in bridges have broadened the I-V characteristics.

A frequency tunable cryogenic VHF generator has been made by simply terminating a 50Ω cable with a 10Ω array of 150 bridges. Varying the current bias through this array changes the time average voltage across each bridge, hence their frequency of oscillation. Powers of 10^{-12} - 10^{-10}W have been produced from 30-500 MHz; maximum powers detected agree with coherent oscillation calculations. For example, at 300 MHZ the power $\sim nV_J^2/2R \sim 10^{-10}$W for this array. This approximation

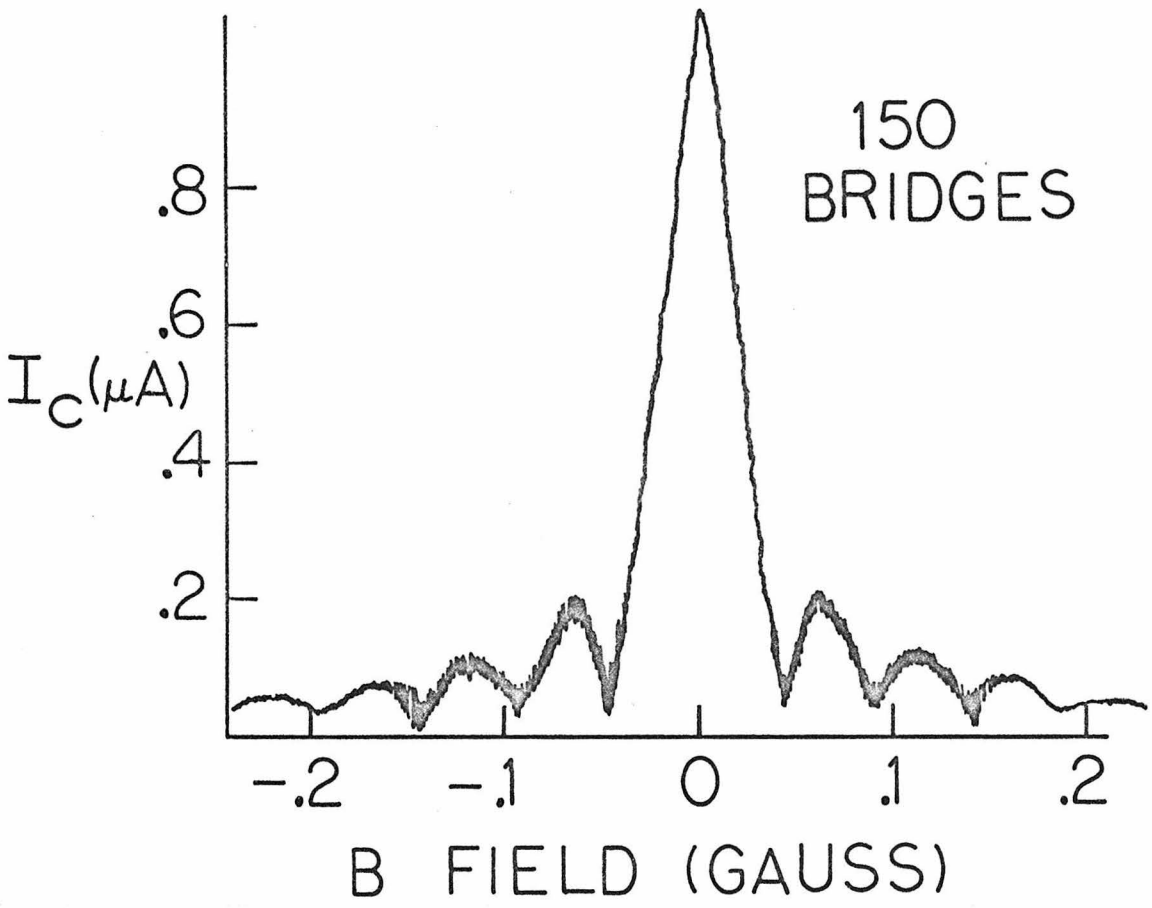

Fig. 3.4 As with single proximity effect bridges, external magnetic field can periodically modulate the critical current in a diffraction-like pattern. The period of the pattern is given by $(\Delta B)A = \phi_0$, where ΔB is the magnetic field intensity change between zero I_c levels, A is the effective area of a single bridge, and ϕ_0 is the fundamental flux quanta.

Fig. 3.5

The measured rf emission of a current biased series array. This array has 300 bridges with 1μ spacing center to center. The plots are at fixed temperature looking for (a) 100 MHz, (b) 300 MHz, and (c) 500 MHz. The half-width of the emission signals (∿ 50 MHz) is slightly more than that expected due solely to internal bridge resistance at this critical current. Definite subharmonic and harmonic structure exist on all traces. The negative signal at the 500 MHz half-step is not explained.

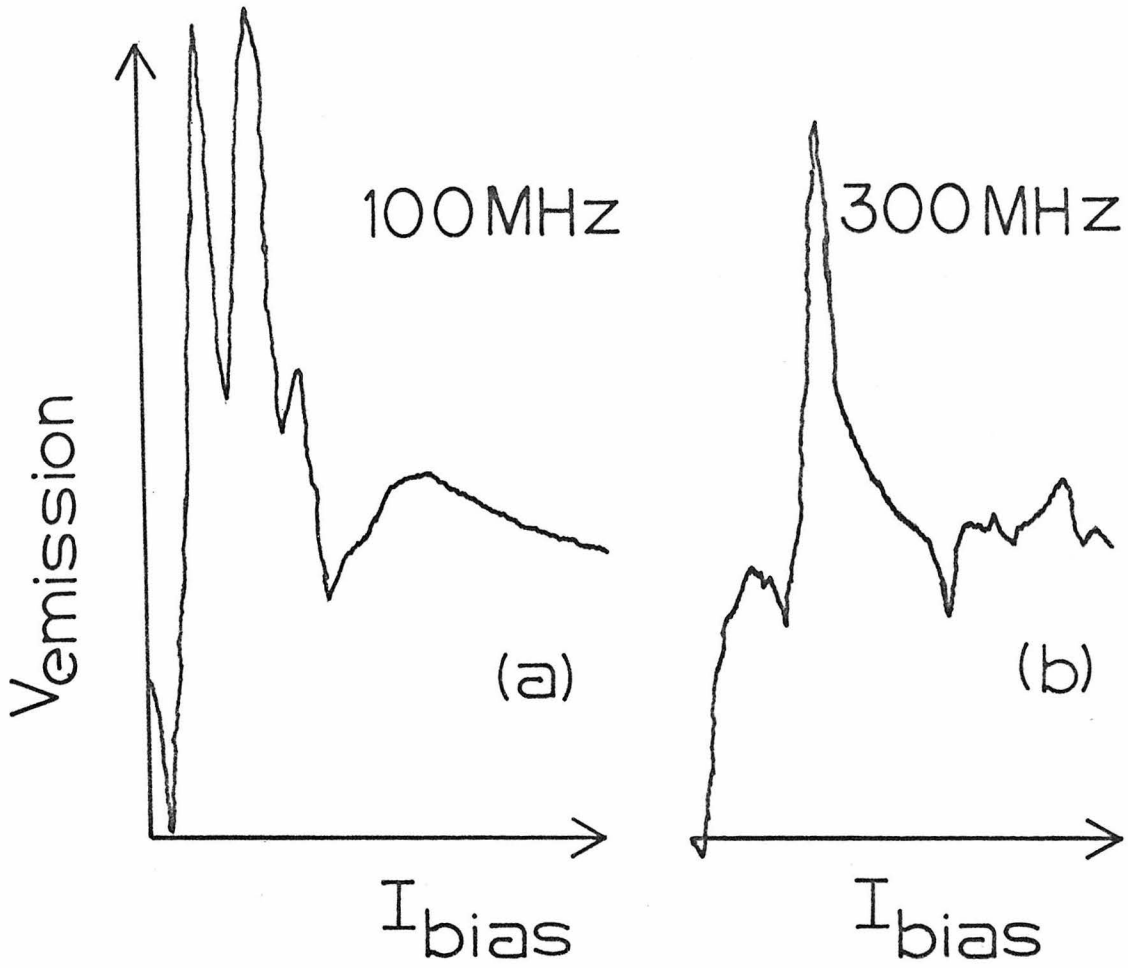
100MHz
300MHz
Vemission
(a)
(b)
Ibias
Ibias

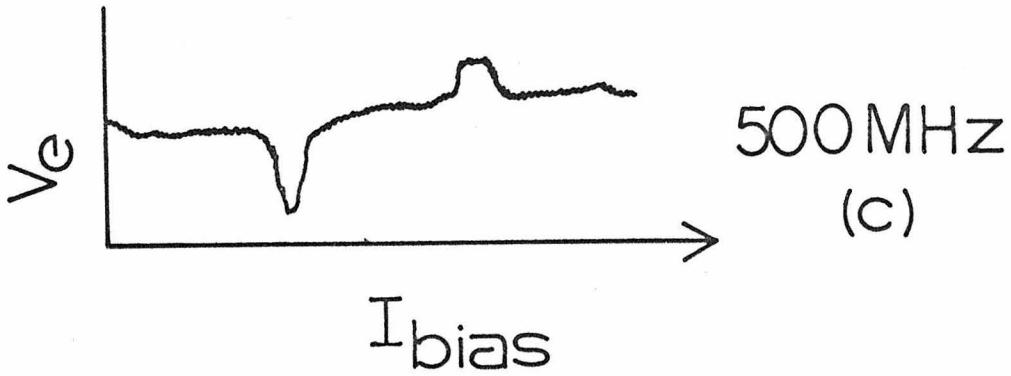
Ve
500MHz
(c)
Ibias

implies that the internal oscillation is over the complete Josephson voltage, a condition that holds if $I_c R_{bridge} \sim V_J$. In the limit of smaller values of I_c we expect a power of $I_c \phi_o \nu$, or $I_c V_J$.[3] These emission tests on arrays showed considerably more subharmonic and harmonic signals than comparable single bridge tests (Fig. 3.5).

3.2.2 Radiation induced characteristics

Typical current-voltage (I-V) and dynamic resistance-current (dV/dI - I) curves for these arrays are shown in figure 3.6. The lower half of the figure shows an I-V curve for a 154 bridge array (bridge length .7μ , separation 2μ) with and without external radiation at 420 MHz. In this example the radiation power was chosen to induce the maximum number of "steps". The upper half of the figure shows the step structure in more detail with dV/dI-I . These gross features can be represented by saying that the array is responding to the radiation field as though it were quantized in units of nh/2e , where in this case n = 154 .

Complete first rf steps (dV/dI = 0) have been achieved from 10 MHz to 2 GHz. In this case the rf power was chosen to enhance a particular harmonic step which also results in diminishing the size of the rest of the steps. In the bias current range of the step the differential resistance remains zero for a current width of at least 10% of the critical current at that temperature. This extreme coincidental behavior of the bridges in the array is a sign of the uniformity of fabrication. RF steps occur at the bridge number multiple of the Josephson voltage to within experimental accuracy. This means a measurement of 5% has been made, not 1 part in 10^8, as has been done in

Fig. 3.6

Typical voltage and differential resistance plots for arrays. This particular array has 154 bridges, L = .5μ and center-to-center spacing of 2μ . The lower curve shows I-V characteristics with and without rf radiation. The well-defined constant resistance region after a slow initial voltage rise can be seen. To enhance the details of the rf induced changes in the I-V characteristics a differential resistance trace is shown in the upper part of the figure. The rf power has been adjusted to see a maximum number of steps, not to maximize any particular one. Several half-steps can be seen.

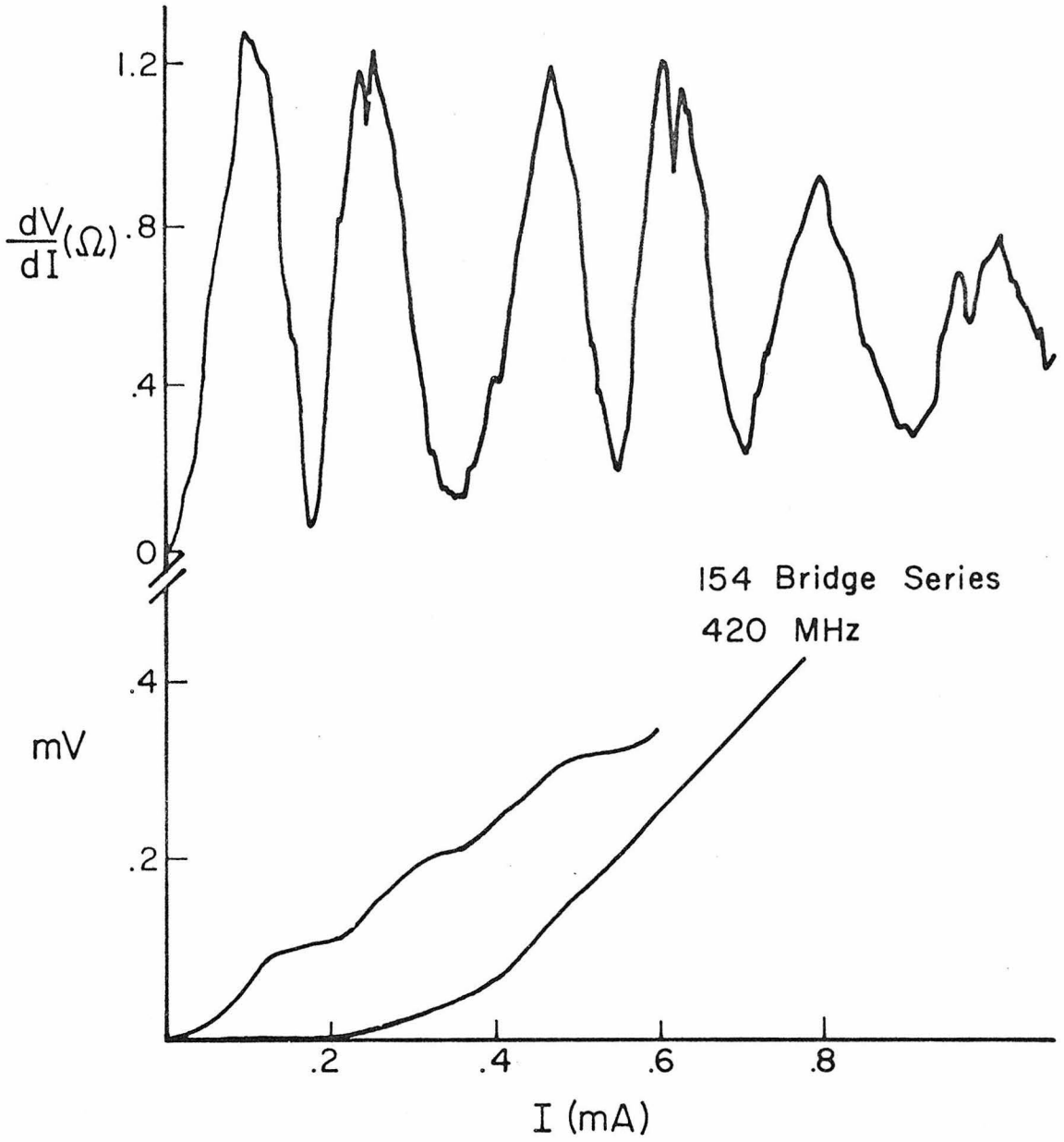
1.2
.8
.4
0
dV/dI (Ω)
154 Bridge Series
420 MHz
.4
.2
mV
.2
.4
.6
.8
I (mA)

the case of a single Josephson junction that has been used to find the ratio e/h and define the national volt.[4]

The zero voltage supercurrent of the array is periodic in rf power in the same manner as a single bridge (Fig. 3.7).

$$I_c = I_o J_o(2eV_{rf}/h\nu)$$

In this particular characteristic, the arrays are more pronounced than the single bridges. A typical single bridge would show periodicity through only one or two oscillations. This ability to modify I_c with external radiation is often convenient when attempting to synchronize arrays in which the elements are not identical. The oscillation frequency of a particular current biased bridge (b) is determined by the average voltage across it--or in a phase slip model (section 2.2).

$$\overline{V}_b = R_b\overline{I}_n = R_b(I_{bias} - \overline{I}_s)$$

Thus at constant bias, the voltage is composed of two parts: one linear in R_b and the other proportional to a product of R_b and I_s. Usually the bridge resistances are quite similar due to the homogeneity of the films and the fabrication process, however, critical current ($I_c = 2\overline{I}_s$) can be somewhat more divergent well below the transition temperature ($T_c - T \geq .2^oK$). However, by radiating the array with the proper amplitude and frequency of external radiation, the critical current can be made zero. In this way, the critical current is artificially made zero and the array can then oscillate synchronously at frequencies below the applied radiation if the junction resistances are sufficiently identical. In particular, a 2 GHz external signal was

Fig. 3.7

The critical current of an array can be periodically modulated by rf voltage, since $I_c = I_o J_o(2eV_{rf}/h\nu)$ for each bridge. This modulation is experimentally more pronounced with an array than with a single bridge.

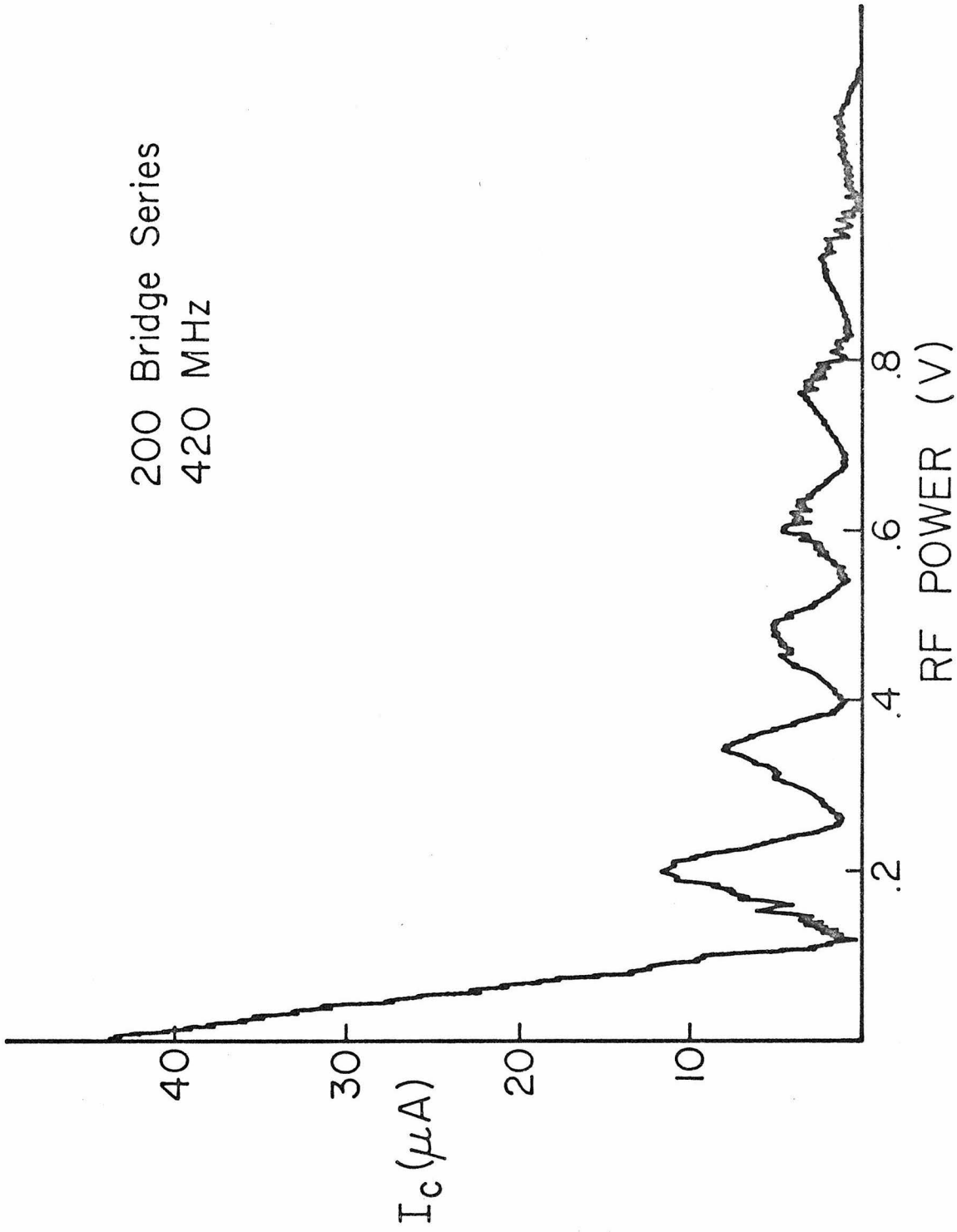
200 Bridge Series
420 MHz
40
30
20
10
I_c (μA)
.2
.4
.6
.8
RF POWER (V)

used to synchronize lower frequency (10-500 MHz) internal oscillation in a 200 bridge array, which was operating below the temperature range where internal synchronization occurred spontaneously.

One measure of the strength of interbridge coupling was the highest frequency (voltage) at which the series arrays showed a complete ($dV/dI = 0$) induced step. Ten bridge arrays each containing 100 bridges ($L = .5\mu$) were constructed with different center-to-center bridge spacing, from $1\mu - 10\mu$. The highest voltage interference step achievable on an array depended strongly on the bridge spacing with the closest spacing reaching 5 GHz (Fig. 3.8a). In a similar manner the amplitude of the oscillating voltage across the array when current biased also increased with decreasing spacing becoming completely coherent with spacing of about 2μ (Fig. 3.8b).

3.3 Interbridge Coupling in Series Arrays

A number of phenomena occur as the interbridge spacing in series arrays is decreased toward 1μ. First, induced rf steps become coincident even at small rf power levels. Second, array rf emission signal size indicates the internal bridge voltages are oscillating coherently when current biased. Third, rf response shows an accentuation of the subharmonics of even denominators 1/2, 1/4, 1/6. Fourth, emission experiments indicate more subharmonic oscillations in arrays than in single bridges.

These phenomena can be described by either of two processes of intrafilm coupling. The first process to be discussed will be direct coupling through the superconducting film which separates neighboring bridges. The second process considered assumes quantum interference

Fig. 3.8

The arrays show distinct changes in properties as a function of interbridge spacing. One measure of interbridge cooperation is the highest frequency at which all bridges still have coincident steps; that is, the highest frequency at which a complete ($dV/dI = 0$) step can occur for the array. In graph (a) the highest frequency step is at 4 GHz with 1μ bridge spacing; a fast fall-off in cooperation exists between 2-5μ spacing. Another measure of interbridge cooperation is the size of the array voltage oscillation when current biased. Each bridge undergoes voltage oscillation when biased above I_c, the resulting total array oscillation increases with decreasing spacing until a maximum is reached between 1-2μ (b). The amplitude of the oscillating voltage indicates complete phase coherence has been reached with 1μ spacing over 30-500 MHz.

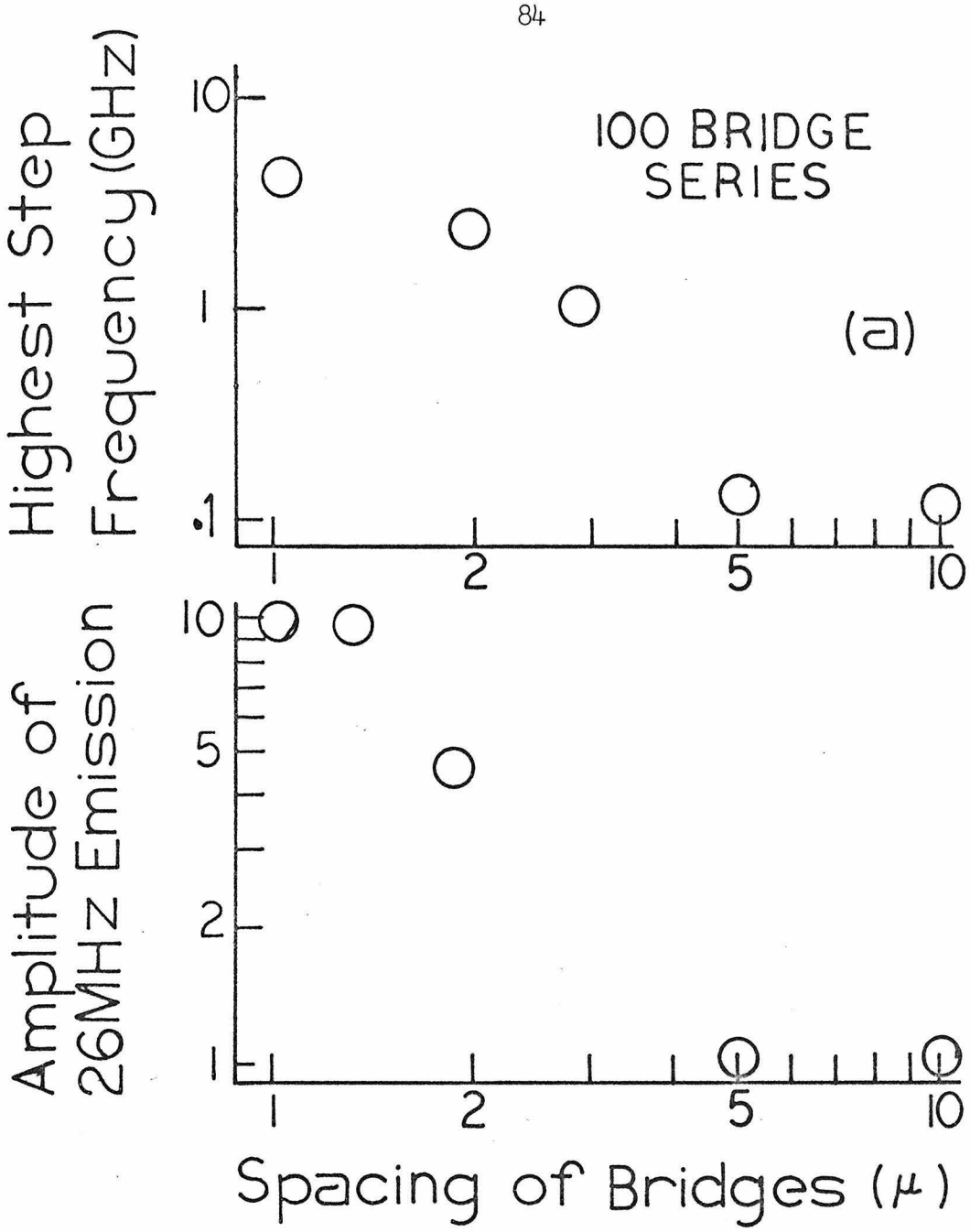
Highest Step Frequency (GHz)
10
1
.1
100 BRIDGE SERIES
(a)
1
2
5
10
Amplitude of 26MHz Emission
10
5
2
1
1
2
5
10
Spacing of Bridges (μ)

not only between successive strong superconducting wave functions but also between next nearest wave functions.

The strong interbridge coupling is likely to be at least as complex as the single proximity effect bridge interference, thus the explanations presented here make an attempt to explain the simpler general relationships by the use of equivalent circuits rather than speculating on complexities that cannot be experimentally measured with present technology.

3.3.1 Direct bridge coupling

The explanation for the high frequency response in Chapter II suggested that the voltage seen by the superelectrons across the Josephson-like oscillator is not identical to the voltage drop seen by the normal electron flow (see section 2.5). This explanation involved an equivalent circuit (Fig. 2.9b) which had a time constant $\tau \sim 10^{-11}$sec consistent both with high frequency dependence on responsivity, and calculated values of bridge kinetic inductance and measured resistance. As seen in figure 2.9b the voltage appearing across the Josephson-like current source, V_J , is not the same as that seen by the normal electron flow in R_b, V_n . That is, the voltage used in the instantaneously true frequency-voltage relationship, $h\nu = 2eV_J$, is not necessarily the voltage seen by the normal electrons since there is nonequilibrium characterized by a relaxation time $\tau = L/R_b$. In fact it is possible to define the superelectron pair potential, μ_p , by using the observable frequency of oscillation, that is, $\mu_p(x_1) - \mu_p(x_2) = \dot{\theta}_1(x_1) - \dot{\theta}(x_2)$, and thus across the

quantum oscillator $\delta\mu_p \propto \nu$. In the same spirit the normal potential μ_n can be related to the normal current, $\nabla\mu_n \propto j_n$. The nonequilibrium state of this complex current flow allows the superconducting and normal electrons to have different potentials at the same spatial point. Previous work[5] has shown that this chemical potential difference is still measurable one micron beyond the S/W interface, well into the strong superconductor. With this perspective it was decided to place two bridges in series separated by only a one micron length of strong superconductor. Then it would be possible to support completely nonequilibrium electron flow through both the bridges and the separating film thereby coupling the instantaneous nonequilibrium state of one bridge to the next. That this did occur represented a new phenomenon never before seen or described.

Using the single bridge circuit representation of figure 2.9b, the nonequilibrium condition of two bridges placed in series close together can be represented by the circuit in figure 3.9. The inductance between A and B represents the possibility of potential imbalance ($\mu_p \neq \mu_n$) between superelectrons and normal electrons in the connecting strong superconductor. This equivalent circuit suggests that if the strong film connection were several microns long and therefore the electron flow had time to return to equilibrium, the inductance value L' should be zero. If the strong film connecting the bridges is only tenths of microns, the inductance L' approaches the maximum value of the bridge kinetic inductance, a measure of how far out of equilibrium the flow can become.

Fig. 3.9

An equivalent circuit for two bridges in series can be assembled from the equivalent circuit of one bridge given in Fig. 2.9b. Again the current sources marked with an "X" obey a Josephson-like relation,

$$I = I_o \left[1 + \cos \frac{2e}{h} \int_0^t V(t')\, dt'\right]$$

This circuit produces coupling between the oscillators because of the existence of the inductor L'. L' represents the non-equilibrium condition that exists between the normal electron flow through R_{b1} and R_{b2}, and the superflow through the left-hand current path. Again, appropriate values are $R_{b1} = R_{b2} = R_{c1} = R_{c2} \sim 2R_{bridge}$. As the spacing which separates the bridges is lessened, L' experimentally approaches $\sim 10^{-11}$H.

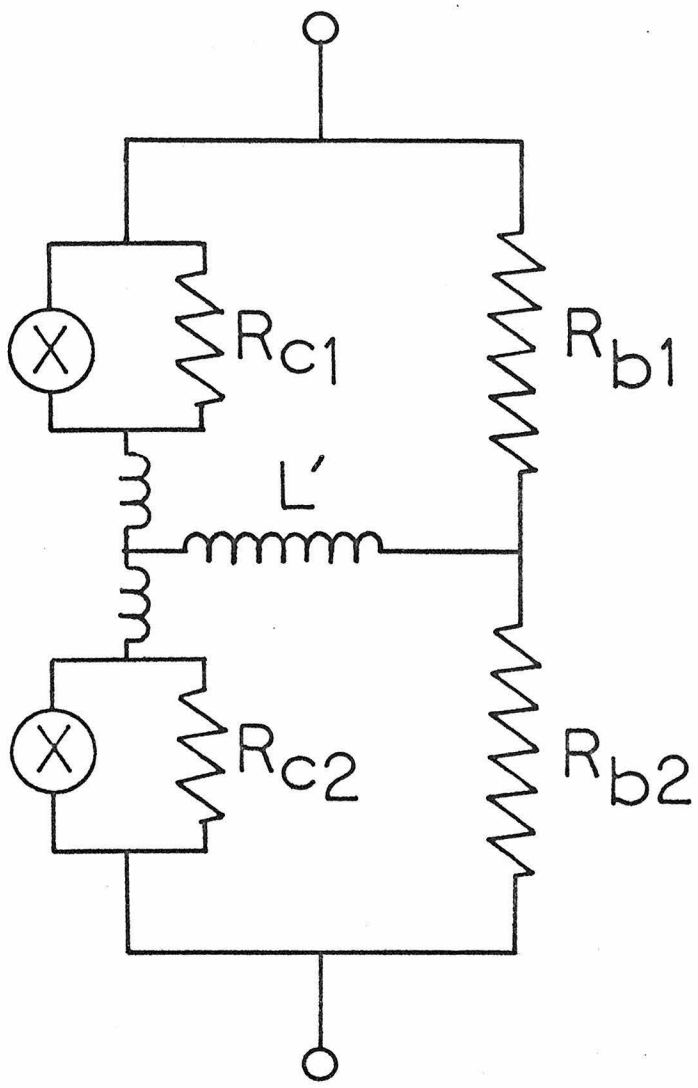
R_{c1}
R_{b1}
L'
R_{c2}
R_{b2}

This circuit obviously couples the two Josephson oscillators, and because of their nonlinearity this coupling can lead to frequency and phase alignment. Remembering that R_c and R_b are about $2R_B$, and L_b is estimated to be 10^{-11} - 10^{-12}H, this circuit with a 100-2000 MHz oscillation can be analyzed using the approximations $R_c \sim R_b$ and $\omega L_b << R_b$. Consequently, a Josephson oscillation voltage of amplitude V_2 across R_{c2} induces a coupling voltage V_1 across R_{c1} where

$$V_1/V_2 \simeq \omega L'/4 R_B \qquad (3\text{-}1)$$

For closely placed bridges the assumption that $L' \sim L_b$ results in $V_1/V_2 \sim 10^{-2}$ (letting ν = 1 GHz, $R_c/R_b \simeq 1$, $R_B \simeq .1\Omega$). Thus only a small percentage of the voltage is available for coupling. How much external rf voltage is required across a quantum oscillator to synchronize the frequency and phase is not known. Experiments using standard rf signal generators have shown that as little as 10^{-9} is needed for synchronization of a bridge (at 1 GHz), but the minimum determined by these experiments was set by the monitor instrument limitations and not by any intrinsic physics in the quantum interference. A coupling voltage of 10^{-9}V could arise from a neighboring bridge having a 10^{-7}V rf oscillation, the product of I_c = 10 μA and R_c = 10 mΩ. These values for I_c, R_c, and frequency are the correct orders of magnitude at which interbridge coupling was experimentally observed.

As the length of the superconducting connection between bridges is decreased the measure of nonequilibrium of the normal and superelectrons in the connection should increase. Thus in the equivalent

circuit model of figure 3.9, L' should be increased to represent the larger possible potential imbalance between pairs and normal electrons. If L' increases the voltage coupling given by equation (3-1) becomes larger. Therefore at any given frequency the coupling improves with closer bridge spacing. In agreement with these physical arguments the coupling, as measured by the highest frequency at which a completely coincident first step could be induced in a 100 bridge array, improved with decreased bridge spacing (Fig. 3.8).

A particular nonequilibrium mechanism that would increase greatly with bridge proximity is electron heating. Appendix C gives thermal arguments showing conclusively that for these circuits the lattice is pegged firmly to the sapphire substrate; the temperature decay length in the film is $\sim .5\mu$. Furthermore, the current levels at which the array coupling effects take place would raise the bridge temperature less than $.01^{o}K$. Thus lattice temperature rise does not seem directly involved in interbridge coupling. On the other hand, the normal electrons may be thermalized and remain out of equilibrium for τ_{TH} ($\sim 10^{-10}$sec). During this time interval the normal electrons would diffuse about 1μ (assuming $v_f = 10^6$m/sec, $\ell = 100\mathring{A}$). Thus an increase in normal thermalized electrons in one bridge can quickly affect the neighboring bridges if closely packed. Such nonequilibrium may be one element of the more general nonequilibrium direct coupling.

3.3.2 Next nearest wave function coupling

Besides direct coupling, a subtler coupling may exist. This coupling is between every other macroscopic wave function. Empirically,

two strong wave functions show quantum mechanical interference effects when separated by up to 2μ of weakly superconducting film. When instead, two wave functions are separated by a sequence of .5μ weak, .5μ strong, and .5μ weak superconducting film as in an array, there may still be interference effects between these two wave functions. If two wave functions can overlap and interfere within a third wave function on at least a 10^{-10}sec time scale, this would be another indication that a .5 micron extent of the strong superconducting film is not enough to let the electrons come to full equilibrium and define a single phase state. Of course, the interference effects between neighboring strong macroscopic wave functions are also assumed to exist. Two tests of this proposed coupling substantiate the concept.

One immediate test of an assumed next nearest neighbor interference is an increase in induced subharmonic steps in an array as compared to single bridges. This increase is experimentally observed as the bridge spacing is decreased. This emphasis on subharmonic features can be reasoned as follows. When the array is current biased so that every bridge experiences a time average voltage, $\overline{V}$, the voltage between next nearest wave functions is $2\overline{V}$. Thus, whatever the frequency of Josephson-like currents between neighboring strong superconductors, currents of twice that frequency exist between next nearest strong regions. One result of this frequency doubling is enhanced half-step response to incident rf. Remember, a subharmonic step of a single bridge can be considered as evidence of higher harmonic components of the Josephson oscillation interacting with incident radiation. Since the normal current oscillation is not sinusoidal in a proximity effect

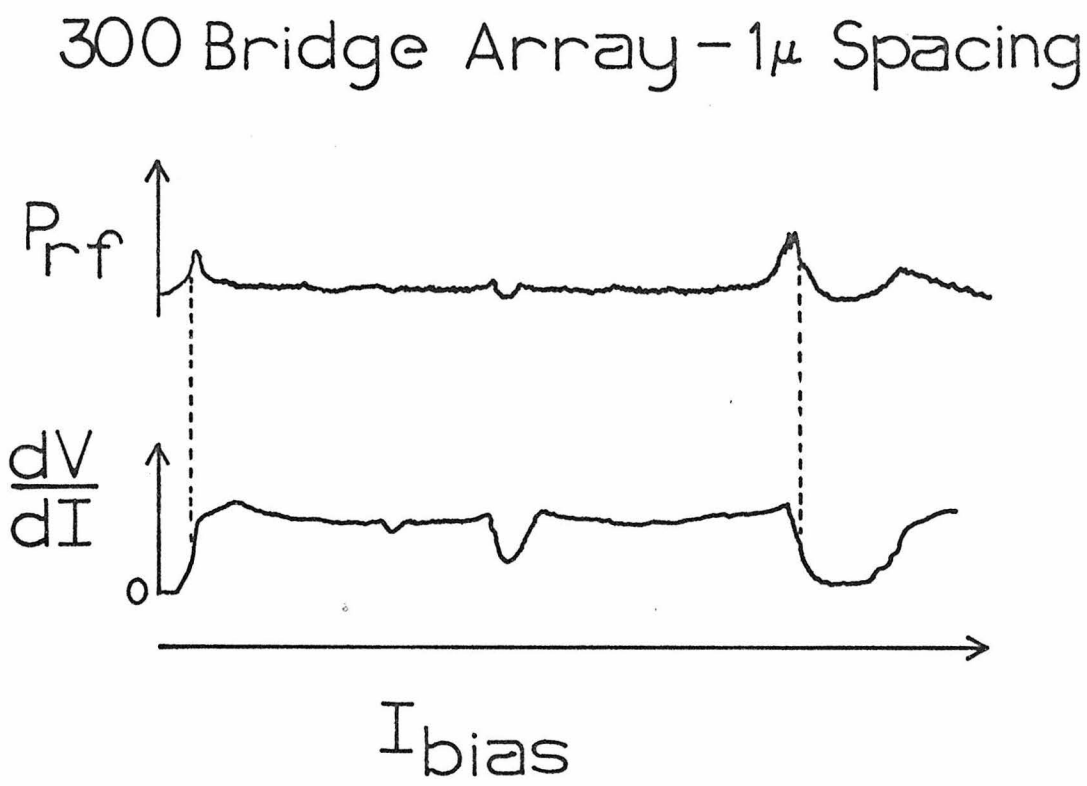

Fig. 3.10 Closely packed series bridges exhibit emphasis on even subharmonics (1/2, 1/4, 1/6). This 300 bridge array of 1μ center to center L = .5μ bridges exhibits (lower graph from left to right) 1/6, 1/4, 1/2 steps of 2 GHz radiation. With no 2 GHz present the critical current was large (> 300 A), and the bridges showed little cooperative 30 MHz internal oscillation when current biased. This was due to their slight differences in R and β being magnified to large voltage differences at this large critical current. However, the upper trace shows the 30 MHz emission with the 2 GHz radiation present, thus the strong 2 GHz signal has forced synchronization of the bridges. The steepest derivatives in the lower curve mark the edge of the 2 GHz rf steps for most bridges in the array. The 30 MHz emission signals are shifted from these currents by (ΔI_{bias}) such that $(\Delta I_{bias})(R_{bridge}) = V_{J\ -\ 30\ MHz}$.

bridge some subharmonic structure on the I-V characteristics is expected. A single bridge typically shows partial 1/2 and 1/3 steps. However, when many bridges are placed in close succession there exists an accentuation of 1/2, 1/4, and 1/6 steps; the 1/3 step is not present (Fig. 3.10). The 1/2 step of single bridges is the fundamental step of the next nearest wave functions. The 1/4 step of single bridges is the 1/2 step of next nearest neighbors. However, the 1/3 step of a single bridge has no corresponding common oscillation of the next nearest configuration, but only in every third wave function; thus the squelching of the 1/3 step in an array as was experimentally observed. Perhaps if fabrication would permit more wave functions within a 2μ space, higher order interference could be encouraged.

A second test of the next nearest neighbor coupling involved testing an analog of this coupling. As in near neighbor interactions, next nearest wave function interactions must also encourage coordination of internal voltage oscillations of bridges. This is most easily seen by considering the equivalent circuit for next nearest wave function interaction shown in figure 3.11. First a digression: consider why one bridge has phase slip by 2π all along its width instantaneously on the scale of 100 MHz. The phase slip model requires that the weakest central coherence length of the bridge periodically has its pair density driven to zero with a consequent phase slip of 2π. That this will happen simultaneously along the entire current width of the bridge can be reasoned by considering the extra load that this local stoppage of supercurrent puts on the neighboring current paths. If

Fig. 3.11

(a) Schematic illustration of 3-bridge array. The weak bridge regions are marked W , the strong regions S . With single bridge logic, wave functions S_A and S_B can interfere, as can S_B and S_C . The corresponding voltages of such interactions are V_{AB} and V_{BC} . However, during this investigation it was discovered that if the distance between S_A and S_C was less than 2μ , then the resulting characteristics could be explained as if an interference also occurred between S_A and S_C at voltage V_{AC} .

(b) This idea was tested by the construction of a single junction of resistance R in parallel with two in series, each of resistance R/2 . This geometry produced enhanced subharmonic behavior and synchronization of the phase slips. An equivalent circuit for this interaction is given in (c).

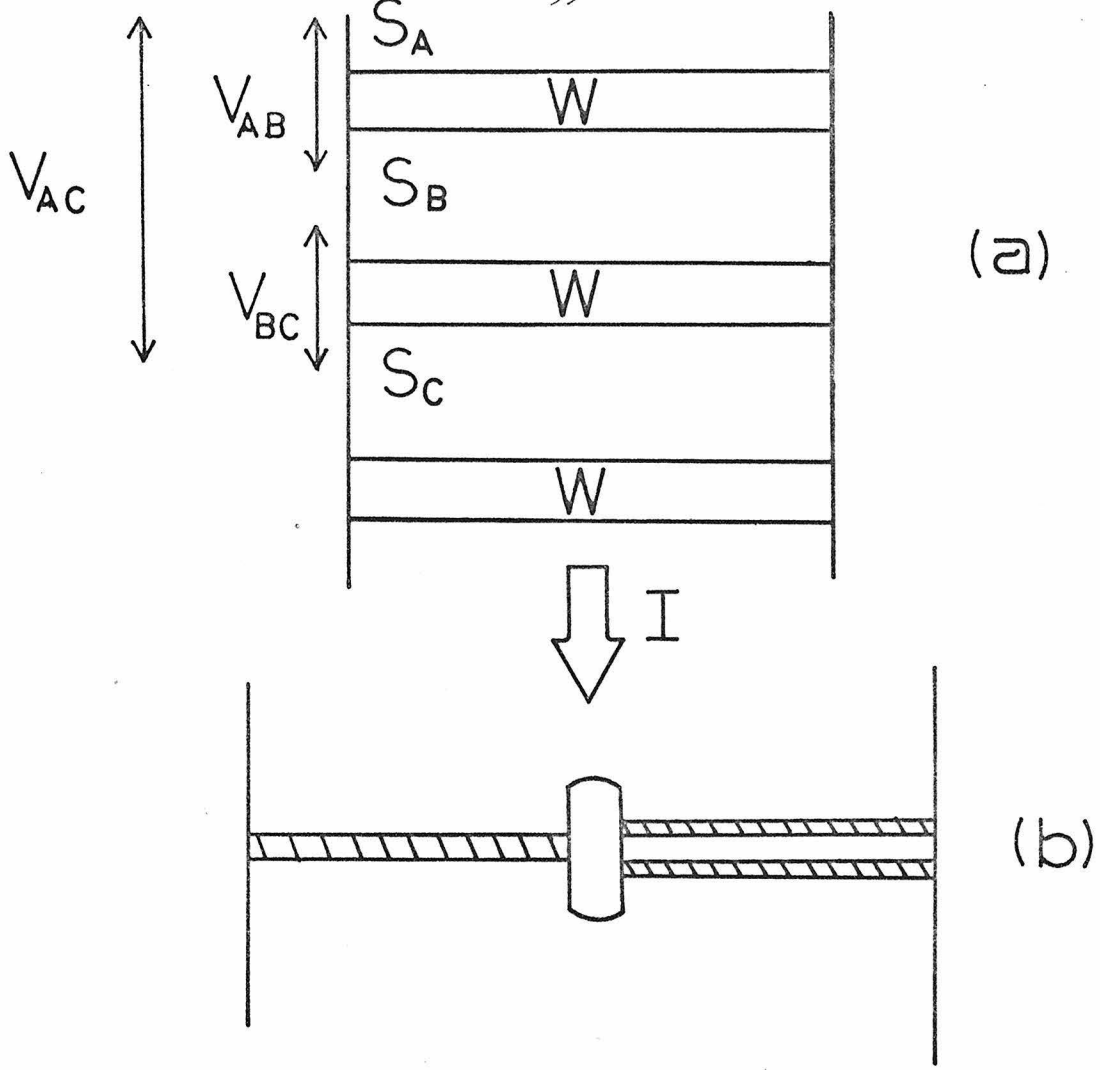

(a)

(b)

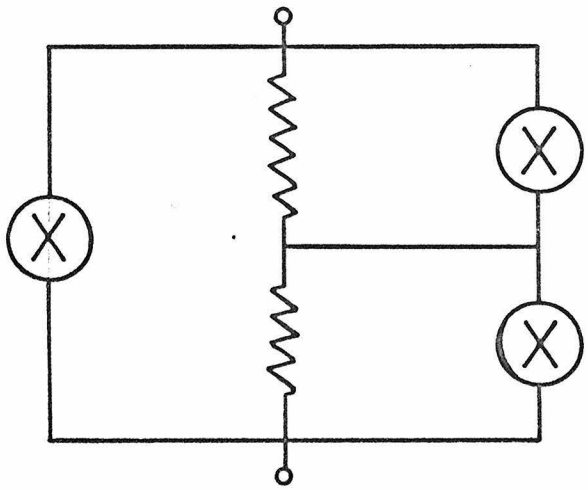

(c)

alternate paths try to short out the temporarily normalized path, this extra supercurrent load will precipitate their breakdown.

This physical argument for coincident phase slip along the whole width of a proximity effect bridge was experimentally confirmed in previous research.[3] The experimental evidence of uniform phase slip was an rf voltage detected across the bridge when the bridge was current biased. In fact applying a magnetic field to the bridge will force opposite ends of the bridge to oscillate out of phase thus modulating the amplitude of rf emission.

Now consider what will happen if two bridges are placed in parallel. Again, one would expect the phase slippage to occur simultaneously provided there is no magnetic field. In this research, the same rf voltage was measured with fixed current bias whether one single bridge was tested intact or divided into two parallel bridges.

The final step to produce the equivalent model of next nearest neighbor interaction was to replace one of the identical parallel bridges with two in series of the same total resistance (see Fig. 3.11b). The rf emission signal was approximately that of a single bridge of equivalent resistance and critical current, a result consistent with coincident phase slip. The induced subharmonic features of such a circuit were more pronounced than for a single bridge, again in agreement with results of the bridge array I-V characteristics. Thus by constructing an analog of the next nearest wave function interaction, it has been shown that such interaction encourages synchronism in the internal voltage oscillations of series bridges and subharmonic

emphasis in their I-V characteristics. This newly suggested process appears experimentally consistent with closely spaced bridge series.

CHAPTER IV

TIME DEPENDENT BEHAVIOR AT AN S/N INTERFACE

The time dependence of voltage across a proximity effect bridge (S/W/S) has been studied in great detail and described by the macroscopic wave function phase slip process.[1] These studies were made to gain an understanding of the superconducting state in nonequilibrium caused by the presence of a potential gradient. The geometry of the planar proximity effect bridge was chosen in order to control systematically the geometric and material parameters of the voltage sustaining region. These investigations indicated the importance of the pair distribution at a superconducting-normal metal interface in the quantum interference of a bridge. This chapter reports on similar studies at a single S/N interface.

In equilibrium, the pair density distribution is both analytically and experimentally known at an S/N (superconductor-normal) interface (see Chapters I and II). However, by passing a current through this interface, a voltage can be developed across the boundary region of the macroscopic wave function. This might produce a nonequilibrium state with a unique time dependence, similar to that of the double S/N interface that forms a proximity effect bridge. The investigation reported here was an examination of these ideas and resulted in a determination of the superconducting pair distribution necessary to produce quantum interference at an S/N interface and it was also found that the frequency of this interference was related to the interface potential by a modified Josephson relation.

Two previous investigations had indicated possible quantum interference at a superconducting-normal metal interface. Both involved superconducting points pressed onto normal bulk metals.[2] The evidence for quantum interference was the appearance of voltage-step structure on the superconducting I-V characteristic upon application of microwave radiation, such as illustrated in figure 4.1b. Since the S/N interface resistance was in series with the bulk normal metal resistance, the voltage measured across these point contacts included not only the average of any time dependent interface voltage but also a term from the spreading resistance of the normal metal. Thus the measured voltage must be corrected for this series resistance. In the initial investigation this corrected voltage, used in the Josephson voltage-frequency relation, yielded

$$2eV/h\nu = f$$

where f could be varied from zero to one as a function of interface resistance. However, subsequent investigation found f to be discrete and equal to 1/2, 1/3, 1/4. No theoretical explanation has yet been suggested for these effects.

With this background of experiments in mind and the well developed planar proximity effect work in hand, it was decided to investigate both planar submicron "point contacts" between superconducting and normal regions and also 20μ wide, uniform current density, thin film S/N interfaces for evidence of quantum interference (Figs. 4.2, 4.3). The objective of these experiments was to find the following: the important interface parameters which allow quantum interference, the localized region where the interference takes place, the voltage-

Fig. 4.1

(a) Schematic illustration of superconducting point contact with bulk normal metal used in two previous investigations of the S/N interfaces. The experimental equivalent circuit for this interface is shown with the usual current source shunted by the interface resistance R_I, and the bulk normal metal resistance R_S in series with the active interface.

(b) A typical I-V characteristic is given in (b). The lower curve shows the characteristic without rf radiation. At low currents the slope equals R_S and the interface is time independent. At the elbow a "critical current" has been reached and the interface now sustains a time dependent voltage. This time dependence was confirmed by the induction of voltage steps in the I-V curve by microwave radiation (upper curve). The step spacing ΔV was often less than that predicted by the Josephson relation, $\Delta V < h\nu/2e$.

(c) As the temperature of an ordinary proximity effect bridge is lowered through the superconducting transition, the bridge shows a continuous drop in resistance. At any temperature within the transition the extent to which rf radiation can modulate the slope of the I-V characteristics at the Josephson voltages is equal to the bridge resistance reduction already achieved. This partial modulation can be interpreted as resulting from a partial induced superconductivity of the bridge region near the interfaces. Thus in this transition temperature range the bridge can be considered somewhat like two W/N interfaces.

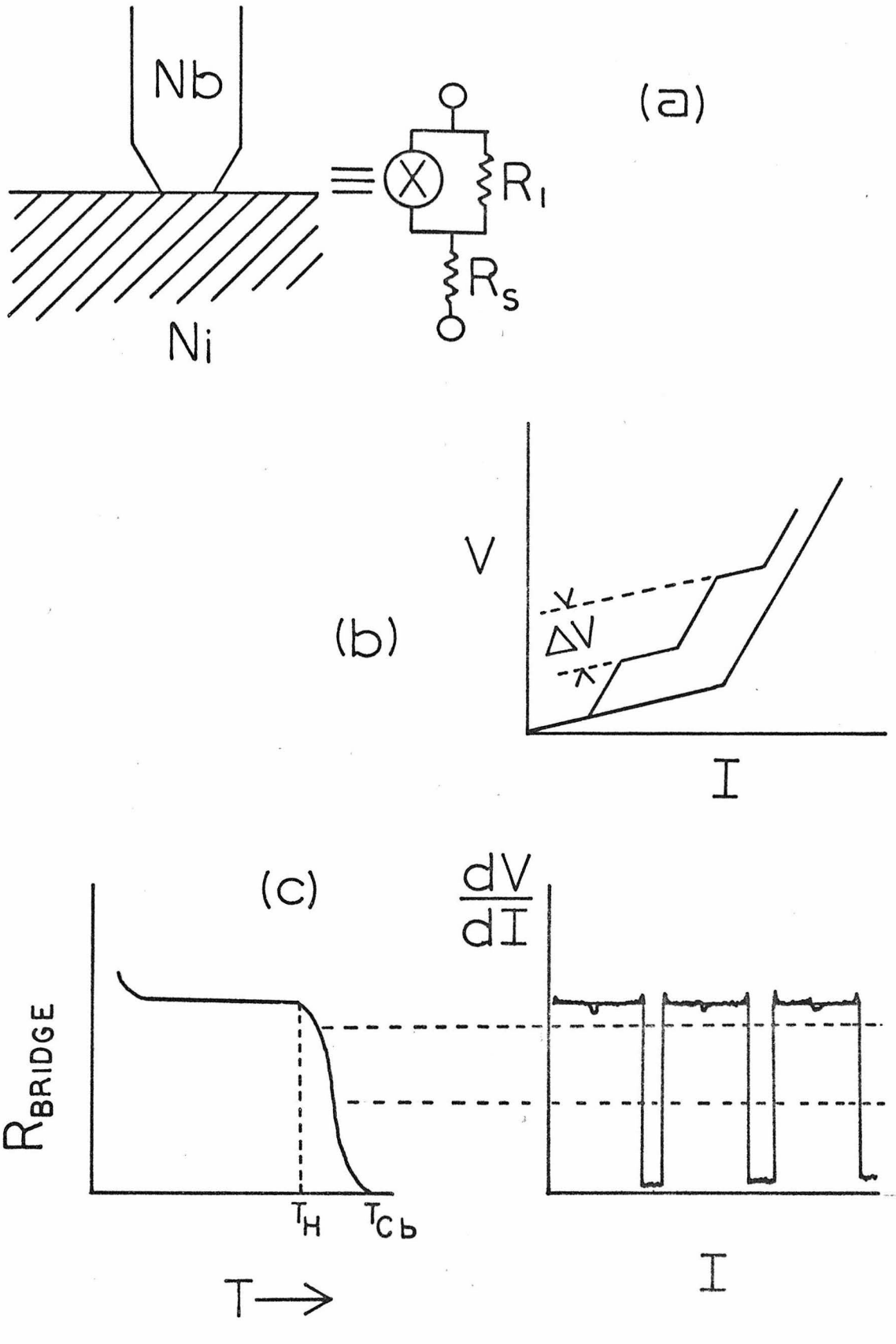
Nb
Ni
(a)
R_1
R_s
(b)
V
ΔV
I
(c)
$\frac{dV}{dI}$
R_{BRIDGE}
T_H
T_{Cb}
T →
I

frequency relation that is obeyed by the interference currents, and whether only one wave function was involved in the interference.

Previous attempts had been made to locate interference at strong superconductor-normal metal film interfaces with no success.[3] In the experiments reported in this thesis, many unsuccessful attempts led to the variation of superconducting electron and lattice variables (see Figs. 4.2,4.3). Eventually "critical currents" and microwave induced step structure were discovered, and were found to depend critically on the equilibrium spatial variation of superconducting pair density near the boundary. The existence of microwave induced steps in the interface I-V characteristics was used as the criterion for quantum interference. The relationship between the extrapolated interface voltage and step frequency was found to be modified from the usual Josephson relation by an integral factor, $f = 2eV/h\nu$, where f was never 1, often 1/2, and occasionally other values such as 1/4 or 1/10.

The time average voltage associated with the interface was determined from the experimental voltage, which was measured from the superconducting side to well within the normal side of the interface. This measurement included the interface voltage as well as that due to resistance of the normal metal (the spreading resistance) and was corrected by subtracting the normal potential drop.

This experimental fact of quantum interference occurring at a single boundary has as yet no theoretical explanation. However, as a result of this work it is suggested that the phenomenon has to do with an oscillation in the position of the boundary region, and that this

Fig. 4.2

Schematic representation of the constricted current flow S/N interface geometries tested. The width and length of the constricted region were typically .5μ. The darkened regions in the figures are the completely etched areas (substrate), the hatched regions are partially etched film (normal metal), and the plane regions are unetched (superconducting). Both Nb/Ta and Ta/Ti films were used to make these interfaces. The arrow marks the current path.

Only configuration (a) showed definite interface quantum interference. This result was interpreted as evidence that the current constriction had to exist on the superconducting side of the interface in order to locally depress the superelectron density.

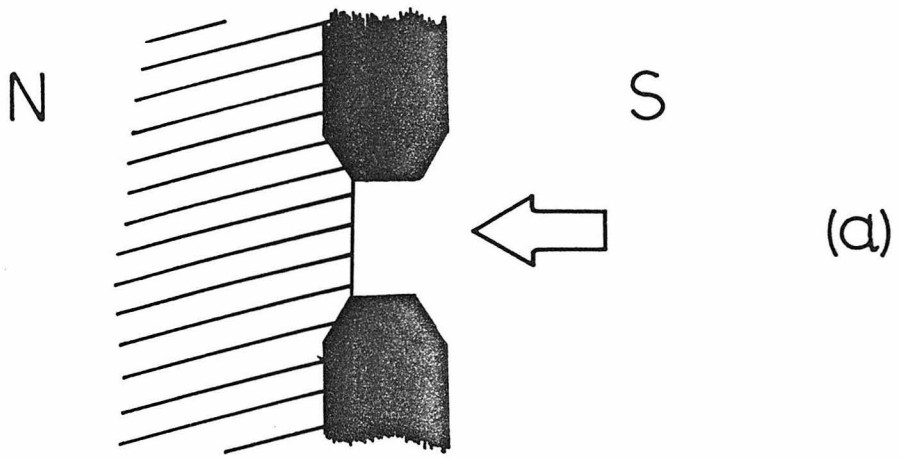
N
S
(a)

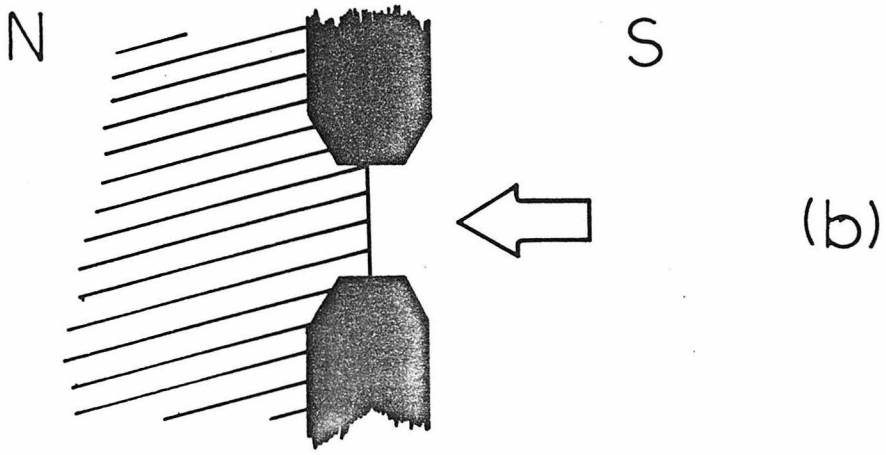
N
S
(b)

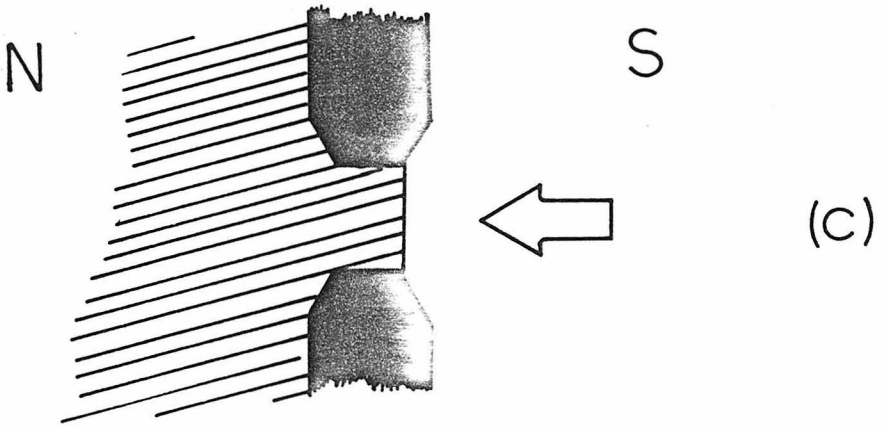
N
S
(c)

oscillation is greatly enhanced if both the pair density gradient and the pair density are small at the interface. Apparently, below some "critical current" the boundary is stable but upon exceeding this critical current the boundary becomes unstable (or "active") and oscillates at some characteristic frequency. Unlike the normal Josephson relation which was derived for a time dependent interaction between two large time independent superconducting states, the pertinent relation for this effect must take into account the fact that both the amplitude and phase of the boundary state varies in space and time.

4.1 Experimental Methods

To reproduce and extend in planar geometry the superconducting point experiments, several one-micron interfaces were constructed (Fig. 4.2). Three combinations were tested: a superconducting point butted against a normal half plane (a), a normal point butted against a superconducting half plane (c), and a normal point butted against a superconducting point (b). Samples were made both on Ta/Ti and Nb/Ta films.

In order to determine the existence of time dependent quantum interference currents in the interface, three methods were used to search for microwave induced Josephson step features. First with incident rf radiation a simple tracing of the I-V characteristic was made using completely chopped current bias and a tuned lock-in voltage amplifier with the ability to monitor differences below the microvolt level. To further enhance small signals a differential resistance measurement was made using .1-1 microampere 400 Hz current along with a DC bias, again with a lock-in monitor. If no rf related features were observed with

Fig. 4.3

Many constant current density interface geometries were tried before the active W/N version of an S/N interface was found. In the figure the hatched regions have been partially etched to form normal metal, whereas the plain areas represent superconducting film. The lattice S/N interface is defined to less than 250Å by the fabrication techniques used. The current flow is horizontal. Nb/Ta films were used for most of these configurations.

(a) The first configuration is that of a strong superconductor-normal metal interface. Neither critical currents nor interference were seen in the I-V characteristics of this geometry. Although the temperature was varied during tests, the transition temperature of the S region ($5.5^{o}K$) was always well above the experimental temperature.

(b) To check whether either a close series resistance would damp interference in a bridge, or an active proximity bridge would excite a S/N interface, the geometry in (b) was tested. The strip of normal metal formed a bridge which gave steps to incident microwave radiation even though a film of about 3 ohms was in close proximity (with its Johnson noise). The step structure seen showed no modification that could be attributed to the single S/N interface.

(c) In order to eliminate the several ohms of normal material in series with the S/N interface, one side, S_2 , of the interface was etched so that its transition temperature was at $4.0^{o}K$. Thus when operating the S_1/N interface at $4.0^{o}K$ very little series resistance existed, and yet such a geometry would not show proximity bridge interference. Unfortunately, complicated interwoven effects made this geometry useless in the S/N investigations.

Fig. 4.3 (continued)

(d) An N/S/N geometry is an antiproximity effect bridge. With $T_{cs} = 5.5^{o}K$ and operating at $4.2^{o}K$ neither critical currents nor quantum interference were seen.

(e) By partially etching the superconductor, a weak (W) region was formed which had a $T_{cw} = 4.4^{o}K$. The interface between W and N showed critical currents, and rf step structure over a temperature range $3.8 < T < 4.3^{o}K$. The length of W was varied from 10μ to .5μ with no change in behavior of the W/N interface. Thus the "S/N" interface is active if the superconducting side is near its transition temperature so that the pair density is small and the density gradient at the interface is small.

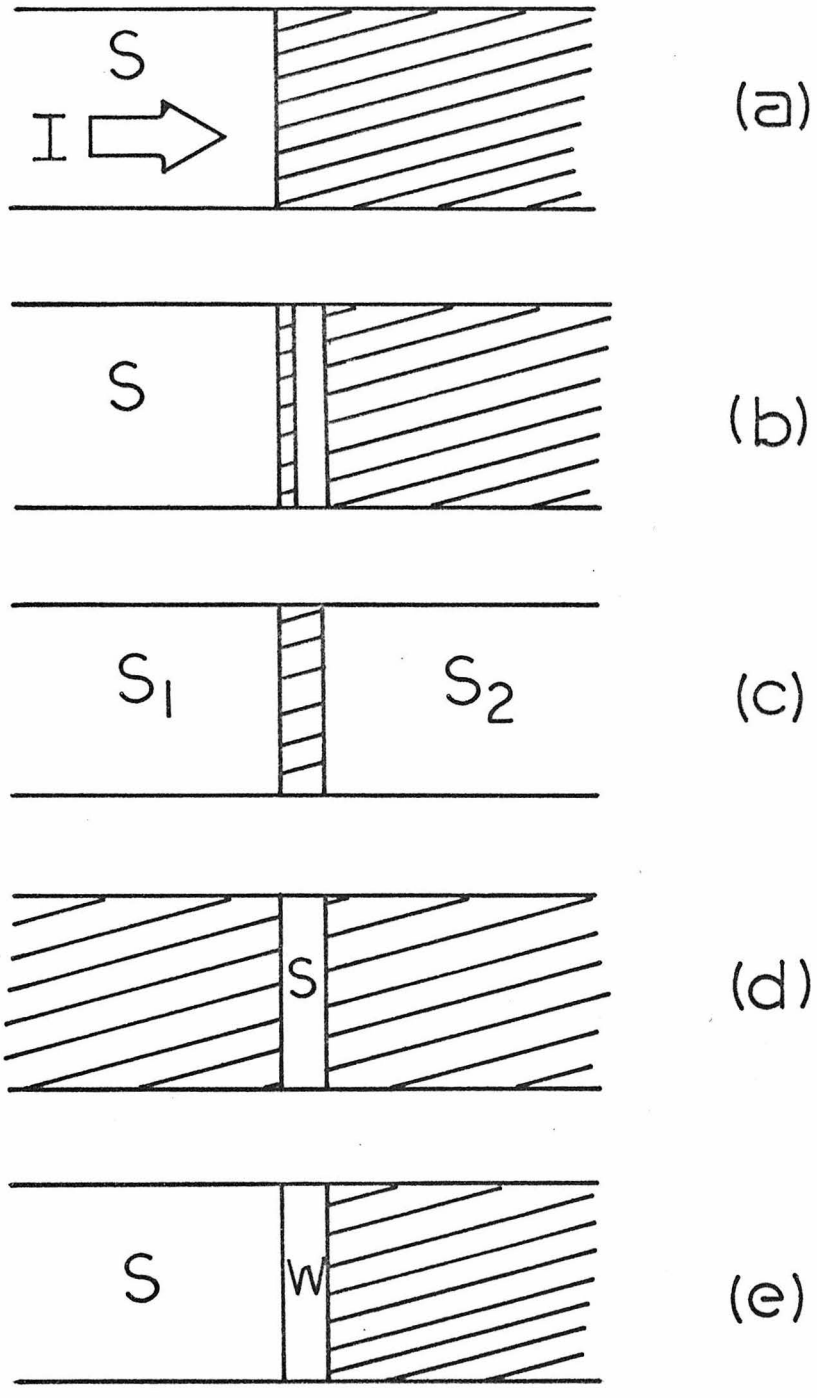
S
I
(a)
S
(b)
S1
S2
(c)
S
(d)
S
W
(e)

either of these methods a third method, responsivity, was used. By chopping the incident microwave radiation but keeping a constant current bias through the interface, a chopped voltage signal resulted representing the difference in the I-V characteristics with and without radiation at that bias. Slow sweeping of the bias current relative to the chopping frequency produced a plot of $I - \delta V_{rf}$. This method was especially sensitive in finding small changes in the I-V characteristics at low rf powers (see Appendix B).

All geometries were tested in a temperature range well above to well below the transition temperature of the "normal" film component. For example, the S/N interface was tested effectively as an S/N, S/W, and S_1/S_2 interface. In later tests it was found important to test higher temperature ranges where the interface was W/N and N_1/N_2.

Microwave power was varied over a 70 db range with frequency set at .5, 1, 2, and 10 GHz. Maximum power produced large enough rf currents in the structures to drive the superconducting areas normal, and the minimum power shifted the I-V characteristic below the lower limit of our detection system (.1 nanovolt). To indicate the sensitivity and inclusiveness of this search, by comparison an ordinary proximity effect bridge would show very pronounced Josephson step features over this range of temperature, rf power, and frequency.

Fabrication techniques have allowed interface definition down to less than 250Å (resolution limit of SEM observational system), hence the real interface is sharp on the scale of the proximity effect diffusion. Resistance per square of the Nb/Ta film was typically 2-4Ω, suggesting

that the normal semiplane forming the S/N interface would place several ohms in series with any active interface.

4.2 Characteristics of Constricted Interface Geometrics

The superconducting point against the normal half plane (Fig. 4.2a) demonstrated sharp "critical currents" and microwave-induced steps as was seen in previous work with a superconducting point contact against a bulk normal metal, whereas the other planar point contacts (Figs. 4.2b,c) showed no quantum interference effects. The most salient feature was the existence of several "critical currents" in the point I-V characteristic (Fig. 4.4); the resistance being a gradual function of current until a "critical current" was reached. At the critical current the resistance abruptly assumed a higher constant level. This change in resistance (or "resistance step") was equivalent to a normal region of 500-1000Å in length being inserted into the current path. The dependence of this critical current on temperature was exponential as in the case of a proximity effect bridge. Depending on the temperature of operation, 1 to 5 of these critical currents have been observed. As the temperature (and thus critical currents) were changed, the magnitude of the resistance step was found to remain constant.

Another feature in common with three dimensional point contact experiments was that rf steps could be introduced in the I-V curve above the critical current (Fig. 4.4). In this experiment these steps show up as a modification of the differential resistance measured across the interface. Three arguments are made for localizing the quantum interference at, or very near the interface. First, when the

Fig. 4.4

Typical differential resistance-current characteristics of a S/N interface of a planar point contact. The top trace shows two critical current resistance steps when no rf radiation is present. The resistance increases slightly between resistance steps with this "point contact", whereas with the constant current density interfaces the total resistance is constant between resistance steps.

The middle trace shows rf step structure induced in the first interface resistance step. The full interface resistance is modulated by the rf. The interface voltage spacing of these steps is constant to within 1%.

With application of more rf power, rf steps can be induced through the critical currents without a voltage step spacing change. This evidence supports the view that the second resistance step represents another degree or state of the first resistance step and not just a similar process in spatial series with the first.

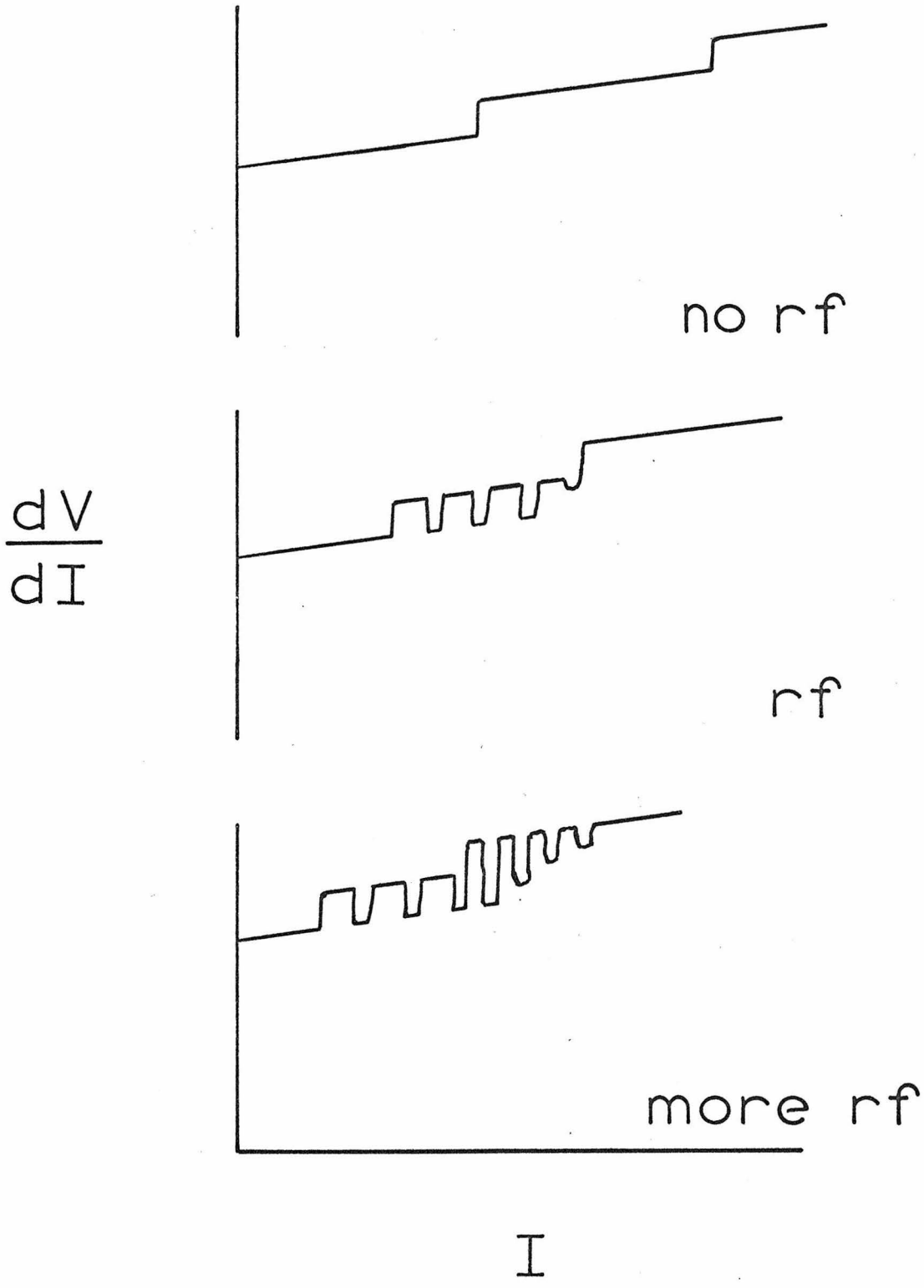
no rf
rf
more rf
dV/dI
I

last half micron of superconducting point was changed to normal metal the interference ended (Fig. 4.2c). Secondly, the resistance steps corresponded to 500-1000Å of normal material, so could not represent the resistance of the complete geometric point. Third, the pair density was lowest at the interface due both to the proximity effect and to the increased current density, hence the weakest superconducting region was at the interface.

The fact that quantum interference was only seen in the case of a constriction on the superconducting side of the interface suggested that a suppression in pair density, in this case by the large current density, was necessary before the S/N interface would show interference. The increased current density near the interface depressed the pair density creating a virtual S/W/N configuration. This suspicion was tested by the construction of constant width S/W/N configurations on Nb/Ta films by thinning the film in a staircase pattern (see Fig. 4.3e). This pattern did in fact lead to the same quantum behavior thus confirming the importance of the low pair density and gradual density gradient for creating quantum interference at an interface. The length of the weak region was varied in order to locate the quantum interference. With a length change from 10 to .5μ the interference was unchanged. This indicates that the location of the boundary between strong and weak is not critical and thus the phenomenon is located at or near the W/N boundary and is not dependent on S. As an additional check, S/W boundaries were investigated and found stable over the range of parameters used in the investigation of the W/N interface.

A conclusion from this work was that quantum interference at a single interface could be seen when a depression of the superconducting pair density existed near the interface either by increased current density in a point contact or by an adjustment of the equilibrium transition temperature in the constant current density interface. This experimental observation can be interpreted as the need to have both a small gradient and small amplitude in pair density at the interface to promote time dependence. In contrast an interface between a strong superconductor (one well below T_c) and a normal metal would have a large gradient in pair density; at interfaces with large pair density gradients no interference was seen.

The facts that rf step structure with similar temperature and power dependence could be induced in each resistance step of an interface, and that all critical currents of an interface had the same exponential dependence suggested that the same physical process was involved in each critical current transition. Furthermore, there was compelling evidence to indicate that the various critical currents not only represented the same physical process but another "state" of a single modification which occurred at one spatial region in the interface. Experimentally, rf structure could be induced continually through successive critical currents with no change in the voltage spacing of the steps (Fig. 4.4c). However, any description that uses the occurrence of some physical process in spatial sequence would require the series addition of the interface voltages in the voltage-frequency relation as is the case with series proximity effect bridges. Such a serial occurrence would cause a change ($\sim$ doubling) in step spacing when passing a critical current value.

No change occurs, thus each successive critical current can be looked at as the onset of another electron interface state caused by the same physical process and involving the same spatial region.

An example of such an allowable physical process is schematically illustrated in figure 4.5. When the first critical current is reached, the pair density distribution becomes unstable and oscillates between two mean distributions or "states", A and B. When the second critical current is obtained a third state, C , becomes viable. The frequency of oscillation between the states is determined by the characteristic length that separates the mean pair distributions of the two states.

A physical criterion that might lead to this nonequilibrium state can be found by setting the superconducting condensate recovery time, τ_{G-L} , equal to the reciprocal of the Josephson frequency which results from the voltage drop at the interface. An earlier investigation has shown that in nonequilibrium (see figure 4.5)

$$\mu_p - \mu_e = \frac{m\xi^2(T)\ \nabla \cdot j_s}{4|e|\tau_{G-L}|\psi|^2}$$

Regrouping the factors and identifying the frequency of interference as $\nu = 2(\mu_p - \mu_e)/h$ this criterion becomes

$$1 \sim \nu\tau_{G-L} \sim \left(\frac{\lambda^2\mu_o}{A}\xi\right)\left(A(\nabla\cdot j_s)\xi\right)\left(\frac{2}{\phi_o}\right) \qquad (4\text{-}1)$$

The first factor can be identified as the kinetic inductance, L_s , in a coherence length, ξ . The second factor can define a critical current or a critical supercurrent divergence per coherence length, that is

$A(\nabla \cdot j_s)\xi = A(j_c/\xi)(\xi) = Aj_c = I_c$. Thus the interference frequency becomes comparable to the inverse of the condensate relaxation time at a critical current of $I_c = \Phi_o/L_s$

For numerical evaluation, consider the pair density in this nonequilibrium state is equivalent to that in equilibrium .1°K below the transition (λ = 1μ, $\mu_o = 10^{-6}$, ξ = .1μ, A = 20μ x 200Å). Placing these numerical values into equation 4-1 gives a value of $2mA = I_c$. This is almost an order of magnitude too high. However, as the superconductor is made stronger (temperature lowered) λ approaches 1000Å and ξ approaches 100Å , and this places $I_c = 2A$, a value high enough to explain why the strong superconductor normal interfaces have not shown interference.

The resistance step at each critical current indicates a length of 500-1000Å of equivalent normal metal has been placed in the current path. The nonequilibrium distance, d , that would correspond to this comes from a recovery time of 10^{-12}sec, where $d = \sqrt{\ell v_F \tau}$

4.3 Properties of the Constant Current Density Interface Geometries

The qualitative features of the planar point contacts and constant current density interfaces were the same, that is, the characteristic lengths deduced from the resistance step at the critical current were identical and the rf induced structure was the same in temperature and power dependence.

The critical current of a constant current density interface has an exponential dependence on temperature for the first few decades of current (1-1000 μA), $I_c = I \exp(-\beta T)$. The exponential factor β

Fig. 4.5

One possible modification to the pair density distribution that could explain many of the features seen in the S/N interface experiments is shown in (a). The pair density given by curve A represents the equilibrium proximity density. After the first critical current is reached the density distribution becomes unstable and oscillates between the extremes represented by curves A and B. The characteristic distance between these distributions is 500-1000Å accounting for the measured resistance step. When the second critical current is reached another distribution "state" C becomes relevant.

Graph (b) shows the average potential distributions found in previous work[3] for a current carrying S/N interface. μ_p is the superconducting electron potential and μ_e the normal electron potential. The expression given is the relation found between supercurrent and potential imbalance.

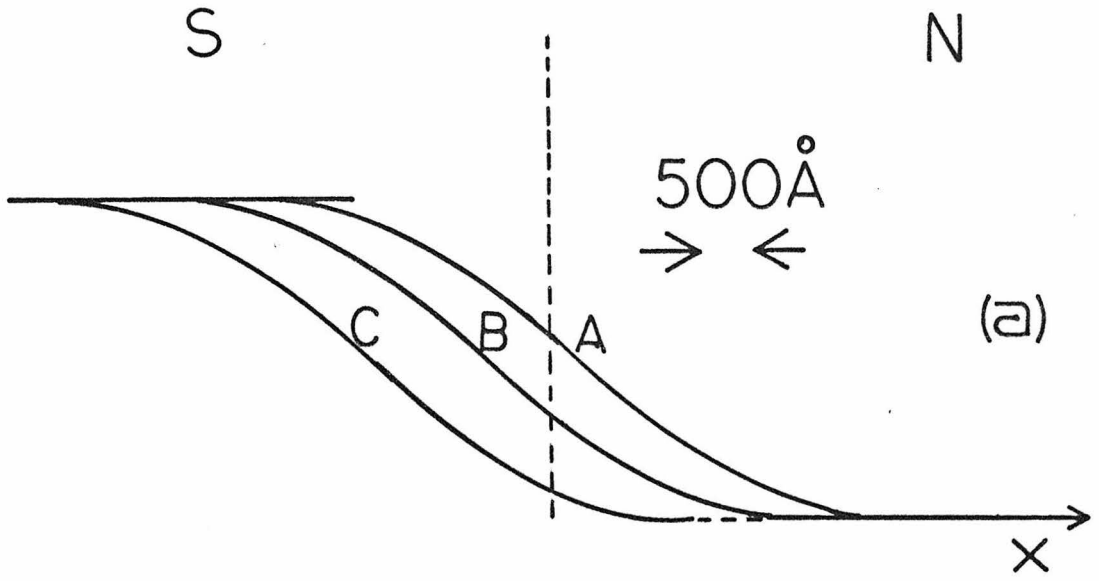

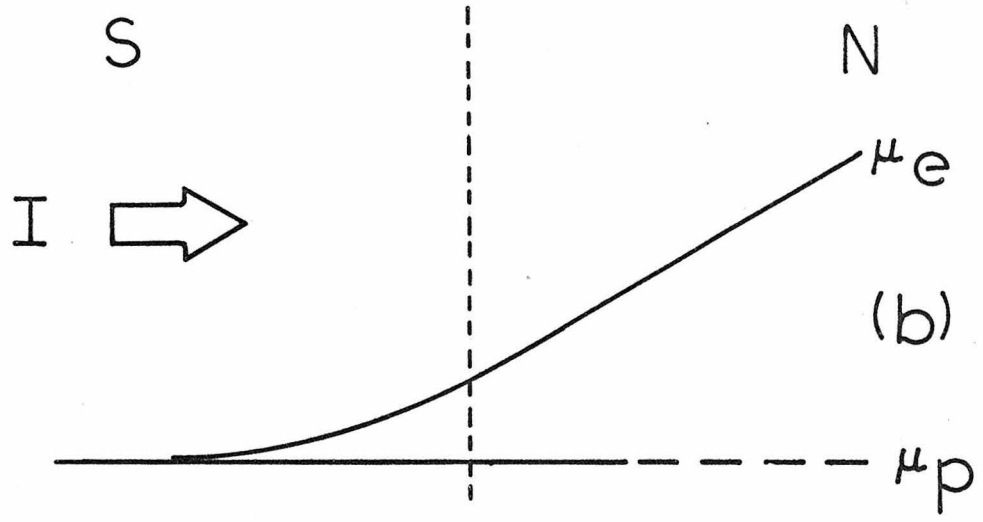

$$\mu_p - \mu_e = \frac{m\,\xi^2(T)\,\nabla \cdot j_s}{4\,|e|\,\tau_{G\text{-}L}\,|\psi|^2}$$

is typically twice as large as that of the critical current dependence in .5μ proximity effect bridges on the same film (Fig. 4.6a). This exponential dependence was taken as a strong indication that the proximity region of the interface contained the quantum interference.

However, as the temperature was decreased it was found that the critical current became multiple valued. When the temperature was lowered from a region where only one critical current was present, other resistance steps (critical currents) appeared. With decreasing temperature the appearance of each new resistance step was as if another 500Å region at the proximity interface had undergone a change from normal electron flow to time dependent superelectron flow. The amplitude of a particular resistance step was not a function of the temperature or current, and there was no other change in resistance besides the distinct resistance steps. On all interfaces tested the first few resistance steps were of nearly equal amplitude (± 10%) with additional smaller resistance steps at higher current density. The characteristic current spacing between resistance steps for all tested 20μ wide constant current density geometries was about 300 μA (± 10%) in the temperature range where rf steps could be induced.

Step structure again disobeyed the Josephson relation, obeying instead

$$f = \frac{2eV_{boundary}}{h\nu} \qquad (4\text{-}2)$$

where f was never 1, often 1/2, and occasionally other values such as 1/4 and 1/10. These measurements were done with an absolute voltage accuracy of 5%. Equation 4-2 is in contrast with the modification of the Josephson relation found in series arrays of proximity effect bridges

in Chapter III

$$n = \frac{2eV_{array}}{h\nu}$$

where n was the number of bridges.

The voltage spacing of rf steps ($V_{boundary}$ in equation 4-2) was constant for any given resistance step of an interface. That is, the voltage spacing between successive rf steps in the same resistance step were equal (to within the 1% relative voltage experimental accuracy), and also (within one resistance step) the voltage spacing (or the value of f in equation 4-2) was not a function of temperature or frequency (200 MHz - 10 GHz). The value of f in equation 4-2 was not the same for all resistance steps. In this investigation the smaller resistance steps tended to have larger values of f . Perhaps in the limit of a continuous resistance change at the interface instead of step increases this fact would imply absence of induced rf step structure.

All rf induced steps showed the standard size dependence on rf power that would be expected for a simple Josephson tunnel junction (Fig. 4.6b). This fact strongly argues against any possibility that the measured step structure was really not the fundamental and higher harmonic steps but rather submultiple steps of the incident radiation. If these steps were 1/2 or 1/4 steps, the Josephson frequency-voltage relation could still be considered valid. However, if the interface does act as a perfect frequency doubler it is possible to explain the experimental step size Bessel relations. However, it seems highly unlikely that any one process could also be a perfect frequency quadrupler or larger multiplier as would be required to explain the other values of f . Consequently this experimental evidence is interpreted

Fig. 4.6

The critical current and induced rf steps associated with S/N interface interference are very similar in behavior to that found in the proximity effect bridge.

The exponential temperature dependence of all critical current features (a) are characteristic of 1.5 - 2μ long proximity effect bridges on the same films.

The step size behavior with rf power (b) parallels the behavior of proximity effect bridges very closely, $\Delta I_N \propto I_o J_N(2eV/h\nu)$. This dependence was used to show that the first, second, and third step features experimentally measured were indeed the first, second, and third steps of the incident radiation and not, for example, the 1/4, 1/2, and 3/4 steps. This observation helped confirm that the Josephson relation was substantially modified at the S/N interface.

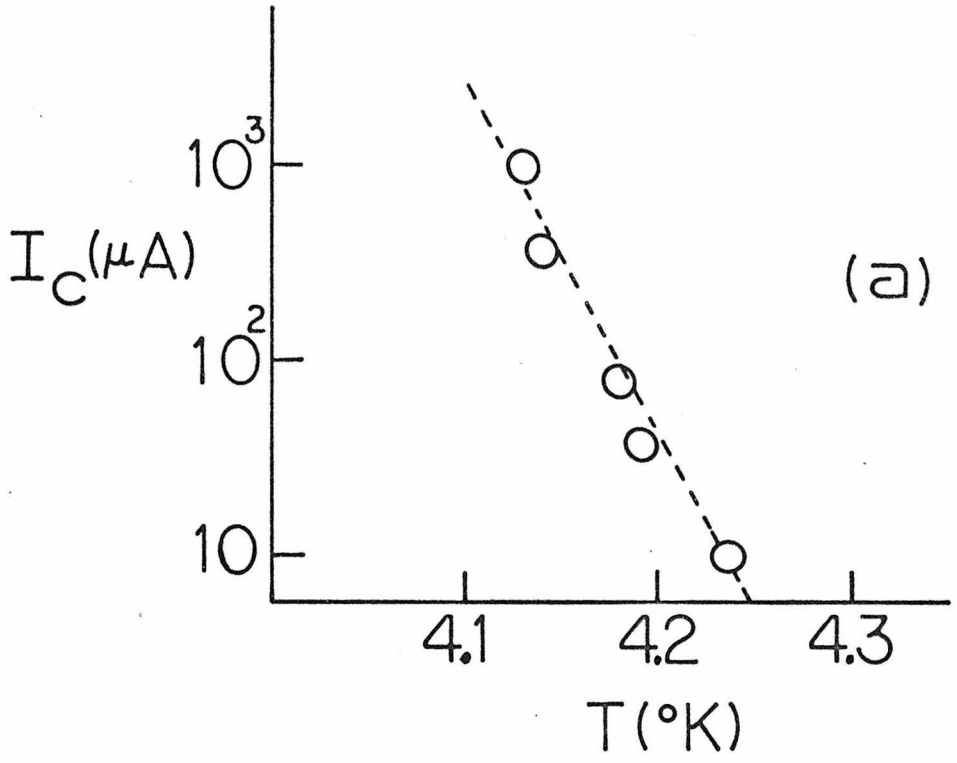
$I_c(\mu A)$
10^3
10^2
10
4.1
4.2
4.3
T(°K)
(a)

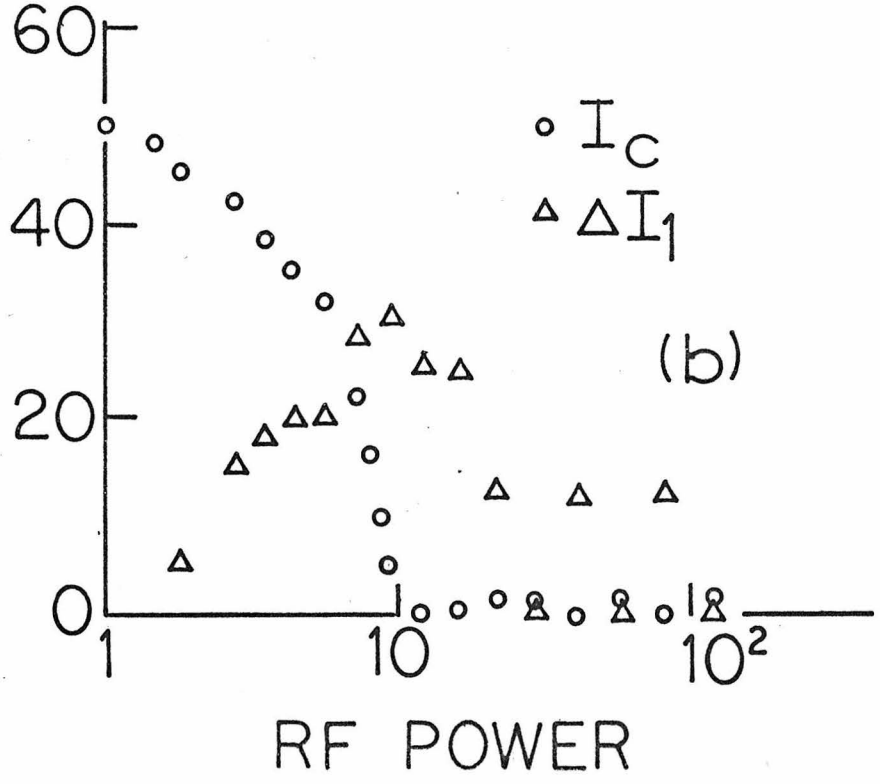
60
40
20
0
1
10
10^2
I_c
ΔI_1
(b)
RF POWER

as a modification of the Josephson relation.

Magnetic field dependence of the critical currents was also tested. An external field suppressed the critical current to zero monotonically, unlike the periodic quantum interference modulation of the Josephson junction or proximity bridge. The field necessary to suppress a critical current was larger ($\sim$10 times) than the field necessary to modulate a proximity effect bridge of the same width and critical current. This lack of quantum interference with magnetic field could be interpreted as evidence that the interface interference is not between two time independent macroscopic wave functions for which a strong modulation is known to exist. Thus the magnetic field results lend support to the one-wave function interface interference.

4.4 Summary

This investigation has found that although the electron pair density at the boundary between a superconductor and normal metal is stable for low current levels, there is a critical current above which the boundary becomes time dependent. This time dependence can be described as an oscillatory motion of the interface between the superconductor and normal metal. This single time dependent superconducting state shows quantum interference effects somewhat similar to the Josephson effect between two weakly coupled superconductors. The measured voltage-frequency relation for the interface is considerably modified from the Josephson relation ($V = h\nu/2e$). The interface oscillation requires voltages which are fractional (1/2,1/4) values of the above. The characteristic nonequilibrium distance measured for the films used in this S/N interface investigation was 500-1000Å. A nonequilibrium relaxation time of 10^{-12} sec would account for this distance.

APPENDIX A

FABRICATION

A.1 Substrates

To construct and systematically vary the geometric and electronic parameters of superconducting thin film devices many new fabrication techniques had to be developed. For the particular interface investigations of this thesis it was necessary to intensively develop submicron resolution photoresist exposures by microscopic projection and highly uniform thickness etching, using both anodization and an Ar ion beam. These techniques allowed pattern edge definition of less than 250Å, resolution down to .2μ, and local film thickness control of ±5Å.

All superconducting wave function studies were done on thin metal films. To ensure homogeneous predictable films, polished uniform substrates were used. The three most common substrates were:

1. Corning 7059 glass, a glass with a special polish for thin film work,
2. Union Carbide sapphire, polished to their finest finish (one grade better than optical),
3. Standard highly polished silicon wafers with room temperature resistance of greater than 4Ω-cm in order to ensure that such a substrate will become an effective insulator at liquid helium temperatures.

Before evaporation all substrates were vigorously cleaned with the following process:

1. scrubbed in detergent and water;
2. rinsed for 5 minutes in distilled water (rinsed);

3. blown dry with dry nitrogen so the jet first removes the puddles of water and then dries the adsorbed layers (blown dry);
4. sprayed with reagent grade acetone for 30 seconds (acetone);
5. blown dry;
6. washed in Chromerge (Chromerge is a trade name for a chromic-sulfuric acid cleaning solution marketed by Monostat.) to remove any organic residue for a few minutes;
7. rinsed;
8. blown dry;
9. acetone;
10. blown dry;
11. washed in ethanol for 30 seconds;
12. blown dry.

Obviously if the slides were freshly unpackaged only the post-Chromerge steps were necessary.

A.2 Metal Films

Two classes of metals were evaporated onto these substrates; the low melting temperature metals were resistance boat evaporated, and the refractory metals were electron beam gun evaporated. The low melting temperature metals most frequently used were Au, Sn, and In. Glass bell jar diffusion pump systems were used. Both 4 and 6 inch pumping port systems seemed adequate but the 6 inch system gave faster pumpdown and 10^{-7}torr pre-evaporation pressures. Actual evaporation took place in 10^{-5} to 10^{-6}torr, due both to the vapor pressure of the metal and the

heat of the evaporation exciting contaminates from their absorbed positions. To avoid diffusion pump oil contamination of the films, both a water and a liquid nitrogen baffle were needed. The substrates were located 5 inches above the boat and the evaporation of the pre-measured melt was as short a duration as possible to avoid excessive heating of the substrate (30 seconds). The substrates were neither externally cooled nor heated. It was necessary to heat the boat slowly until the metal melted or else an ejection of the half-melted sample resulted. Au films were found to be continuous when more than a few hundred angstroms were deposited and Sn films were made uniform by first coating the surface of the substrate with Siliclad (manufactured by Clay Adams, Inc.) to avoid the Sn-glass variations in sticking.

The refractory metals had to be evaporated in a higher vacuum system. A stainless steel system with sorption pumps for initial roughing and a sublimation pump and ion pump assembly allowed a pre-evaporation vacuum of 10^{-9} - 10^{-8}torr. E-guns of at least 2 KWatts were necessary to melt W, Ta, Nb, Zr, or Ti. Typically 300Å of a metal could be evaporated within 2 minutes without exceeding 10^{-7}torr in the system. Changing over to the second metal melt (when making a layered film) took a few minutes, but experimental tests indicate that no oxide layer grows during this time. Heating the sapphire substrates up to 400^{o}C resulted in more laterally homogeneous films with transition temperatures closer to bulk values than with cooler substrates. Transition temperature widths over working areas 1 mm square were 10 m^{o}K for these films. This was comparable to high purity bulk samples and thus allowed large homogeneous working areas. Anodic etching indicates that at most the

mixing interface between layers of refractory metals was 10Å thick.

A.3 Photolithography

Shipley 1350B photoresist (PR) was applied in a uniform thin layer over the metal films by either spinning or dipping and draining. First, the surface of the metal film was prepared by an acetone and ethanol wash, each followed by blowing off the solvent in a dry nitrogen jet. The dry gas jet was aimed so as to push the puddled liquid and included dirt off the film and then to evaporate the remaining surface layer of solvent. If the PR did not stick or was streaky in color it was necessary to rub the metal film with an acetone soaked Q tip (refractory films only). Spinning gave a uniform thickness PR film over a 2 inch diameter area with the only irregularities near the substrate edge. Spinning rates determined the thickness of the PR film: 4000 rpm gave 1μ and 10,000 rpm gave .5μ.

Exposure of a pattern in the PR was accomplished using contact masks and a UV lamp for large detail over large areas. Contact masks were photographically easy to make and register when all detail was larger than 100μ and the area was limited to a 2 inch disk. This research also required finer resolution than was possible with existing methods. A standard Zeiss reflection light microscope was adapted to project patterns of finer resolution (Fig. A.1). The optical resolution of the microscope, .2μ, was achievable in PR pattern detail within a field of vision of 100μ.[1] Using less powerful objective lenses one could print projection patterns over a 2 mm field. Besides the ultimate resolution obtainable with microscopic projection, this method provided

Fig. A.1

A reflection microscope illuminator system was used to produce submicron details in photoresist patterns. A simple, inexpensive 20μ detail mask is placed in the Koehler illumination system at point F so that the pattern will be imaged upon the PR. The objective lens, O , causes a dimunition of the mask. For example, using a Zeiss RA microscope with a vertical illuminator II-B and a X100 oil immersion objective mask, reduction by a factor of 50 was achieved with a lower bound of .2μ on resolution achievable.

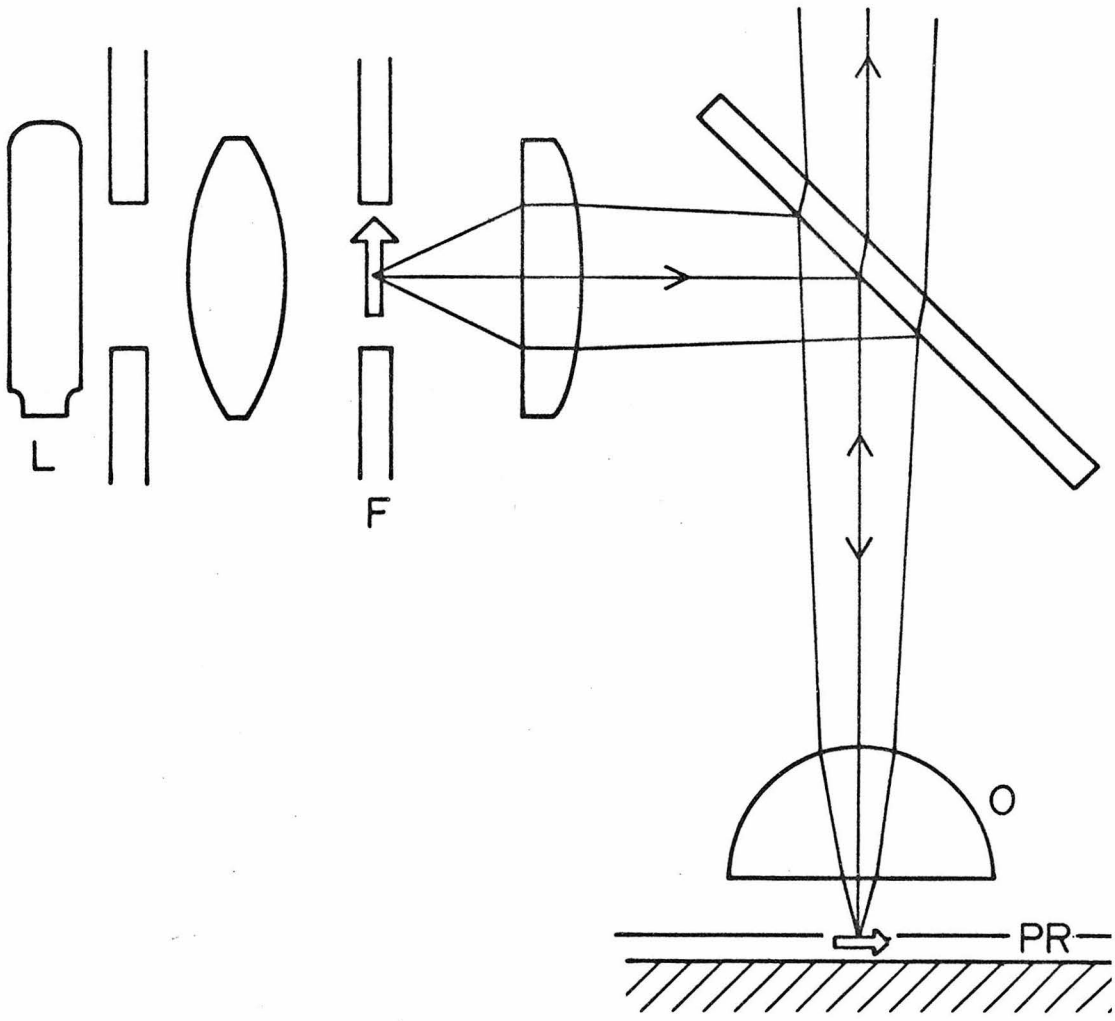
L
F
O
PR

two other advantages. First, registration of subsequent masks could be achieved to a .2μ limit. Second, since the mask pattern was projected backwards through the optics, a diminution of detail was gained. For example, a cheap 20μ wide line mask became a projected .5μ line with the RA Zeiss vertical illuminator optics combined with a x100 objective lens.

Various tricks have been discovered to work around the limited field of vision available when using high resolution objective lens. For example, a line .4μ by 1 cm was made by projecting a .4 x 25μ line pattern and uniformly translating the microscope stage (with a slow electric motor) parallel to the line mask. Similarly a row of 40 light dots under translation became a grid of 40 lines.[2] It was also possible to use separate exposures with overlapping fields to microscopically continue a pattern since registry between exposures was within .2μ. The highest resolution lenses required immersion fluid (oil or glycerin) to effectively shorten the light wavelength. Thus it was necessary to blot off the excessive fluid and rinse in water or developer before the standard PR development procedure was followed.

The array exposures were also made with laser interference[3] and Scanning Electron Microscope (SEM) techniques. Using an Ar laser beam (5145Å line), first split and then recombined in the plane of the PR, a grid pattern is exposed. The grid period could be conveniently adjusted from .2- 1μ by adjusting the angle between the recombining beams. A 1 cm square area has been exposed this way, producing at least 1000 grid lines. Shipley 1350B PR could also be exposed with the electron beam of an SEM. Using the raster scan mode of the beam, Dr. R. Kirschman of JPL

prepared many grid patterns for this investigation. Such grids had periods of 1, 2, 5, and 10μ with line widths of .5μ. Typically each pattern was .2 - 1 mm square. SEM exposure shows promise of being the most versatile and best resolving exposure system of the three investigated, but it would require an in-house SEM to reach the full potentials of such a system.

A.4 Etching

Once the photoresist pattern had been established, it was necessary to remove the metal in a controlled way from the exposed areas.

Large areas of soft metals could easily be removed by chemical etching. Aqua regia diluted with equal parts of water removed gold. Sn could be etched with a very dilute solution of aqua regia in ethylene glycol: 20 ml ethylene glycol, 40 drops aqua regia, 20 drops of hydrogen peroxide. Undercutting, the removal of metal under the plastic mask, occurred on the micron scale under the borders of the exposed area. Standard techniques of baking the PR mask and minimizing the etching time were no guarantee against undercutting.

For large areas of refractory films (Nb,Ta), a commercial instrument called the "Plasmod" (Tegal Corporation) was successful at etching. In this device a plasma rf discharge was excited in freon at a pressure of 200 mtorr. The radical F^- caused a non-liquid chemical etching of the exposed metal areas. There was still some undercutting, but less than 1μ, and very predictable. Zr and Hf were not etched with this system, presumably because the reaction of F^- with these metals or their natural oxide did not give a gaseous product. This method gave only yes-no etching, no depth control was possible.

Fig. A.2

Schematic illustration of a simple liquid anodization technique for $\pm 5\text{Å}$ controlled etching of refractory films. The photoresist pattern E defines the metal film region to be etched. A drop of boric acid solution B covers the pattern. A voltage ramp A is applied across the metal film by placing a Au wire F into the drop and pressing another wire onto a distant spot on the film with an In tab C . The current that flows can be easily monitored across a resistor R . For equilibrium etching, the ramp slope in volts/sec must be chosen small enough so the current flow D is constant for each different layer of refractory film.

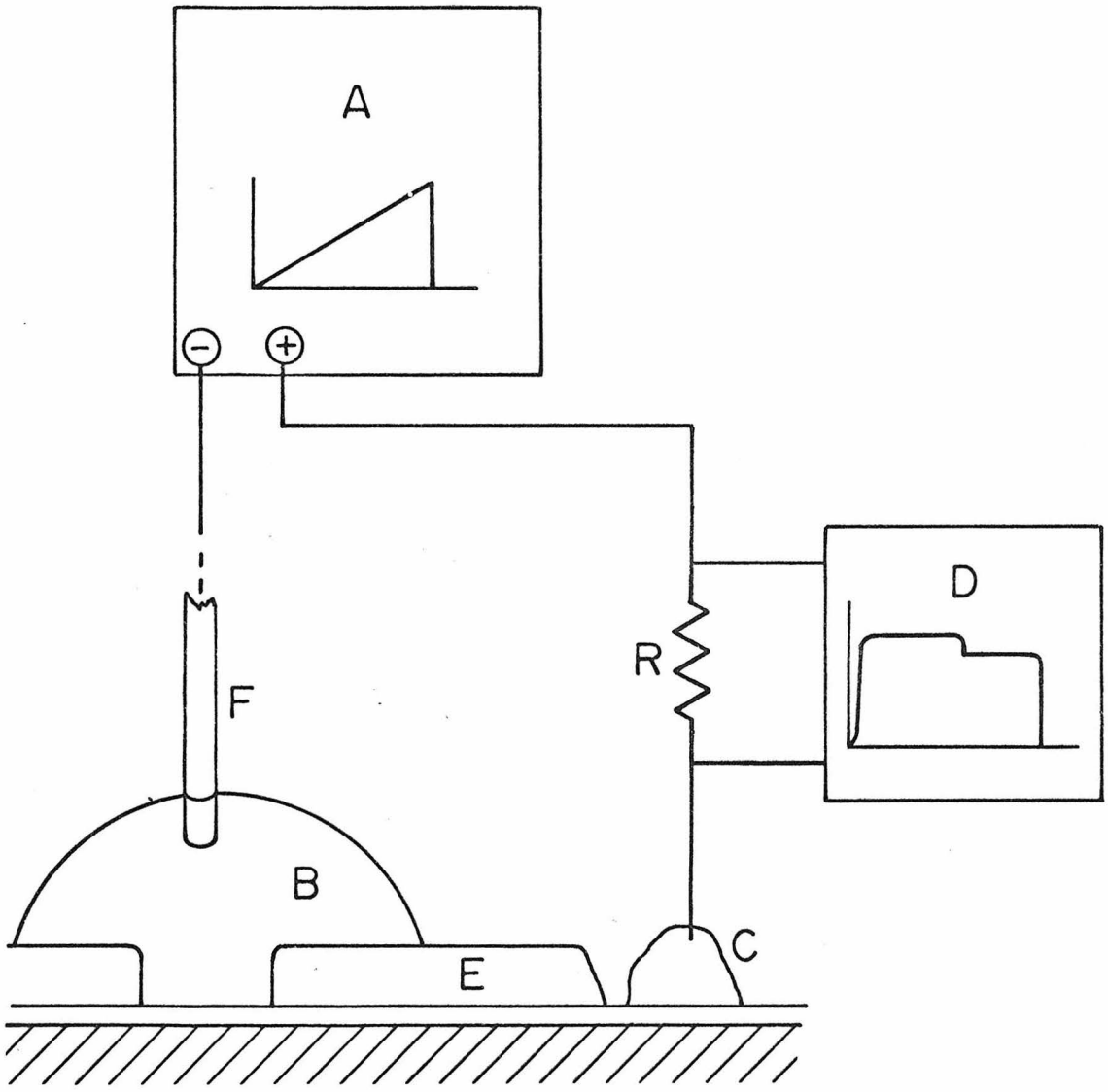
A
D
R
F
B
E
C

For small areas or regions where only a partial thickness of refractory metal was to be removed, anodization proved the most effective etching method. For ±5A thickness control over the small areas needed in this research, extensive anodization techniques were developed. The refractory metals formed hard nonsoluble oxides under liquid anodization. A drop of boric acid solution was placed on the exposed metal film defined by the PR mask. The refractory film was made positive and the drop was made negative by a gold wire electrode (Fig. A.2). The thickness of oxide that grew was proportional to the voltage applied. For example, Nb converted 6Å of metal to oxide for every volt applied, Ta-8Å/V, W-10Å/V. As a calibration precaution, there was a certain oxide growing rate not to be exceeded. When a voltage ramp, A , was applied between the drop and a well defined area of metal film, the current flow, B, would quickly reach a constant value (Fig. A.3). This signifies that no deficit of unanodized metal was building up and that an equilibrium rate had been achieved. If the current grew continually throughout the ramp then the anodization time was too short for the given area, and the thickness/volt calibration did not apply. Thickness control to within 5Å was achieved and undercutting was less than .1μ for areas small enough to be equilibrium anodized in 50 msec, for example, 10 x 10μ area at 50 volts. Fine resolution work was done below 50 volts (∿400Å) and rough cutouts below 120V (∿900Å) or PR electrostatic breakdown became a problem.

Ion etching proved the best all around etching system. Both hard and soft materials could be etched in fine or rough detail over a 1 inch diameter area. The system built during this investigation had an rf

Fig. A.3

Detailed look at anodization voltage ramp A and current flow B. The ramp rate is chosen so that the current flow will quickly assume a constant value. The step change in curve B indicates that the top layer of Ta film is completely etched at 37 volts and the W film by 56 volts. When the anodization is done using this constant current flow equilibrium mode, there is a direct correlation between voltage and angstroms of metal oxidized. This calibration is $6\mathring{A}/V$ = Nb, $8\mathring{A}/V$ = Ta, $4\mathring{A}/V$ = W .

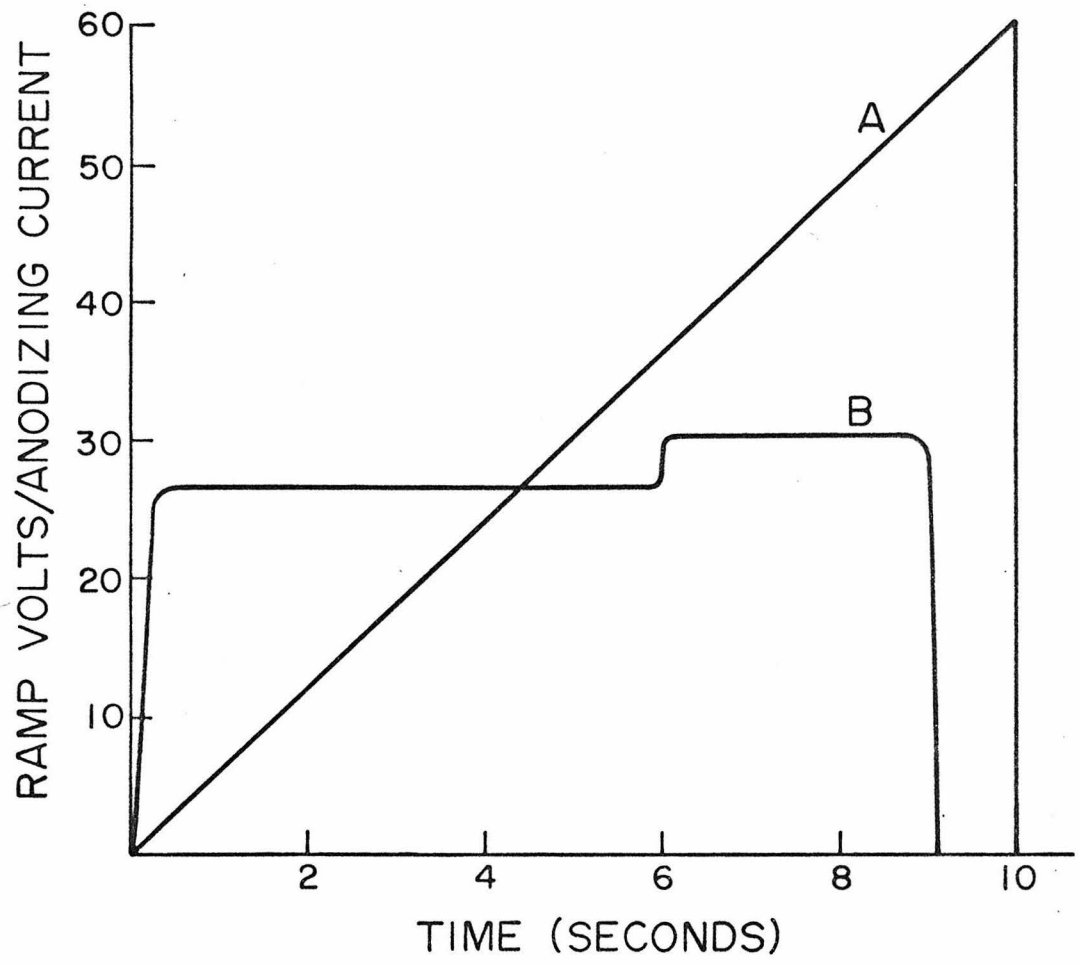
RAMP VOLTS/ANODIZING CURRENT
60
50
40
30
20
10
A
B
2
4
6
8
10
TIME (SECONDS)

plasma discharge of Ar gas at low pressure, 10^{-4}torr. This plasma was bled of its Ar^+ ions by a DC 1000V potential placed between one end cap and a small collimating nozzle in the opposite end cap (Fig. A.4). The nozzle bore was .2" in diameter and 1" long. The bore was made of Al to minimize the amount of sputtered material that would be deposited on the sample. The nozzle defined a cone shaped beam with a 7^o apex angle. The sample was placed about 5 inches below the nozzle and received about .2 mA current fairly uniformly over a 1 inch area. Etching rates were typically 1000Å/hour for Sn and Au, and 200Å/hour for Nb and Ta with 10% unevenness over the etching area. Etching rates could be increased in a number of ways. By placing the target 1 inch below the nozzle, rates 25 times these could be achieved over a correspondingly smaller area. Unfortunately, if the ion flux was too high the PR began to carbonize due to heating. Adjusting a solenoidal B field with its axis coincident with the nozzle, and making a nozzle collar out of high magnetic permeability material also greatly encouraged a higher flux of ions.

Several unanticipated design parameters became known while constructing the Ar ion source. First, no metal except the nozzle could be exposed to the plasma at the bottom of the plasma chamber. Even a crack in the bottom of the quartz tube would allow the 1000V accelerating potential to be shorted out. Silicon rubber O-rings could be used to make the end cap vacuum seals on the plasma chamber without "poisoning" the Ar plasma, as can be the case with a H^+ plasma. In fact, it was found that both ends caps should have silicon rubber gaskets between the glass and metal to avoid breakage as the parts were pressed together

Fig. A.4

Cross section of Ar ion source used in ion etching. All parts are cylindrically symmetric around a central vertical axis except the Ar gas leak E . The drawing is approximately the right size. Aluminum cap A acts as one end of the plasma chamber B and as the positive extraction electrode. The vacuum seal is made to the quartz chamber B using silicon rubber o-rings to withstand moderate heating. The o-rings are shown as solid black circles. C is the plasma itself being formed by Ar gas leaking in through channel E . The gas is ionized by two rf electrodes wrapped on the outside of B one inch apart, centered between A and D . A 100W 80 MHz power source was used to sustain the discharge. Base plate D was grounded so that with +1000 volts on end cap A the positive Ar ions would be accelerated toward the aluminum nozzle F . It was found very important that no metal show at the bottom of the plasma chamber except the nozzle. Enhanced ion beam output was achieved by placing a coaxial magnetic field at the base of the plasma chamber to concentrate the plasma near the nozzle. 200 μA of ion beam could be easily extracted, and with a magnetic material nozzle to help concentrate the magnetic field, up to a 1 mA beam has been produced.

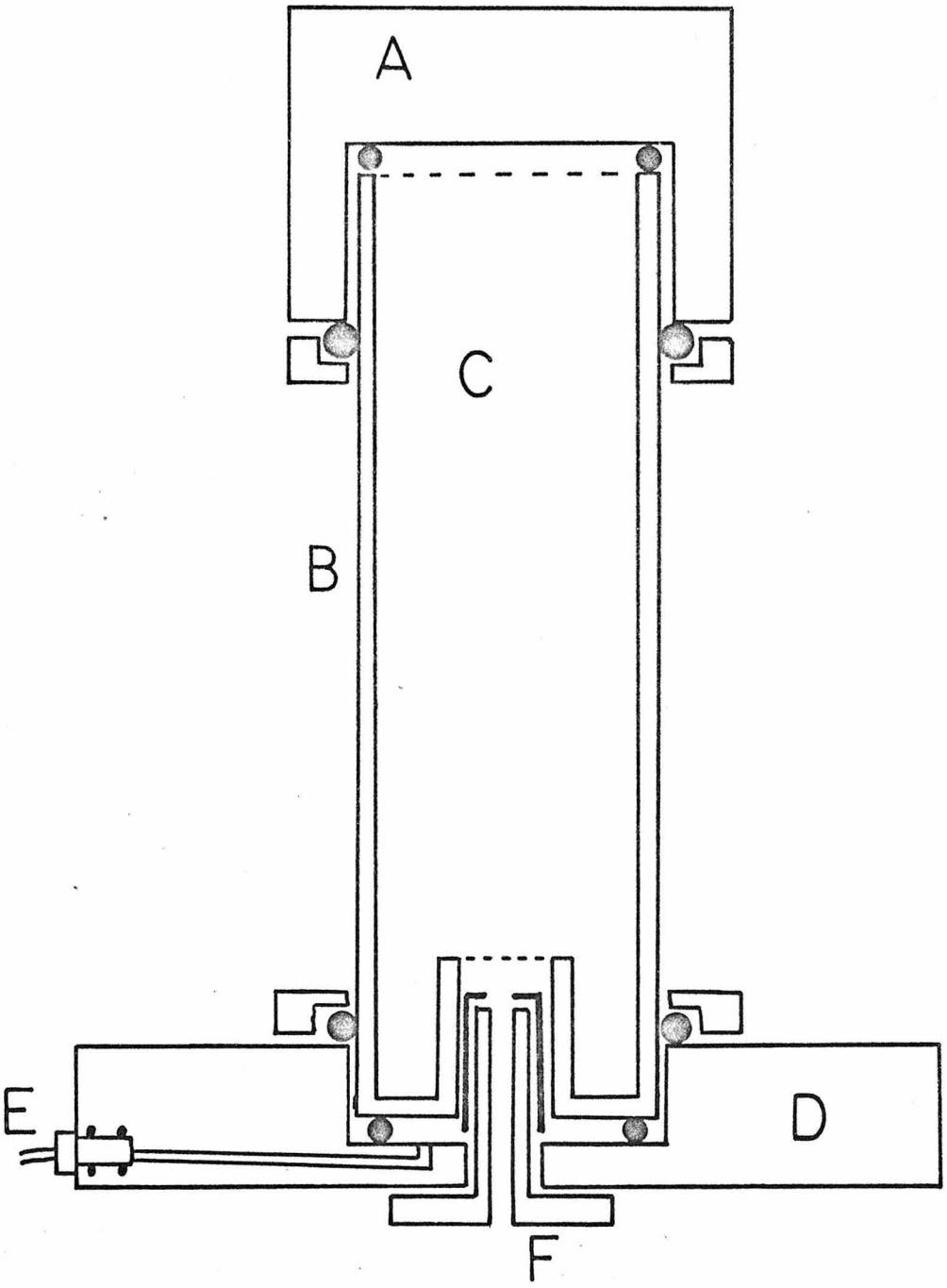
A
C
B
E
D
F

upon pulling a vacuum. The Ar discharge was normally blue, but after one hundred hours of usage a red glow appeared around the walls of the discharge tube. This effect was due to the gradual deposition of some scale on the tube walls. It was believed this scale was a result of the pump oil hydrocarbons interacting with the plasma. Simple brushing removed this deposit and returned the output ion current back to a high value.

There was no undercutting since the ion beam was highly collimated and the etching thickness limit was determined solely by the durability of the masking material. Shipley PR bombarded at the flux rates that gave 200Å/hour for Nb etched about 5 times faster than Nb. Thus a 1μ thick PR mask allowed 2000Å of Nb to be etched.

A.5 Contacts

The best contacts for experimental tests were simply pressed In contacts. 1 mm lengths of .02" In wire were pressed onto the contact pad regions of the thin film device. The end of a #38 tinned Cu wire was then pressed onto this In tab and another piece of In was pressed on top of the first. If the sample could be lifted by the wire, the contact was strong enough both electrically and mechanically. If the film surface was particularly oxidized or contaminated, In pressed contacts proved highly resistive; even though a four terminal measurement was being made, when the contact became as resistive as the input impedance of the voltmeter, trouble set in. This high resistance was avoided by first dipping a razor blade end in a dab of Wet Alloy (Hg, Th, In) and then using this to scratch the surface in the area where the contact

was to be made. The Wet Alloy prevented the scratched region from re-oxidizing before the In made contact. To make smaller area bonds or nicely packaged bonds a commercial ultrasonic bonder (Unitek) with a 1 mil $Al_{99}Si_1$ wire could be used with refractory metal films on glass, sapphire or Si.

A.6 Scribing

A hand-held diamond scribe was used to dice glass, Si, and sapphire substrates (if the sapphire was 15 mils or less thick). To protect the finished devices while scribing, it was advantageous to first coat the sample with PR and tape over the devices. One straight clean scribe was worth 1000 gauges; the idea was to form one sharp fault line where all the strain would be concentrated. Snapping was best accomplished with the scribed line directly over a straight edge.

APPENDIX B

EXPERIMENTAL METHODS

B.1 Temperature

Cryogenic temperatures were achieved with standard dewar techniques; a liquid nitrogen cooled outer dewar protected a liquid helium inner dewar. Devices were allowed to come into contact with the helium liquid. Temperature control was achieved by controlling the vapor pressure over the bath with a ballast tank manostat. Pressure could be easily controlled from 150 - .1 cm of Hg($5^{o}K$ - $1.3^{o}K$). Over most of this temperature range the bath could be held within 1 $m^{o}K$ for 5 minutes.

Measurements made from 5-$20^{o}K$ were accomplished by moving the sample through the temperature gradient of the helium vapor above the bath. The sample was fixed against a Cu plate to ensure temperature stability, and a carbon thermometer was used to measure the temperature. In this range only $.1^{o}K$ accuracy was achieved, and temperature drifts were monitored during a data run rather than stabilizing the temperature.

B.2 Shielding

All devices and probe geometries were sensitive to common rf frequencies (FM, TV, microwave ovens, etc.) and to magnetic fields (earth's, 60 Hz, etc.). Shielding was very important and could only be considered adequate when additional shielding resulted in no change in performance of the device. This was because the proximity effect interfaces observably changed characteristics with only 10^{-17}W of rf absorbed, and were therefore the most sensitive detector available.

Magnetic shielding was provided by several concentric μ-metal cylinders outside of the nitrogen dewar. Static magnetic fields measured in the dewar were reduced to a 100 microgauss level. To eliminate any remaining fields, compensating coils were mounted near the device. Zero fields were indicated by a maximization of the critical current of a bridge at a given temperature. A Pb foil bucket was mounted around the bridge in the helium bath so that any external varying magnetic flux would be shielded by this superconducting shell.

Rf shielding was part plan and part magic. Most experiments were carried out in a Faraday cage with filtered power lines. The cage was advertised as a 100 db room and over the 10-500 MHz range worked well. The various probe wirings were made with a common metal shield completely enclosing the sample, lead wires, and joining the chassis of the voltmeter and current source.[1] This approach did not always uniquely define a ground nor shield all rf interference because there were often subtle ground changes every time a new piece of equipment was hooked up. However, when the critical current was depressed or the voltage rise slightly widened over calculable noise width, a badly defined ground was immediately suspected, although the remedy could remain obscure for many hours. Rf chokes were occasionally placed in the current and voltage lines to the devices as a final check as to the effectiveness of the shielding.

B.3 Measurements

Four basic analog measurements provided most of the data for this thesis: Current-voltage (I-V), differential resistance-current, rf responsivity-current, rf emission-current (Fig. B.1). Temperature and

Fig. B.1

Typical measurements of characteristics of a bridge

(a) Current-voltage (I-V) characteristic produced by totally chopping the bias current and monitoring the voltage change across the bridge with a lock-in amplifier tuned to the chopping frequency. I_c is the critical current; the slope is the resistance of the bridge; ΔI is the excess current, a measure of the average supercurrent flow when a voltage exists across the bridge.

(b) More detail can be seen by looking at the derivative of the I-V curve, also called the differential resistance curve. A graph of dV/dI - I is produced by placing a .1 μA 400 Hz current along with the DC bias current. The tuned lock-in amplifier measures the small changes in voltage due to small current changes, dV/dI.

(c) For small external microwave perturbations a responsivity measurement is the most effective method for exhibiting the induced changes in the characteristics. Incident rf radiation is chopped, and the voltage across a current biased bridge is monitored with a lock-in amplifier tuned to the chopping frequency. Features induced by 10^{-17}W have been observed this way.

(d) RF emission from the internal oscillating voltage of a current biased bridge or series array of bridges has also been measured. High impedance bridge arrays are used directly as loads on a 50 Ω cable, low impedance bridges are placed on a LC resonance circuit to match impedances with external amplifiers.

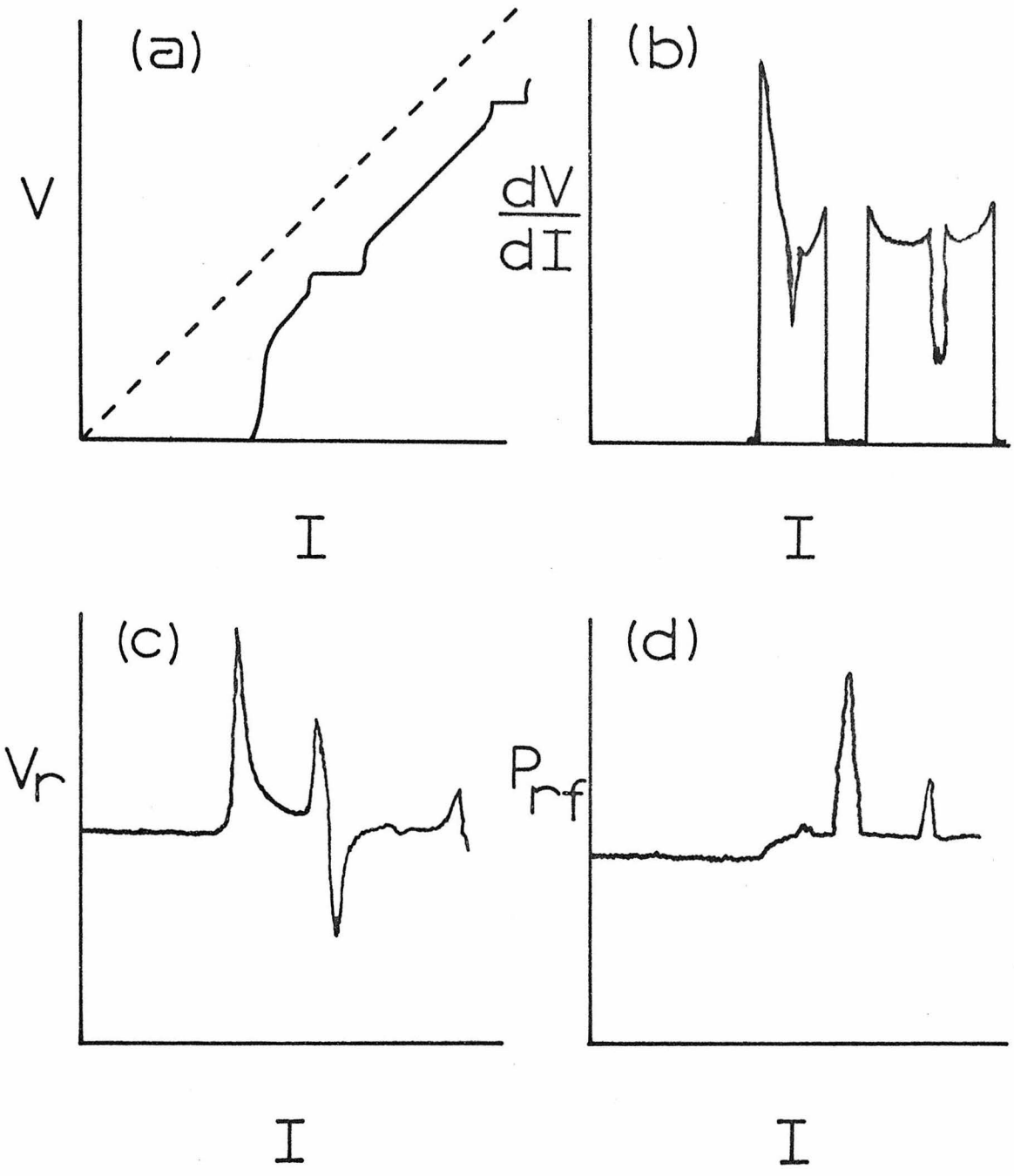
(a)
V
I
(b)
dV/dI
I
(c)
Vr
I
(d)
Prf
I

magnetic field were in general incrementally changed, while current was swept relative to some voltage signal. Four terminal contacts were used in all measurements.

I-V characteristics were obtained by chopping (∿400 Hz) the bias current ramp and monitoring,with a lock-in (PAR HR-8) tuned to the same frequency,the resulting voltage across the device (Fig. B.1a). In general the interesting rf step data were two orders of magnitude below the full voltage sweep, so very little quantitative rf data could be taken off I-V curves.

To enhance the subtle changes in slope of the I-V curve a differential resistance measurement was made (Fig. B.1b). Again a bias current ramp was used, this time with a small (.1 - 1 μA) 400 Hz current component. Once again a tuned lock-in was used to measure the resulting 400 Hz voltage giving the local derivative of the I-V curve, the differential resistance or dV/dI-I.

When low power rf induced changes in the I-V curve were being investigated a responsivity measurement (Fig. B.1c) was found to be more convenient and sensitive than a dV/dI-I sweep. Again a current ramp was applied across the device but now the incident rf power was chopped and the lock-in monitored the change in the I-V curve that resulted from the incident radiation (Fig. B.2). Chopping was available in most rf generator power supplies but for X-band radiation pin diode guide choppers were found to produce much less noise in the responsivity signal. Probably the basic difference was that the pin diode device worked at about 10 volts, whereas the reflex klystron chopper worked at 300 volts. With this technique coherent changes due to 10^{-17}W of rf power absorbed

Fig. B.2

Schematic representation of circuit used to measure rf responsivity and differential resistance. For a responsivity measurement the klystron output is modulated by an 80 db pin diode waveguide chopper. The wave form generator that controls the chopper also is the reference for the lock-in amplifier. A four-terminal measurement is made on the bridge. For differential resistance measurements a small ac signal can be used in parallel with the dc current bias. In this case the rf signal is applied cw. The lock-in used, PAR HR-8, had .5 nV of noise with a setting of .3 sec time constant.

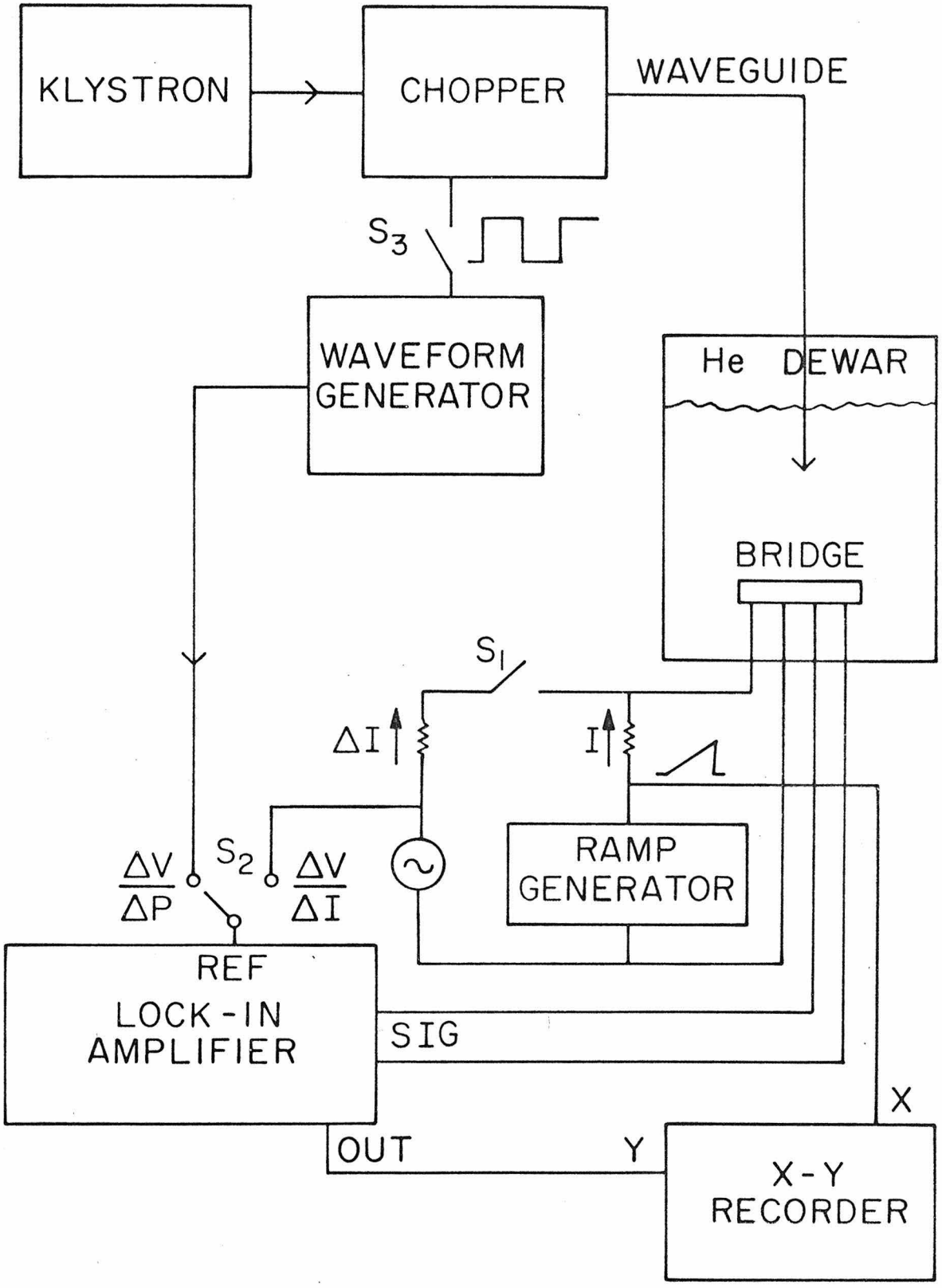
KLYSTRON
CHOPPER
WAVEGUIDE
S3
WAVEFORM GENERATOR
He DEWAR
BRIDGE
S1
ΔI
I
ΔV/ΔP
S2
ΔV/ΔI
RAMP GENERATOR
REF
LOCK-IN AMPLIFIER
SIG
X
OUT
Y
X-Y RECORDER

by a bridge could be detected with a 10 second time constant for the lock-in. The noise level for the lock-in in a 1 second time constant was .5 nV.

B.4 Emission

The most difficult experiments were those involving the detection of rf emissions from the bridges themselves (Fig. B.1d). Typical bridges were 10-100 mΩ and had to be matched to standard 50Ω detection gear. Signals were very small in voltage, at most 10 μV peak to peak in the X-band frequency range. All detection systems had their own resonances in the 10-500 MHz range since the wavelengths were comparable to the cable and probe lengths. This was a tough problem, with each device and each frequency range demanding a different probe and detection design. Three detection systems were particularly noteworthy: An oscillating array detection system for 10-500 MHz, a single bridge detection system for 30 MHz, and a single bridge detection system at 10 GHz.

Since the series array of bridges have resistance of 10-50Ω , it was relatively easy to extract an rf signal. The array was mounted as a load to a 50Ω cable using 1/8" extending wires from the cable end. Current leads had rf chokes mounted within one inch of their contact with the device to avoid losing any of the internally generated power. The 50Ω cable at dewar top fed directly into a 30 db amplifier and was then mixed down in frequency and amplified again by 30 db. A tuned detector converted this signal into a DC voltage.

A single bridge detection system was much harder to design and calibrate because of the impedance mismatch between bridge and

amplifier. At 30 MHz a bridge resistance must be below 10 mΩ to be certain that the 30 MHz oscillation will not be lost in the internal Johnson noise of the bridge. To match power to the outside world an LC resonant circuit (tank) of high Q was used (Fig. B.3). A high impedance preamp was used at the top of the dewar and mixing and amplification followed. This system was susceptible to resonant signals due to multiple reflections along the length of coax, therefore the preamp impedance was adjusted so that the coax formed a reasonable $\lambda/4$ transformer between the tank and the preamp. Again all current leads were highly choked. It is of interest to note that the tank circuit formed across the bridge did not seem to load down the bridge (no modification of the I-V curve).

At X-band a discrete tank was no longer viable, so a waveguide cavity was made with an adjustable length at cryogenic temperatures. The bridge was cut as small as possible so very little superconducting material would remain to affect the field configurations in the cavity. The bridge was mounted to be at an E field antinode ($\lambda/4$ from the end plate) with the bridge current direction in the E direction of the guide. The tuning and Q of the cavity were checked at helium temperature by looking at the reflected wave and the critical current as a function of frequency. The signal was brought out of the dewar by a thin walled stainless steel waveguide and into a Tektronix L30 spectrum analyzer. The analyzer input had to have 80 db of waveguide isolation added to make sure any local oscillator signal from the input mixer did not reach the bridge. Such a measuring system has sensitivity to 10^{-10}W. To increase the detection sensitivity to 10^{-15}W a mixer-preamplifier was

Fig. B.3

Two rf emission detection systems

(a) This coaxial cable system was used for single or double bridge systems of total resistance in the milliohm range. The bridges were mounted in the LC tank at the bottom of the probe. The bridge, signified by the circle with an "X", was current fed by two highly rf choked wires, and the rf voltage across the bridge was monitored across the capacitance C . In some cases the coax was rigid 50Ω cable which led to a room-temperature 50Ω input amplifier. In more sensitive cases the coax was hand fabricated to be of an impedance which was the geometric mean between the LC tank and a high impedance preamp on the dewar top. The coax was then between 10-30Ω , and approximately $\lambda/4$ in length. All amplification was done in 30 db amounts with mixing and frequency changing in between stages to avoid probe length induced rf oscillations.

(b) To look for 10 GHz emission a waveguide equivalent detection system was used. A cavity was formed by a length of waveguide between an iris and a moveable short. The bridge was placed above the short so that it was at an E field maximum of the empty cavity. Any signal coming from the bridges passed through an isolator before reaching the mixer and amplifiers (M and A) since the local oscillator of the mixer would otherwise drive the bridge. The moveable cryogenic short was made by a loose-fitting brass plug with quarter-wave traps D , and a brass loose pitched screw E moving in woods metal nuts.

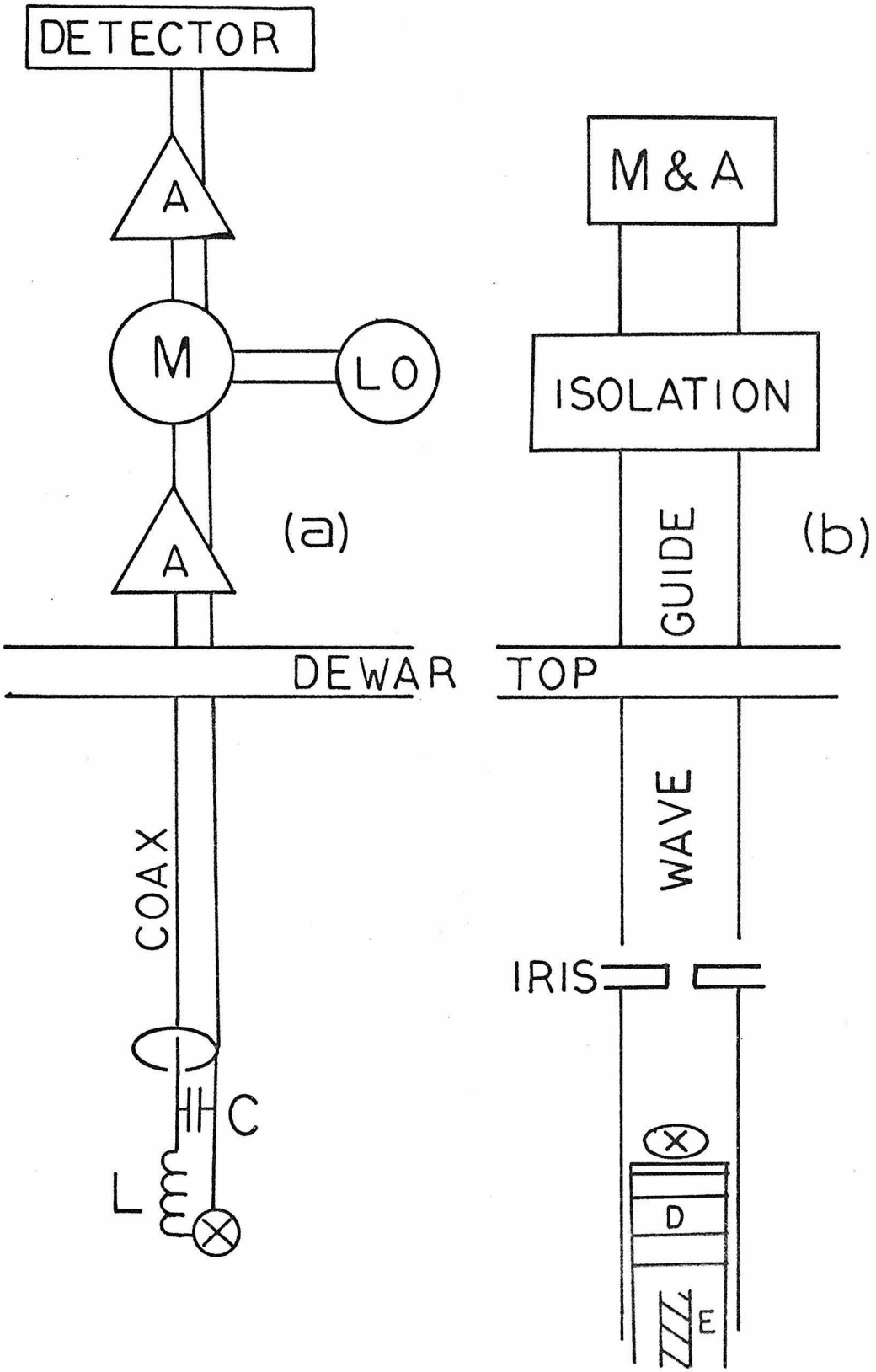
DETECTOR
A
M
LO
A
(a)
DEWAR
COAX
C
L
M & A
ISOLATION
GUIDE
(b)
TOP
WAVE
IRIS
D
E

used. The particular mixer used was a PCR #2619 (made by LEL division of Varian). Since it was not a balanced mixer it was necessary to put 120 db of isolation between the mixer and the device.

B.5 Microcalorimeter

In order to make an absolute calibration of the rf responsivity of the proximity effect bridges, it was necessary to first find the amount of rf energy absorbed for a given rf incident. This fraction was measured using a new microcalorimeter technique developed during this investigation.[2]

At high current levels the resistance of a standard bridge becomes unstable (typically 2-3 mA for a 10μ wide Nb/Ta bridge). Expermentally it has been determined that this happens when the power dissipated in the bridge region is large enough to raise the temperature of the bridge to the transition temperature of the surrounding strong superconducting film. If some rf power was also dissipated in the bridge, less DC power was needed before the resistance instability occurred. Thus by finding the decrease in the DC bias needed to drive the bridge to resistance instability one could estimate the rf power absorbed. Experimentally the rf power absorbed was linear in the incident power over the 40 db range that noticeably changed the I-V characteristics, an indication of the correctness of this method. The power absorption was also linear in bridge resistance as is expected for the effective rf current bias that results from the characteristically high waveguide impedance and low bridge impedance. The absorption fraction proved approximately constant using 10, 35, 96 GHz radiation.

In each case the device was placed $\lambda/4$ below the open end of a fundamental mode rectangular waveguide. The current direction of the bridge was oriented along the E field of the guided wave.

It is important to notice that the calibration of absorption fraction was done at high DC current bias (1-3 mA) and moderate rf power levels, thus such calibration must be used with caution at low bias levels (near I_c) and threshold rf power levels.

APPENDIX C

THERMAL EFFECTS BETWEEN WEAKLY COUPLED WAVE FUNCTIONS

Recent articles about the thermal effects of superconducting weak links[1] have proposed that many of the effects seen in the I-V characteristics of Dayem-Anderson bridges and point contacts are attributable to thermal effects. For the particular case of proximity effect bridges, this investigation has shown Joule heating is also responsible for several effects: one type of critical current hysteresis, setting an upper voltage limit on coherence in standard geometry bridges, and creating a resistance instability ("boiling") on the I-V curve. However, it must be pointed out that self heating can be made arbitrarily small by proper choice of bridge geometry and materials. This section analyzes these thermal effects and indicates the physical parameters involved in their control.

C.1 Substrates

The thermal problem is clearly defined. A DC bias current flowing through the ohmic resistance of the bridge generates I^2R power. This heat flows continually through the sapphire-metal interface, along the superconducting film, or directly into the helium bath. Most of the heat flows into the sapphire beneath the bridge because of the relatively low thermal impedance of this path. Whenever heat flows through a material interface of thickness much less than the phonon mean free paths in either material, it is customary to think about the temperature distribution as a simple temperature drop across the boundary

(thermal boundary resistance model). The phonon mean free path is millimeters in $3^{o}K$ sapphire and $100\mathring{A}$ in Nb/Ta, thus such a model applies to the films used in this investigation. Hence the heat flow into the sapphire can be written

$$\frac{dQ}{dt} = \alpha \text{ (Area of interface)}(\delta T)$$

where the sapphire is considered at bath temperature. The value for the constant α has been measured for Sn on sapphire in past investigations, $\alpha = 2W/cm^2\text{-}{}^{o}K.^2$

At constant bias current a steady state temperature is reached at each point. This may at first seem strange because the dynamic phase slip model for these bridges contains a time varying normal current, hence variable Joule heating. However, the thermal time constant is long compared to the Josephson periods of the interesting high voltage operational ranges. To calculate the thermal time constant for a typical bridge and compare this to the relaxation times expected at higher voltages, consider a typical bridge 1×10 microns, $.1\Omega$, in $100\mathring{A}$ thick Ta film on sapphire. The instantaneous power balance equation is

$$\text{Joule power} = \text{power lost to sapphire + power used to change bridge temperature}$$

$$I^2R = \alpha \text{ (Area of interface) } T + \text{(Ta density)(Volume of bridge)} \times \text{(Specific Heat Ta)}(d(\delta T)/dt)$$

putting in values for the physical constants

$$d(\delta T)/dt) + (3 \times 10^8)\delta T = I^2R/N$$

A simple differential equation like this has an exponential term in the solution with a time constant of 3×10^{-9} seconds. Thus if the frequencies are above 10 GHz (voltages above 20 μV) the bridge region can be considered as having an elevated but steady temperature. One point needs particular emphasis. In the thermal balance equation above, α must be determined. The planar geometry of the proximity effect bridge would make feasible the deposition of a micro-resistance thermometer on top of the bridge area. Thus it would be possible to precisely find the average bridge temperature for a given bias current and deduce α directly. This direct approach is on the resolution limit of fabrication technology, but fortunately it is also possible to arrive at consistent temperature rise numbers from several different indirect lines of reasoning.

C.2 Experimental Measurements of $\alpha(Ta\text{-}Al_2O_3)$

It was possible to experimentally measure α by two methods, both requiring knowledge of some fixed temperature at which a qualitative change appeared on the I-V characteristic. One such temperature was T_H, the bridge temperature above which interference effects did not exist. The other temperature was T_{cs}, the bridge temperature (and strong film transition temperature) above which distinct resistance fluctuations occurred.

First, T_H was experimentally well defined and was the temperature where the differential resistance of the bridge measured at zero bias began to drop from the normal state value (Fig. C.1a). If the bath was below this temperature, quantum interference existed up to the

Fig. C.1

One temperature marker on a typical I-V characteristic is T_H , the highest bridge operating temperature where rf interference can be monitored. Experiments have indicates that for a typical proximity effect bridge this temperature can be found at the beginning of the superconducting transition of the bridge region (a). This graph is of the resistance across the bridge as a function of the bath temperature. Using low power levels of rf radiation so that most heating is due to the bias current, the highest frequency "step" signature on the dV/dI - I curve will occur when the bridge region attains T_H , (b). It is possible to have a high frequency cutoff for nonthermal reasons, but if the bridge has shown interference at higher frequency when operated at lower temperatures, then a low voltage interference cutoff is due to T_H being exceeded.

Another temperature marker on the dV/dI - I curve is the resistance fluctuation which occurs when Joule heating elevates T_{bridge} to T_{cs} , the transition temperature of the strongly superconducting film (b).

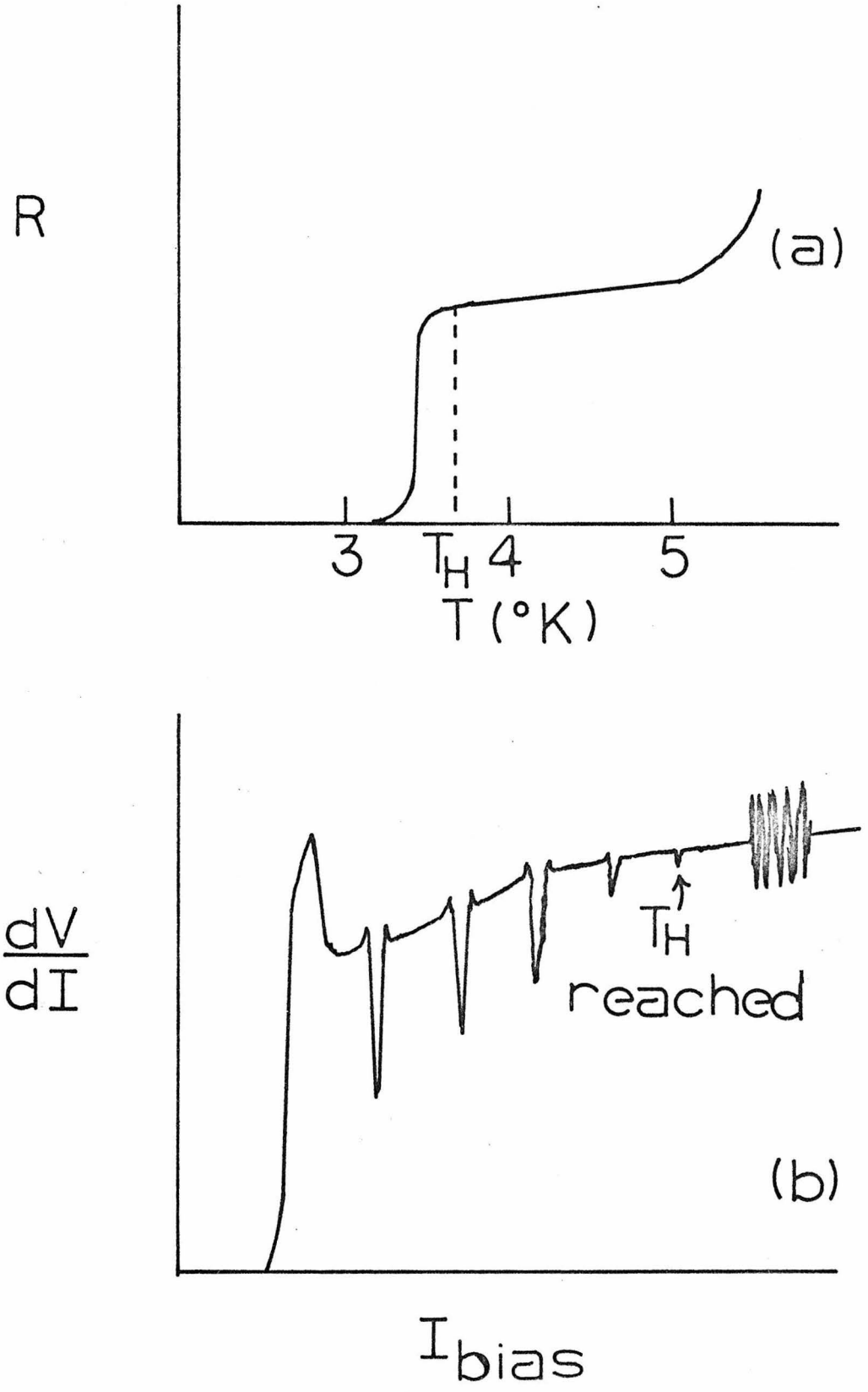
R
(a)
3
T_H
4
5
T (°K)
$\frac{dV}{dI}$
T_H
reached
(b)
I_{bias}

voltage where heating from $(V_{DC}^2)/R$ plus any heating from external rf induced currents was enough to raise the bridge temperature above T_H (Fig. C.1b). Using small rf powers and monitoring the step structure it was possible to see at what bias power, $I_{Bias}^2 R$, the bridge region had reached T_H. By varying the bath temperature the formula $\delta T_{Bridge} = \alpha(I^2R)(Area)$ was confirmed, giving for several bridges $\alpha(Ta\text{-}Al_2O_3) \sim 2W/cm^2\text{-}^oK$. For a standard bridge (.1Ω, 10 x 1μ, 100Å thick) in a voltage sustaining state, a current of 100 μA gave $\sim.01^oK$ temperature rise.

The other marker on the I-V curve, T_{cs}, allows measurement of α for larger $\delta T/T$. Experimentally, rapid resistance fluctuations occurred when the current bias reached 2-3 mA; this corresponded to a bridge temperature about 2^oK above the bath and had previously been associated with the nucleation of helium bubbles.[3] However, for fine wires and thin films the onset of bubble nucleation cooling usually takes place with a temperature difference of only .2-1^oK.[4] There was strong reason to suspect the observed fluctuating resistance in these circuits corresponded to the neighboring strong superconducting film alternately being driven normal and then cooling back down below the transition temperature. This idea was tested by anodizing the strong film immediately around the bridge, thus lowering the local transition temperature of the strong film and shifting the onset of the fluctuating resistance to a correspondingly lower bias current.

As a measure of α at higher $\delta T/T$ the Joule power needed to increase the bridge to T_{cs} as a function of T_{bath} was measured (Fig. C.2a). As the temperature was lowered below the transition

Fig. C.2

The approximate linearity of bridge temperature rise with Joule power is displayed by plots of (a) Joule power needed to reach T_{cs} as a function of T_{bath}, and (b) total power needed to reach T_H as a function of T_{bath}.

These graphs indicate that $\delta T_{bridge} \sim \alpha(P_{Joule})$. The value of α given by these experiments is

$$\alpha(\text{Ta-sapphire}) = 1\text{-}4 \text{ W/cm}^2 - {}^{o}\text{K}$$

However, for $\delta T_{bridge} > 2^{o}\text{K}$, α can approach 10 $\text{W/cm}^2 - {}^{o}\text{K}$.

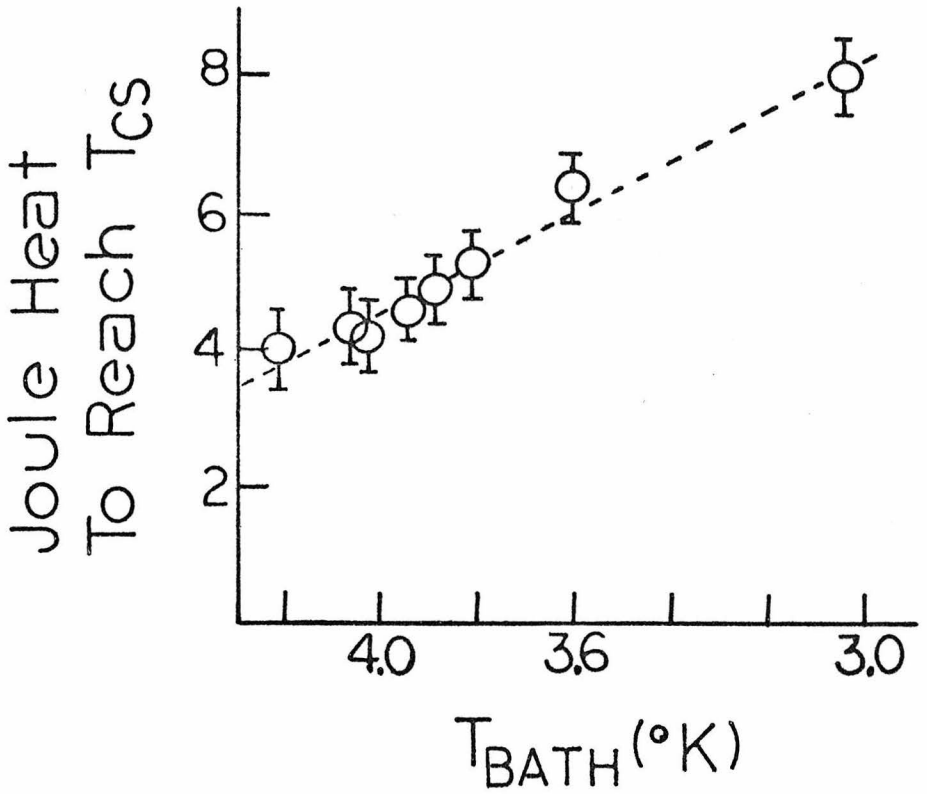
Joule Heat
To Reach T_{CS}
8
6
4
2
4.0
3.6
3.0
T_{BATH} (°K)

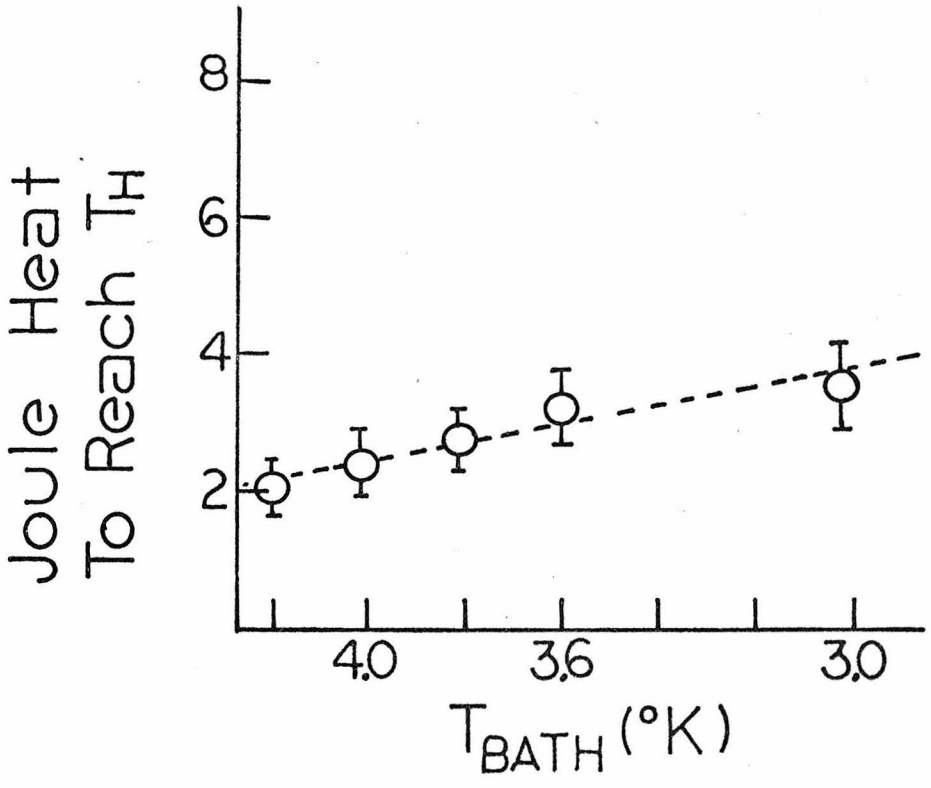
Joule Heat
To Reach T_H
8
6
4
2
4.0
3.6
3.0
T_{BATH} (°K)

temperature of the bridge more bias current was needed to bring the device to the resistance fluctuating state. In fact the power dissipated was linear in $T_{cs}-T_{bath}$, giving a value for $\alpha(Ta-Al_2O_3) \sim 2\text{-}4 W/cm^2-{}^oK$. In the case of the standard .1Ω Nb(100Å)/Ta(200Å) the fluctuation set in at 5.4^oK, the measured transition temperature T_{cs}, therefore allowing voltage operation up to .2-.3 mV (100-150 GHz).

Thus the fluctuation of resistance was due to the strong film transition temperature, T_{sc}, being attained by Joule heating in the bridge region, and not due to the onset of a special boiling mode of helium cooling. One mechanism that could account for this fluctuation would be a cyclic thermal process: the bridge volume heats up to T_{sc}, the neighboring strong film becomes normal and thus improves its thermal conduction coefficient by a factor of 10, heat is now dissipated to the sapphire and helium bath over a larger area, this increased cooling of the bridge region drops the temperature below T_{sc} and the strong film becomes superconducting again.

C.3 Calculation of $\alpha(Ta-Al_2O_3)$

A second approach to find the temperature increase of a bridge per unit power dissipated is to solve the thermal boundary value problem. The majority of the heat flows into the sapphire. The thermal coupling between the refractory metals and the sapphire is very good owing to the density and sound velocities of Ta, Nb, and sapphire.[5] The thermal boundary resistance can be calculated from phonon transmission matching or experimentally from bias current levels necessary to raise the bridge

temperature to T_H or T_{cs}). Using standard acoustic transmission impedance calculations and the Debye spectrum of phonons, the amount of heat flowing across an interface between two solids has been calculated by Little.[6] This approach results in the formula

$$\frac{dQ}{dt} = (2 \times 10^{10})(\Gamma) \frac{T^3}{c_1^2} (A)(\delta T) \text{ Watts}$$

which is accurate for small values of $\delta T/T$. In this formula c_1 is the velocity of sound in the bridge region, A is the area of interface, T is the bath temperature, δT is the temperature difference between the bridge and the bath, and Γ is an impedance match factor with functional dependence on the density and sound velocity ratios of the two solids. For a standard .1Ω, 1 x 20 micron bridge of Ta operating between 3 and 4^oK, the calculated heat flux implies $\alpha(Ta\text{-}Al_2O_3) \sim 1 W/cm^2\text{-}^oK$. Thus the temperature rise for a bias current of 100 μA ($10^{-9}W$) is $\sim .01^oK$ and 1 mA gives about 1^oK. However, at large temperature differences, $\delta t/T \geq .1$, it is more accurate to use the factor $T_1^4 - T_2^4$ instead of $(T_2^3)\delta T$ in the above calculation. The small temperature difference approximation which is most useful for the operating conditions of the bridge tends to underestimate the heat flow at larger δT.

Compared to the sapphire interface, the helium interface supplies very little direct cooling above the λ point (2.17^oK). With the bath at 3^oK and the bridge region $.1^oK$ above the bath temperature $\alpha(Ta\text{-}He) = .01 W/cm^2\text{-}^oK$.[7] However, below the λ point the helium bath becomes

just as effective as the sapphire at heat transfer. The refractory metal film itself conducts little of the heat away, owing to its low thermal conductivity. Estimating from the Wiederman-Franz law, $k/\sigma T = 2.45 \times 10^{-8}$ Watt-ohm/$^{o}K^{2}$, implies $k = 2.5$ W/m-^{o}K . Bulk Ta in the dirty limit typically has values of 2-10 W/m-^{o}K at $3^{o}K$.[8] Again, consider a typical bridge. The cross sectional area of heat flow along the film is 100Å by 20 μm.

Thus

$$\frac{dQ}{dt} = k(A)\frac{\delta T}{\delta z}$$

The largest possible temperature gradient exists if the temperature increase is confined to the bridge region. This approximation yields a heat flow of 2×10^{-7} W/^{o}K. Such a heat flow is small compared to the loss through the sapphire interface.

C.4 Characteristic Healing Length in Ta Films

By calculating a thermal healing length, an estimate on the localization of bridge heating effects can be made. Starting with a line source of heat in a Ta film, a hot film strip of half length r will develop. The order of magnitude for r can be given by comparing the power that will leave a hot strip of length r through the sapphire to the power leaving through the film (Fig. C.3). In effect this length can be considered a measure of the thermal conductivity of the Ta film compared to the thermal coupling to the sapphire.

The power through the interface = $\alpha(rW)\overline{\delta T}$.

The power through the film = $K_N(tW)\frac{\overline{\delta T}}{r}$.

Fig. C.3

A characteristic temperature decay length can be estimated for the refractory films which were used in this investigation. Using a line source of heat in the film (a), and comparing the heat loss through the substrate to that flowing along the film (b), a "half-width" of resulting film temperature distribution can be derived. For the bridge region of these films (c), treated as a normal metal (i.e., using the normal heat conducting coefficient for Ta, k_n), this length is around .5μ or about the typical bridge length. In the strong superconducting adjoining film where $k_s << k_n$ the decay length is much shorter. Hence, the temperature distribution may be thought of as pictured in (d).

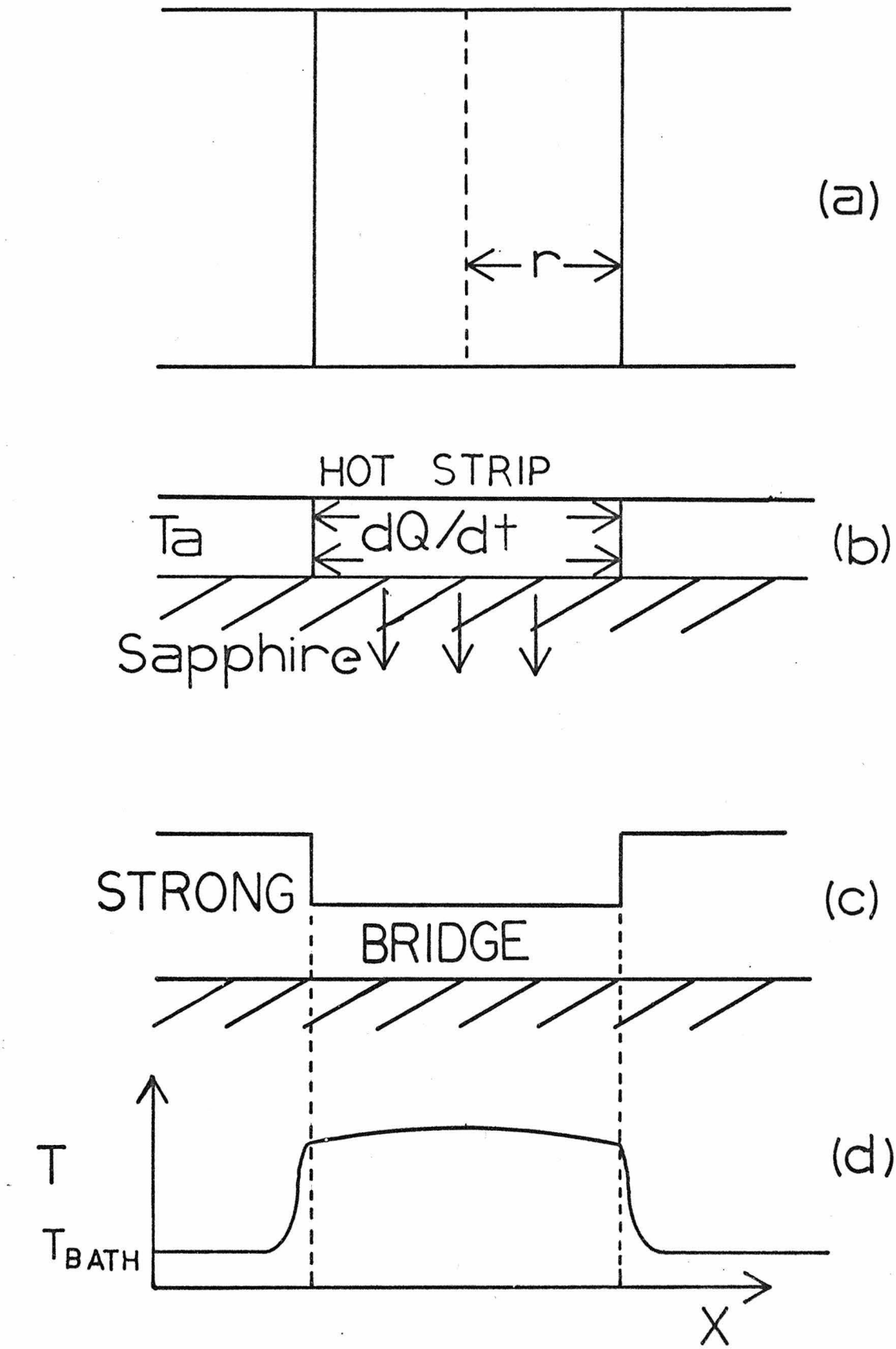
(a)
r
HOT STRIP
Ta
dQ/dt
(b)
Sapphire
STRONG
BRIDGE
(c)
T
T_{BATH}
(d)
X

k_N is the normal metal thermal conductivity coefficient.

Setting these quantities equal gives $r = \sqrt{tk_N/\alpha}$. Using a Ta normal film having thickness 50-100Å, the spot size is $r = .5\text{-}.7\mu$. Thus for all proximity effect bridges the characteristic length is about the bridge length. This leads to an interesting temperature profile--fairly constant temperature within the bridge with a sudden drop to the bath temperature at the boundaries with the strong superconducting film (Fig. C.3d). This quick cutoff results from the several degree higher transition temperature of the strong region. Thus the strong film remains superconducting for small temperature rises of the bridge, and the superconducting thermal conductivity coefficient must be used to calculate the healing length. This coefficient is considerably smaller than the normal case, $k_s << k_N$.

C.5 Microcalorimetry

The onset of the resistance fluctuations was used as a microcalorimeter to measure the amount of microwave radiation absorbed by the bridge.[9] Consider the bias current necessary to bring about this instability; this defines the power dissipation necessary in the bridge before the temperature increases sufficiently to cause a super to normal transition in the neighboring strong film. For example, if $I_{bias} = 2$ mA is necessary to reach a fluctuating resistance across a .1 bridge, then 4×10^{-7}W is the required power. By inducing rf current in the bridge by incident microwaves, less DC bias is necessary to reach the required dissipation power. A linear increase in rf power incident on the bridge over a 40 db range leads to a linear decrease in

DC power necessary to reach the instability. Thus for any particular bridge mounting and film geometry the fraction of incident radiation absorbed by the device can be accurately measured.

This microcalorimetric technique has been experimentally examined over a 40 db range of rf power and has been used in these experiments as a way in which to determine an absolute calibration of these devices. The relative responsivity measurements at different frequencies could not be done without knowing the fraction of incident radiation that was absorbed.

C.6 Thermal Limit on High Frequency Response

To date most proximity effect links have exhibited self heating effects on the high frequency quantum interference which has limited the frequency response to below one supposed frequency limit of $2\Delta/h \sim 1000$ GHz. The main impediment for higher frequencies has been the slow increase in bridge resistance and temperature and the corresponding slow decrease in rf step size with increasing voltage. Higher frequency response can be achieved by lowering the bath temperature to several degrees below the T_{cw}, but even then quantum interference effects are thermally quenched before $2\Delta/h$ is reached using standard bridge geometry and materials.

Some bridges reach higher frequency response than others even though they are made of the same materials. In almost all cases the bridges that both increase in temperature least for a given voltage and that have the highest value of $T_{cs} - T_{cn}$ have had the highest frequency response. The highest frequency response achieved with standard bridge

geometry and Nb/Ta films is 300 GHz (3×10^{-12}sec). This frequency corresponds to .62 mV or about $\Delta_s(T_{bridge})/e$. At this frequency the bias current produced 3.6×10^{-6}W of bridge dissipation and the I-V characteristic also showed resistance fluctuation onset. As a final check of the resistance fluctuation model, a 1μ bridge was tested in a Nb_3Sn film ($T_{cs} = 17.5^oK$). The bridge operated at $T_{cb} = 1.5^oK$, and the bridge could sustain more than 10 mV (5000 GHz) without resistance fluctuations and with only a 10% increase in resistance. However, internal oscillations of the bridge were not monitored up to this voltage since the T_{cb} was exceeded at a much lower power level.

C.7 Thermal and Magnetic Hysteresis

As the bath temperature decreased, the critical current of a bridge typically became double valued--the critical current for increasing current, $I_{c\text{-up}}$, being larger than for decreasing current, $I_{c\text{-down}}$, (Fig. C .4a). The current difference $I_{c\text{-up}} - I_{c\text{-down}}$ increased with decreasing temperature. While lowering the temperature toward the onset temperature of the hysteresis, the current width of the initial rise of the I-V characteristic became smaller until reaching zero at the beginning of hysteresis. The width of the initial rise, ΔI_o , was defined as the difference between the bias current where the bridge had a maximum resistance and the critical current. For low critical currents ΔI_o has been related to internal bridge noise calculated under the assumption of constant temperature,[10] $\Delta I_o = \sqrt{k_B T I_c/\Phi_o}$. However, for large I_c when $I_c V$ Joule heating considerably changed the bridge

Fig. C.4

At large critical currents hysteresis develops in the I-V characteristic. (a) The critical current with increasing bias current, $I_{c\text{-}up}$, becomes larger than the critical current with decreasing bias, $I_{c\text{-}down}$. The onset of this hysteresis occurs when the initial voltage rise at I_c becomes metastable due to thermal effects. This happens when the predicted noise width of the voltage rise at I_c is less than the critical current shift caused by the temperature change in going from the zero voltage to the voltage state, $\Delta I_N < \frac{dI_c}{dT} (\delta T_{Joule})$. To show the thermal nature of t this hysteresis, $I_{c\text{-}down}$ is plotted versus the calculated value of $I_c(T_{bath} + T_{Joule})$ in (b). At higher critical currents (> 500 μA for a typical bridge) $I_{c\text{-}down}$ also becomes a metastable transition.

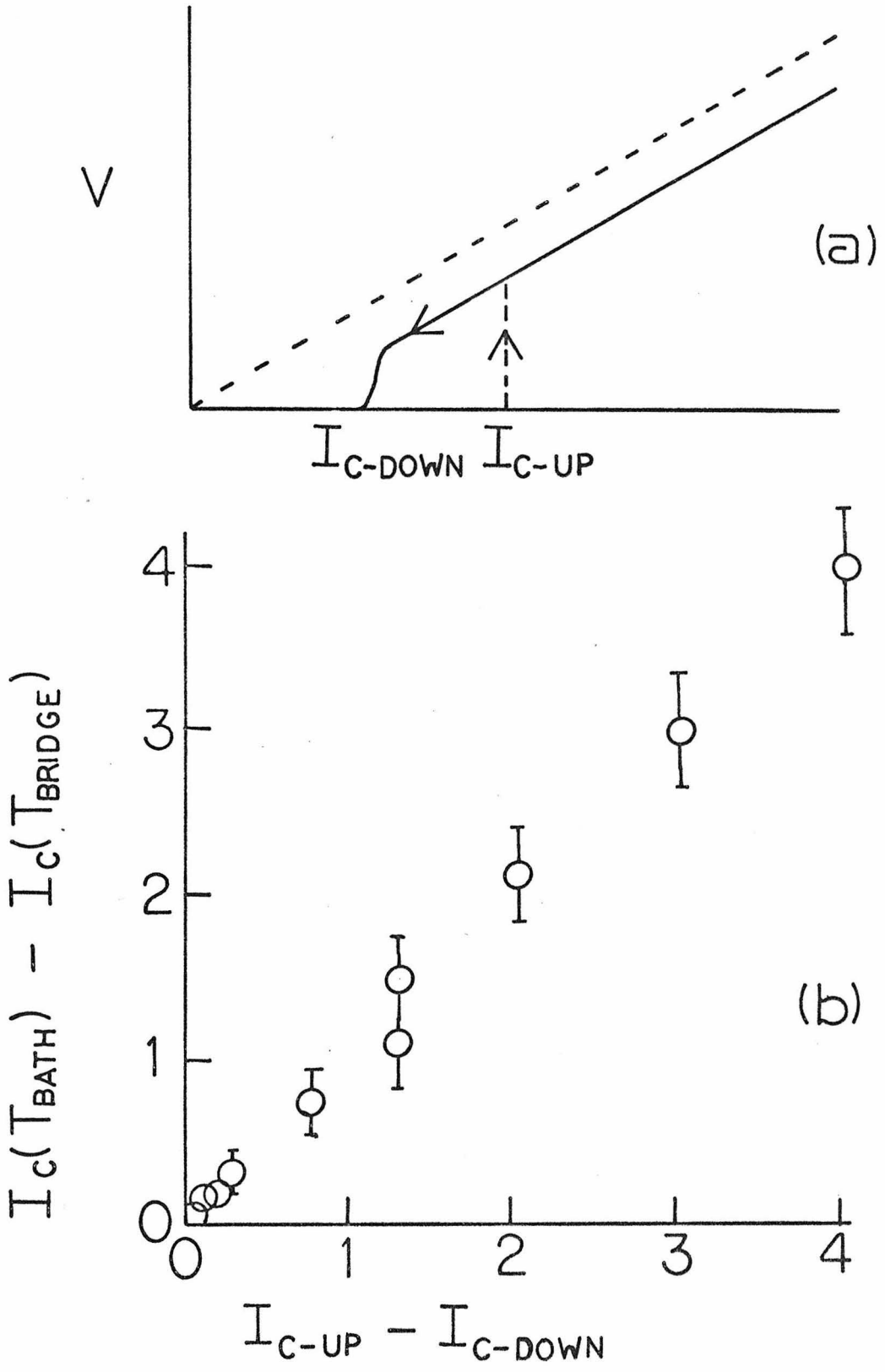
V
(a)
$I_{C\text{-}DOWN}$ $I_{C\text{-}UP}$
$I_c(T_{BATH}) - I_c(T_{BRIDGE})$
0
1
2
3
4
(b)
$I_{C\text{-}UP} - I_{C\text{-}DOWN}$

temperature, the corresponding change in effective bridge critical current could greatly exceed ΔI_o. Hence I_c was double valued; the bridge was either at bath temperature with no voltage, or an elevated temperature at a voltage $V \sim I_c R(1/2)$.

Experimentally, the hysteresis onset agreed well with

$$\Delta I_o = \sqrt{k_B T \, I_c/\Phi_o} \leq \frac{dI_c}{dT} (\delta T)_{Joule}$$

The value $I_{c\text{-down}}(T)$ corresponded closely to the equilibrium critical current $I(T_{bath} + \delta T_{Joule})$, where δT_{Joule} was determined by the Joule heat $R(I_{c\text{-down}})^2$ (see Fig. C.4b). Actually, the critical current in the hysteretic temperature range was not well defined but rather there existed a current range for both $I_{c\text{-up}}$ and $I_{c\text{-down}}$.

It was also possible to choose a bridge geometry that was conducive to trapping magnetic flux after a certain threshold bias current had been reached. One such geometry was a bridge containing a small hole which was off center relative to the bridge width. Magnetic flux quanta trapped in this hole acted to shift the I-V curve in a discrete and predictable way. Upon reducing the bias current after a unit of flux was trapped, it was often necessary to reverse the direction of the bias current in order to untrap the flux and return the I-V characteristic to its original state. This type of magnetic switching appears to be very rapid and may have some use as a possible computer element. Magnetic and thermal hysteresis both existed in proximity effect bridges but were very easy to differentiate experimentally.

REFERENCES

Introduction

1. B. D. Josephson, Physics Letters 1, 251 (1962).
2. P. W. Anderson, Lectures on the Many-Body Problem (Academic Press, Inc., New York, 1964), Vol. 2, p. 113.
3. R. C. Jaklevic, J. Lambe, A. H. Silver, and J. E. Mercereau, Phys. Rev. Letters 12, 159 (1964).
4. T. J. Rieger, D. J. Scalapino, and J. E. Mercereau, Phys. Rev. Letters 27, 1734 (1972).
5. M. L. Yu, Ph.D. Thesis, California Institute of Technology, 1974.

Chapter I

1. W. Kahn and D. Sherrington, Rev. Mod. Phys. 42, 1 (1970).
2. R. P. Feynman, Lectures on Physics, Vol. 3 (Addison-Wesley Publishing Co., New York, 1965), pp. 21-25.
3. L. P. Gor'kov, Soviet Phys. JETP 7, 505 (1958).
4. W. Meissner and R. Ochsenfeld, Naturwiss.21, 787 (1933).
5. F. London, Superfluids, Vol. I (Dover Publications, Inc., New York, 1961), pp. 142-155.
6. K. L. Chopra, Thin Film Phenomena (McGraw-Hill Book Company, New New York, 1969), pp. 530-534.
7. R. D. Parks, Superconductivity, Vol. I (Marcel Dekker, Inc., New York, 1969), pp. 51-117.
8. J. R. Tucker and B. I. Halperin, Phys. Rev. B 3, 3768 (1971).
9. B. S. Deaver and W. M. Fairbank, Phys. Rev. Letters 7, 43 (1961).
10. P. W. Anderson, Rev. Mod. Phys. 38, 298 (1966).
11. B. D. Josephson, Physics Letters 1, 251 (1962).
12. R. P. Feynman, loc. cit., 21- 9.

13. P. W. Anderson and J. M. Rowell, Phys. Rev. Letters 10, 230 (1963); S. Shapiro, Phys. Rev. Letters 11, 80 (1963).

14. τ_{TH} is discussed in M. Tinkham, Phys. Rev. B 6, 1747 (1972, τ_Q in J. Clarke, Phys. Rev. Letters 28, 1363 (1972), and τ_R in J. L. Levine and S. Y. Hsieh, Phys. Rev. Letters 20, 994 (1968).

15. V. L. Ginsburg and L. D. Landau, J. Exptl. Theoret. Phys. (USSR) 20, 1064 (1950).

16. P. G. DeGennes, Rev. Mod. Phys. 36, 225 (1964).

17. D. L. Livesey, Atomic and Nuclear Physics (Blaisdell Publishing Co., Waltham, Mass., 1966), p. 26.

18. M. L. Yu, Ph.D. Thesis, California Institute of Technology, 1974.

Chapter II

1. H. A. Notarys and J. E. Mercereau, J. Appl. Phys. 44, 1821 (1973).

2. R. D. Parks (ed.), Superconductivity, Vol. 2 (New York: Marcel Dekker, Inc., 1969), p. 1005.

3. D. W. Palmer, H. A. Notarys, and J. E. Mercereau, Appl. Phys. Letters 25, 527 (1974).

4. E. P. Harris, "Preparation of Superconducting Weak Links in Molybdenum Films by Ion Implantation," (To be published in IEEE Magnetics Trans., March 1975).

5. R. Adde, P. Crozat, S. Gourrier, and G. Vernet, Rev. de Physique Appliquée 8, 455 (1973); R. Adde, et al., Rev. de Physique Appliquée 9, 179 (1974).

6. R. Rifkin, D. A. Vincent, and B. S. Deaver, "Detailed Measurements of the Response of an rf SQUID in the Regime $Li_c < \phi_0/2\pi$," (To be published in IEEE Magnetics Trans., March 1975).

7. R. K. Kirschman, H. A. Notarys, and J. E. Mercereau, Phys. Letters 34A, 209 (1971).

8. T. J. Rieger, D. J. Scalapino, and J. E. Mercereau, Phys. Rev. Letters 27, 1787 (1971).

9. T. J. Rieger, D. J. Scalapino, and J. E. Mercereau, Phys. Rev. B 6, 1734 (1972).

10. S. Shapiro, Phys. Rev. Letters 11, 80 (1963).

11. J. Bardeen, Rev. Mod. Phys. 34, 667 (1962).

12. P. G. DeGennes, Rev. Mod. Phys. 36, 225 (1964).

13. J. Clarke, J. de Physique 29, C2-3 (1968).

14. T. A. Fulton, L. N. Dunkleberger, J. Appl. Phys. 45, 2283 (1974); W. J. Skocpol, M. R. Beasley, and M. Tinkham, Bull. Am. Phys. Soc. 18, 302 (1973); W. J. Skocpol, M. R. Beasley, and M. Tinkham, J. Appl. Phys. 45, 4054 (1974).

15. S. K. Decker, private communication.

16. P. W. Anderson, in preprint of his article in Lectures on the Many-Body Problem, E. R. Caianello (ed.) (Academic Press Inc., New York, 1964), Vol. 2, p. 113.

17. R. K. Kirschman, Ph.D. Thesis, California Institute of Technology, 1971.

18. M. G. Hauser and D. W. Palmer, Rev. de Physique Appliquée 9, 53 (1974).

19. P. L. Richards, F. Auracher, T. Van Duzer, Proc. IEEE 61, 36 (1973); S. P. Russer, J. Appl. Phys. 43, 2008 (1972).

20. M. L. Yu, Ph.D. Thesis, California Institute of Technology, 1974.

21. W. A. Little, Symposium on the Physics of Superconducting Devices, April 1967, S-2.

Chapter III

1. D. R. Tilley, Phys. Lett. A 33, 205 (1970);
T. D. Clark, Phys. Rev. B 8, 137 (1973);
W. T. Tsang and S. Wang, Appl. Phys. Letters 24, 519 (1974);
M. L. Yu and A. M. Saxena, "Coherent a.c. Josephson Effect in a Bulk Granular Superconducting System", (To be published in IEEE Magnetics Trans., March 1975).

2. J. Bardeen and J. L. Johnson, Phys. Rev. B 5, 72 (1972).

3. R. K. Kirschman, Ph.D. Thesis, California Institute of Technology, 1971.

4. B. F. Field, T. F. Finnegan, and J. Toots, Metrologia 9, 155 (1973).

5. M. L. Yu, Ph.D. Thesis, California Institute of Technology, 1974.

Chapter IV

1. T. J. Rieger, D. J. Scalapino, and J. E. Mercereau, Phys. Rev. B 6, 1734 (1972).

2. I. Jaguchi and H. Yoshioka, J. Phys. Soc. Japan 27, 1074 (1969);
W. S. Goree, and F. Chilton, Proceedings of the Conference on Fluctuations in Superconductors (Stanford Low Temperature Physics Department, 1968), p. 167.

3. M. L. Yu, Ph.D. Thesis, California Institute of Technology, 1974.

4. The same relationship regarding the spatial variation of pair density that exists between Dayem-Anderson film bridges and the proximity effect bridges also exists between constriction S/N interfaces and constant width S/W/N interfaces. In one case the locally increased current density created a depression of the pair density, in the other case a material manipulation resulted in an equilibrium gradient in pair density. The necessity to control and measure dimensions precisely along only one axis instead of two greatly facilitates the fabrication and systematic variation of these constant width interfaces.

Appendix A

1. D. W. Palmer and S. K. Decker, Rev. Sci. Instrum. 44, 1621 (1973).

2. D. W. Palmer and J. E. Mercereau, Appl. Phys. Lett. 25, 467 (1974).

3. S. Somekh, E. Garmire, A. Yariv, H. L. Garvin, and R. G. Hunsperger, Appl. Phys. Lett. 22, 46 (1973).

Appendix B

1. R. Morrison, Grounding and Shielding Techniques in Instrumentation (John Wiley, 1967).

2. M. G. Hauser and D. W. Palmer, Rev. Phys. Appl. 9, 53 (1974).

Appendix C

1. T. A. Fulton, L. N. Dunkleberger, J. Appl. Phys. 45, 2283 (1974); W. J. Skocpol, M. R. Beasley, and M. Tinkham, J. Appl. Phys. 45, 4054 (1974).

2. D. A. Neeper and J. R. Dillinger, Phys. Rev. 135, A1028 (1964).

3. Private suspicion voiced by M. L. Yu, H. A. Notarys, and S. K. Decker (1973).

4. J. R. Dillinger (ed.), Low Temperature Physics and Chemistry (University of Wisconsin Press, 1958), p. 41.

5. G. V. Samsonov, Handbook of the Physicochemical Properties of the Elements (IFI/Plenum Data Corp., New York, 1968), pp. 128,398; Properties of Clear Linde Sapphire, private publication of Union Carbide.

6. W. A. Little, Can. J. Phys. 37, 334 (1959).

7. J. I. Gittleman and S. Bozowski, Phys. Rev. 128, 646 (1962); also reference 1(b) above.

8. Y. S. Jouloukian, Thermophysical Properties of Matter, Vol. I, (IFI/Plenum, New York, 1970), p. 355.

9. M. G. Hauser and D. W. Palmer, Rev. Phys. Appl. 9, 53 (1974).

10. R. K. Kirschman, Ph.D. Thesis, California Institute of Technology, 1971.